Research Report 225
LASER SCINTILLATION CAUSED BY TURBULENCE NEAR THE GROUND

by
Donald J. Portman,
Edward Ryznar and Arif A. Waqif

JANUARY 1968

U.S. ARMY MATERIEL COMMAND
COLD REGIONS RESEARCH & ENGINEERING LABORATORY
HANOVER, NEW HAMPSHIRE

University of Michigan
Grant No. DA-AMC-27-021 63 G7
DA Task 1VO14501B52A02

PREFACE

The research described in this report was conducted by the University of Michigan Department of Meteorology and Oceanography for the U.S. Army Cold Regions Research and Engineering Laboratory, Research Division (Mr. James A. Bender, Chief) under Grant No. DA-AMC-27-021-63 G7. It was under the general supervision of Dr. R.W. Gerdel, then Chief, Environmental Research Branch, and followed earlier work for CRREL at the University of Michigan having to do with optical scintillation and visual resolution over snow, ice, and frozen ground. The work was done between 1 November 1963 and 30 May 1966.

The results of the earlier work showed that practical application of optical propagation through cold region atmospheres could be seriously hampered by diffractive effects. With the development of continuous wave lasers suitable for field use it became necessary to examine more closely the atmospheric limitations to optical propagation. The work reported here contributes basic information on the diffractive phenomenon known as scintillation. Although the field experiments were not conducted in cold regions, the results are directly applicable to cold region environments where scintillation must be considered as an important factor in the design of laser systems.

Part of the research described here was that of W. Gale Biggs. His work is more completely described in "Measurement and analysis of turbulence near the ground with a hot wire anemometer system," a dissertation submitted in partial fulfillment of the requirements for the degree of Doctor of Philosophy at the University of Michigan.

The authors are indebted to Mr. Floyd C. Elder and Mr. Francis Yockey for their assistance in the measurement phases of the investigation and to Mr. Fred Brock for the numerical solutions of equations 2.31 and 2.32.

Citation of commercial products is for information only and does not constitute official approval or endorsement.

USA CRREL is an Army Materiel Command laboratory.

CONTENTS

ILLUSTRATIONS

CONTENTS (Cont'd)

TABLES

SUMMARY

Laser scintillation was measured for a horizontal optical path 500 m long and 1 m high for various conditions of horizontally homogeneous turbulence. Wind direction, average vertical distributions of wind speed and temperature, and, in some cases, turbulent fluctuations of wind velocity were measured simultaneously. The results of the measurements were analyzed in relation to a set of theoretical relationships derived by Tatarski (1961) for electromagnetic wave propagation in turbulent flow.

Tatarski's derivation of the scintillation frequency spectrum (at a point in a plane perpendicular to the optical path) in relation to the three-dimensional spectral density of index of refraction inhomogeneities is summarized and interpreted in relation to its validity for various conditions of turbulence.

Analysis of the spectral data showed that their characteristics were similar to Tatarski's theoretical spectrum if the divergence of the laser beam, the size of the receiver aperture, the intensity of scintillation and turbulence spectra were considered. Specific results of the analysis revealed: (1) Agreement between a theoretical variance for scintillation calculated from meteorological data and the variance measured from the spectral densities; (2) A linear increase of the frequency of maximum power with wind speed component normal to the optical path in agreement with Tatarski's model; (3) A decrease of scintillation intensity with path height and an accompanying increase in its frequency of maximum power, both closely related to height variations of stability and wind speed; (4) A relative decrease in intensity of scintillation at low frequencies when the potential temperature increases with height.

The Appendix consists of a description and discussion of the method of spectral analysis and its application to processing the scintillation and turbulence data.

LASER SCINTILLATION CAUSED BY TURBULENCE NEAR THE GROUND

by

Donald J. Portman, Edward Ryznar and Arif A. Waqif

1. INTRODUCTION

Recent plans for the use of laser radiation to transmit information and energy over long paths have emphasized the significance of atmospheric influences. Some of the features of laser radiation particularly useful for this purpose may be seriously influenced by commonplace atmospheric characteristics. In addition to the obvious effect of attenuation by precipitation, clouds and dust, there are the more subtle clear air refractive and diffractive effects. They are generally related to average vertical refractive index gradients which are closely associated with thermal stratification. The latter is a common characteristic of the atmosphere near the ground.

Refraction of horizontally directed laser radiation in the lower atmosphere appears as vertical displacement and distortion of the beam. Time variations in the effect are usually observed to be on the order of minutes or fractions of a minute as the average vertical temperature gradient along the length of the beam varies in strength due to the influence of wind or clouds. Diffractive effects, on the other hand, are related to small scale temperature inhomogeneities created by the mixing action of turbulence in a thermally stratified air layer. The consequent temperature fluctuations are usually on the order of seconds or fractions of a second.

Scintillation is the diffractive effect that appears as rapid fluctuations in brightness* of a small and distant object. The effect may also be seen, in the absence of other light, as a mottled shadow pattern on a screen perpendicular to an optical beam. Figure 1 is a photograph, taken in 1/1000 of a second, of a shadow pattern produced by a continuous wave laser beam after propagation through a 500-m path, 1 m above the ground. There was steady turbulence and the average vertical temperature gradient was about 0.4 C/m at the height of the beam. Such a shadow pattern is never observed to be motionless. If the beam consists of parallel rays, the shadow pattern moves across the screen with the speed of the wind component normal to the optical path. It is apparent that a photometer, having a small aperture in the plane of the screen, will sense a fluctuating brightness as the shadow pattern moves. Such an arrangement is an easy and commonly used method to study the characteristics of scintillation.

An example of scintillation familiar to all is the twinkling of stars, often a major problem for astronomers. Because little is known concerning small scale motions in the higher atmosphere, however, there has been a general lack of understanding of stellar scintillation and its relation to turbulence characteristics. There have been, nonetheless, many theoretical analyses for both optical and radio wavelengths. A comprehensive survey of the literature on optical scintillation is given by Meyer-Arendt and Emmanuel (1965).

Theoretical models appropriate for horizontal optical paths in the surface layer of the atmosphere have been developed by Obukhov (1953), Chernov (1960), Tatarski (1961) and Hufnagel and Stanley (1964). Experimental results suitable for comparison to theoretical models that lead to

*The word "scintillation" used here refers exclusively to brightness or intensity scintillation.

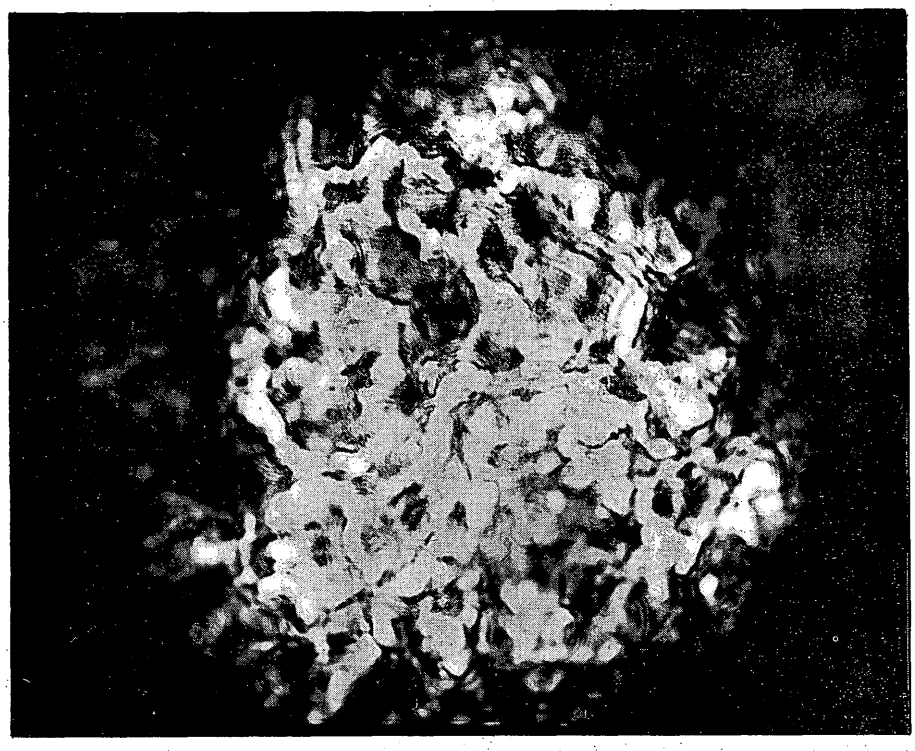

Figure 1. Shadow pattern photograph of laser scintillation obtained by directing the laser beam to a 15-in. parabolic mirror and placing a camera near the focal point. The circular diffraction patterns are apparently caused by imperfections on the mirror surface and the diagonal pattern in the ~~lower left~~ upper right hand corner by an instrument support guy wire that happened to be in the optical path.

generalization in terms of turbulence parameters have been reported by Gurvich, Tatarski and Tsvang (1958); Tatarski et al. (1958); and Portman, Elder, Ryznar and Noble (1962). Many other observations of scintillation have been reported but few have been made in a way that permits careful analysis of the obvious question of the influence of different wind and temperature conditions on the nature of scintillation. Such analyses are required for the understanding necessary to meaningful prediction of the occurrence and characteristics of laser scintillation.

The work reported here was designed to provide basic information on laser scintillation and its relationship to the characteristics of turbulence. Experiments were conducted with a helium-neon, continuous wave laser whose beam was directed along a 500-m path, 1 m above uniform and level ground, to a photometer. Electrical signals from the photometer were analyzed to determine spectral characteristics of scintillation. At the same time measurements were made of thermal stratification, wind direction, variation of wind with height and, in some cases, the three-dimensional structure of turbulence. The experimental results are compared with those predicted by the theory of Tatarski (1961) to help establish the extent to which the theory may be applied to real atmospheric situations. The results contribute, therefore, to the general problem of predicting clear air diffractive effects on laser propagation in the atmosphere.

LIST OF SYMBOLS FOR SECTIONS 2-5

Symbol	Definition
a	proportionality factor for structure function dependence on separation distance.
c_p	specific heat of air at constant pressure.
da	spectral amplitude of electromagnetic wave amplitude fluctuations.
$d\sigma$	spectral amplitude of electromagnetic wave phase fluctuations.
f	frequency.
f_m	measured frequency of maximum power.
f_0	$V_n(2\pi\lambda L)^{-\frac{1}{2}}$.
g	acceleration due to gravity.
k	wave number for electromagnetic radiation.
k_v	von Karman number.
ℓ_0	microscale of turbulence.
n	index of refraction.
p	atmospheric pressure.
q	specific humidity: mass of water vapor per unit mass of moist air.
r	position vector magnitude.
$\vec{r}_{1,2}$	position vector components.
u	in eq 2.2, electromagnetic wave velocity.
u	component of wind velocity in the along-wind direction.
u_*	reference wind velocity.
v	horizontal component of wind velocity in the cross-wind direction.
w	vertical wind component.
x	horizontal length along optical path.
z	vertical dimension.
z_0	surface roughness parameter.
A	instantaneous amplitude of electromagnetic wave after propagation through turbulence.
A_0	undisturbed amplitude of electromagnetic wave.
B_A	correlation function for electromagnetic wave amplitude.
$C_{n,T}$	structure function coefficients; n for refractive index, T for temperature.

LIST OF SYMBOLS (Cont'd)

Symbol	Definition
$D_{V,n}(\vec{r})$	structure function; V for wind velocity, n for refractive index.
$D_S(\rho)$	spatial structure function.
$F_{A,S}$	two-dimensional spectral density in a plane normal to propagation path; A for electromagnetic wave amplitude, S for electromagnetic wave phase.
F_m	theoretical frequency of maximum power.
H	sensible heat flux by turbulence.
I	instantaneous value of light intensity after propagation through turbulence.
I_0	undisturbed value of light intensity.
$J_{0,1}$	Bessel function of the first kind, order zero, one.
K, $K_{H,M,n}$	turbulent transfer coefficient; H for heat, M for momentum, n for index of refraction.
L	optical path length.
L_0	outer scale of turbulence.
M	factor relating refractive index differential to temperature differential.
N	$(n-1) \times 10^6$.
$\overline{N}$	dissipation rate for inhomogeneities of conservative passive additives in turbulent flow.
P	total light flux through an aperture after propagation through turbulence.
P_0	undisturbed total light flux through an aperture.
Pm	scintillation percent modulation.
R	radius of aperture.
$R_A(\tau)$	time correlation function.
Ri	Richardson number.
T	temperature.
T_1	temperature at height 1.
T_*	reference temperature.
$\Delta T/\Delta z$	vertical temperature gradient obtained by finite differences.
$\overline{U}$	mean horizontal wind velocity.
U(f)	normalized power spectral density of light intensity fluctuations.
$U_P(f)$	normalized power spectral density of light intensity fluctuations measured by a receiver with aperture.

LIST OF SYMBOLS (Cont'd)

Symbol	Definition
V	wind velocity.
V_n	horizontal component of wind normal to optical path.
$W(f)$	power spectral density of light intensity fluctuations at a point in the plane of the receiver aperture.
$W_P(f)$	power spectral density of light intensity fluctuations measured by receiver with aperture of radius R.
α	wind direction.
γ_a	dry adiabatic lapse rate = 9.86×10^{-5} C cm^{-1}.
Γ	gamma function: $\Gamma(n) = \int_0^\infty x^{n-1} e^{-x} dx \quad (n>0)$.
ϵ	energy dissipation rate per unit mass.
θ	potential temperature.
κ	wave number for turbulent fluctuations.
λ	wave length of electromagnetic radiation.
ν	spectral amplitude of turbulent fluctuations.
π	3.1416
ρ	in eq 2.20 through 2.27, correlation length.
ρ	in eq 2.32 = $(R\sqrt{2\pi/\lambda L})$.
ρ_a	atmospheric density.
σ^2	theoretical variance.
σ_P^2	measured variance.
τ	in eq 2.25 through 2.28, time.
τ	turbulent horizontal shear stress/area = vertical momentum flux.
ϕ	unknown function.
$\overline{\chi}^2$	$[\overline{\ln(A/A_0)}]^2$
Ω	f/f_0

2. TATARSKI'S MODEL FOR OPTICAL PROPAGATION IN HOMOGENEOUS AND ISOTROPIC TURBULENCE NEAR THE GROUND*

The influence of turbulent fluctuations of refractive index on optical wave propagation has been comprehensively treated by Tatarski (1961).† Parts of his work are summarized here as a basis for analysis and interpretation of the laser scintillation and turbulence data presented in the following sections. Tatarski's model appropriate for the laser experiments is included in the referenced book with general solutions and with specific conditions not descriptive of those under investigation. The material was extracted from several chapters in an attempt to present a brief and coherent account of the significant steps for the following specific conditions:

1) Homogeneous and isotropic turbulence in which the index of refraction may be treated as a "conservative, passive additive";

2) Inner scale, ℓ_0, and outer scale, L_0, of turbulence of magnitude appropriate to satisfy the inequality

$$\ell_0 \ll \sqrt{\lambda L} \ll L_0 \qquad (2.1)$$

in which λ is the optical wave length and L the optical path length;

3) Average wind direction angle relative to the optical path much larger than the quantity $\sqrt{\lambda/L}$;

4) Plane, parallel and monochromatic optical waves.

In addition to the foregoing conditions there are a number of approximations which may restrict the application of his results. The analysis, nonetheless, appears to provide a firm basis from which to build a more general framework to understand and to predict the influence of atmospheric turbulence on laser propagation.

Derivation of the scintillation spectrum

Tatarski (p. 120) gives the following physical argument to show that diffraction effects dominate for the condition described by inequality 2.1:

"Let an obstacle with geometrical dimensions ℓ be located on the propagation path of a plane wave. At a distance L from this obstacle we obtain its image (shadow) with the same dimensions ℓ. At the same time, diffraction of the wave by the obstacle will occur. The angle of divergence of the diffracted (scattered) wave will be of order $\theta \sim \lambda/\ell$. At a distance L from the obstacle the size of the diffracted bundle will be of the order $\theta L \sim \lambda L/\ell$. Clearly, in order for the geometrical shadow of the obstacle not to be appreciably changed, it is necessary for the relation $\lambda L/\ell \ll \ell$ or $\sqrt{\lambda L} \ll \ell$ to hold. When there is a whole set of obstacles with different geometrical sizes, it is obviously necessary that this relation be satisfied for the smallest obstacles, which have the size ℓ_0. Applying a similar argument to the problem under consideration, we convince ourselves that the solutions".... of the equations of geometrical optics...." are valid only in the case

*by Donald J. Portman

†All Tatarski citations in this section refer specifically to the 1961 translation by R.A. Silverman of V.I. Tatarski's Wave propagation in a turbulent medium. New York: McGraw-Hill, 285 p.

where the inequality $\sqrt{\lambda L} \ll \ell_0$ is satisfied, where ℓ_0 is the inner scale of turbulence. In other words, the theory of amplitude and phase fluctuations based on the equations of geometrical optics is valid only for limited distances L satisfying the condition

$$L \ll L_{cr} = \frac{\ell_0^2}{\lambda}."$$

The analysis begins, therefore, with the electromagnetic wave equation

$$\Delta u + k^2 n^2 (\vec{r}) u = 0 \qquad (2.2)$$

in which u represents any field component, $k(=2\pi/\lambda)$ wave number, n index of refraction and $\vec{r}$ position vector. Tatarski solves eq 2.2 by the Rytov method of small and smooth perturbations and the application of spectral expansions. For a locally isotropic random field, $n_1(\vec{r})$,* made up of spectral amplitudes, dr, the spectral amplitude, da, of the wave amplitude perturbation, $\ln(A/A_0)$, is given by

$$da(\kappa_2, \kappa_3, x) = k \int_0^x dx' \sin\left[\frac{\kappa^2 (x-x')}{2k}\right] d\nu(\kappa_2, \kappa_3, x') \qquad (2.3)$$

and for the spectral amplitude, $d\sigma$, of the phase fluctuations,

$$d\sigma(\kappa_2, \kappa_3, x) = k \int_0^x dx' \cos\left[\frac{\kappa^2 (x-x')}{2k}\right] d\nu(\kappa_2, \kappa_3, x'). \qquad (2.4)$$

Eq 2.3 and 2.4 show that the spectral amplitude at wave number κ is due to combined effects of all index of refraction inhomogeneities of the same wave number. The influence of each, however, is controlled by its size (equivalent wave length $\ell = 2\pi/\kappa$) and distance from the receiver (x-x') by the term $\sin[\kappa^2 (x-x')/2k]$.

Substitution, simplification and integration yield the two-dimensional spectral densities $F_A(\kappa_2, \kappa_3, 0)$ of $\ln(A/A_0)$ and $F_S(\kappa_2, \kappa_3, 0)$ of phase fluctuations in terms of the three-dimensional spectral density $\phi_n(0, \kappa_2, \kappa_3)$ of the refractive index fluctuations:

$$F_A(\kappa_2, \kappa_3, 0) = \pi k^2 L\left(1 - \frac{k}{\kappa^2 L} \sin\frac{\kappa^2 L}{k}\right)\phi_n(0, \kappa_2, \kappa_3) \qquad (2.5)$$

$$F_S(\kappa_2, \kappa_3, 0) = \pi k^2 L\left(1 + \frac{k}{\kappa^2 L} \sin\frac{\kappa^2 L}{k}\right)\phi_n(0, \kappa_2, \kappa_3). \qquad (2.6)$$

---

*$n_1(\vec{r}) = n(\vec{r}) - 1$ and it is assumed that $|n_1(\vec{r})| \ll 1$.

For isotropic refractive index fluctuations, i.e., $\phi_n(0, \kappa_2, \kappa_3) = \phi_n(\kappa)$

$$F_A(\kappa, 0) = \pi k^2 L \left(1 - \frac{k}{\kappa^2 L} \sin \frac{\kappa^2 L}{k}\right) \phi_n(\kappa) \qquad (2.7)$$

$$F_S(\kappa, 0) = \pi k^2 L \left(1 + \frac{k}{\kappa^2 L} \sin \frac{\kappa^2 L}{k}\right) \phi_n(\kappa). \qquad (2.8)$$

Figure 2, taken from Tatarski (Fig. 11, p. 140), shows the relative positions of the functions $\phi_n(\kappa)$ and

$$f(\kappa) = \left(1 - \frac{k}{\kappa^2 L} \sin \frac{\kappa^2 L}{k}\right)$$

which comprise the spectral density of the logarithmic amplitude fluctuations for a given k and L.

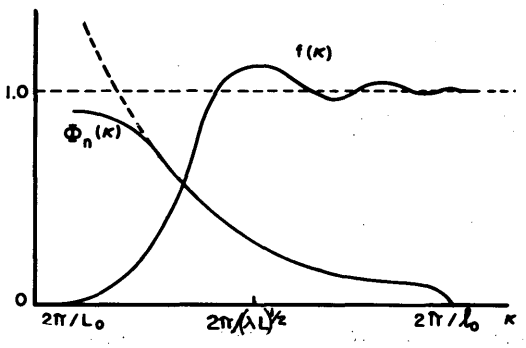

Figure 2. Relative position of the curves $\phi_n(\kappa)$ and $f(\kappa) = \left(1 - \frac{k}{\kappa^2 L} \sin \frac{\kappa^2 L}{k}\right)$ for $\ell_0 \ll \sqrt{\lambda L} \ll L_0$.

It is apparent that the index of refraction fluctuations of size $(\lambda L)^{\frac{1}{2}}$ are the most effective in causing fluctuations in wave amplitude and it is clear, furthermore, that $f(\kappa)$ effectively diminishes the influence of low wave number refractive index fluctuations. The latter fact is significant for the further development of quantitative relationships.

Atmospheric turbulence and associated fluctuations of conservative, passive additives which are not thoroughly mixed are in general not isotropic (i.e., their statistical properties depend on reference frame orientation). Their spectral densities, furthermore, may vary widely in dependence on wave number. For a certain range of relatively high wave number atmospheric turbulence, however, there is evidence that both velocity and conservative passive additive spectra conform to the Kolmogorov (1941) hypothesis. This hypothesis states that for turbulence generated at sufficiently high Reynolds number, there exists a high wave number region (the inertial subrange) in which the turbulence is isotropic and the spectral characteristics depend only on the turbulent energy dissipation rate, ε. The concept applies to an equilibrium situation in which the rate of turbulent energy production, at the largest scale, L_0, is equivalent to the rate of energy dissipation into viscosity at the smallest scales of turbulence, i.e., at wave lengths on the order of ℓ_0.

Kolmogorov postulated, in addition, that in the wave number region between the inertial subrange and the microscale (ℓ_0) the turbulence is isotropic and that its spectral characteristics depend on the fluid (molecular) viscosity as well as on the energy dissipation rate. Dimensional

analysis is made in terms of the structure function of the velocity field, $D_V(\vec{r})$, defined as

$$D_V(\vec{r}) = \overline{[V(\vec{r}_1) - V(\vec{r}_2)]^2} \tag{2.9}$$

in which the velocity V is a function of position vector $\vec{r}$. The result for the inertial subrange with the condition $\ell_0 << r << L$ is

$$D_V(r) \propto r^{\frac{2}{3}} \tag{2.10}$$

and for $r << \ell_0$

$$D_V(r) \propto r^2 . \tag{2.11}$$

It can be shown that proportionality 2.10 (the "two-thirds" law) corresponds to the three-dimensional spectral density

$$\phi(\kappa) \propto \kappa^{-11/3} \tag{2.12}$$

and the one-dimensional spectral density

$$\phi(\kappa) \propto \kappa^{-5/3} . \tag{2.13}$$

Obukhov (1949) showed that the "two-thirds" law would also apply to a conservative, passive additive imbedded in turbulence characterized by the isotropic, equilibrium range. Thus, if refractive index is so regarded,

$$D_n(r) = C_n^2 r^{\frac{2}{3}} \tag{2.14}$$

for $\ell_0 << r << L_0$

and, similarly, the spectrum of refractive index fluctuations is given by

$$\phi_n(\kappa) = 0.033 C_n^2 \kappa^{-11/3} \tag{2.15}$$

for the inertial subrange.*

The refractive index structure function coefficient, C_n^2, plays a significant role in Tatarski's analysis of turbulence effects on propagation; its characteristics are discussed on page 15.

*The coefficient 0.033 derives from the relationship between $D_n(r)$ and $\phi_n(\kappa)$. If $D(r) = C^2 r^P$ for $0 < P < 2$ then $\phi(\kappa) = \frac{\Gamma(P+2)}{4\pi^2} \sin\frac{\pi P}{2} C^2 \kappa^{-(P+3)}$.

The analysis of amplitude and phase fluctuations continues with the substitution of eq 2.15 for $\phi_n(\kappa)$ in eq 2.7 and 2.8.

$$F_A(\kappa, 0) = 0.033\pi C_n^2 k^2 L\left(1 - \frac{k}{\kappa^2 L} \sin\frac{\kappa^2 L}{k}\right)\kappa^{-11/3}. \qquad (2.16)$$

and

$$F_S(\kappa, 0) = 0.033\pi C_n^2 k^2 L\left(1 + \frac{k}{\kappa^2 L} \sin\frac{\kappa^2 L}{k}\right)\kappa^{-11/3}. \qquad (2.17)$$

Tatarski writes eq 2.16 and 2.17 for $\kappa < \kappa_m$. κ_m is a fictitious cutoff point below which eq 2.15 applies and above which turbulent contributions are negligible. He reasons that $\kappa_m \cong 5.5/\ell_0$.

From eq 2.16 it is possible to calculate the mean square fluctuation of logarithmic amplitude at a point in the plane x = L and obtain, with $\overline{\chi}^2 = \overline{[\ln(A/A_0)]^2}$,

$$\overline{\chi}^2 = 2\pi^2 (0.033) C_n^2 k^2 L \int_0^\infty \left(1 - \frac{k}{\kappa^2 L} \sin\frac{\kappa^2 L}{k}\right)\kappa^{-8/3} d\kappa. \qquad (2.18)$$

By calculating the integral, Tatarski finally obtains

$$\overline{\chi}^2 = 0.31 C_n^2 k^{7/6} L^{11/6} \quad (\sqrt{\lambda L} >> \ell_0). \qquad (2.19)$$

For a spherical wave front of monochromatic radiation propagating through isotropic and homogeneous turbulence Tatarski shows that $\overline{\chi}^2 = 0.13 C_n^2 k^{7/6} L^{11/6}$.

Eq 2.17 leads to similar expressions for phase fluctuations which are given in terms of the spatial structure function, $D_S(\rho)$, for two separate conditions; vis.,

$$D_S(\rho) = 2.91 k^2 L C_n^2 \rho^{5/3} \quad (\rho \gtrsim \sqrt{\lambda L}) \qquad (2.20)$$

and

$$D_S(\rho) = 1.46 k^2 L C_n^2 \rho^{5/3} \quad (\ell_0 << \rho << \sqrt{\lambda L}). \qquad (2.21)$$

Eq 2.18 and 2.19 can be used to describe light intensity variations on the plane x = L through the relation

$$\ln\left(\frac{I}{I_0}\right) = 2\ln\left(\frac{A}{A_0}\right). \qquad (2.22)$$

If, as Tatarski assumes, both $\ln(I/I_0)$ and $\ln(A/A_0)$ are normally distributed,

$$\sigma^2 \equiv \overline{\left(\ln \frac{I}{I_0}\right)^2} = 4\overline{\chi}^2 , \tag{2.23}$$

and from eq 2.19

$$\sigma^2 = 1.23 C_n^2 k^{7/6} L^{11/6} . \tag{2.24}$$

Eq 2.24 provides for the conditions listed above a general relationship between intensity scintillation and (1) wave length of light, (2) optical path length and (3) the intensity of turbulent fluctuations of refractive index as expressed by C_n^2.

Scintillation is usually observed as fluctuating light intensity at an aperture on the plane x = L. To obtain an expression for the frequency spectrum that would be observed with an infinitesimally small aperture for the conditions listed above, it is convenient to begin with the Fourier transform relation between the frequency spectrum function W(f) and the time correlation function $R_A(\tau)$

$$W(f) = 4 \int_0^\infty \cos(2\pi f\tau)\, R_A(\tau) d\tau . \tag{2.25}$$

For the condition of the angle between mean wind direction and optical path much larger than the quantity $(\lambda / L)^{\frac{1}{2}}$ and for the assumption "that the field at the point (y_0, z_0) at the time $t_0 + \tau$ coincides with the field at the point $(y_0 - v_y\tau,\ z_0 - v_z\tau)$ at the time t_0," (Tatarski, p. 215) the time correlation function may be equated to the space correlation function, $B_A(V_n\tau)$, so that

$$W(f) = 4 \int_0^\infty \cos(2\pi f\tau)\, B_A(V_n\tau) d\tau . \tag{2.26}$$

The two-dimensional correlation function $B_A(\rho)$ may be expressed in terms of the two-dimensional spectral density $F_A(\kappa, 0)$ by the relation

$$B_A(\rho) = 2\pi \int_0^\infty F_A(\kappa, 0)\, J_0(\kappa\rho)\kappa d\kappa \tag{2.27}$$

in which $J_0(\kappa\rho)$ is the Bessel function of the first kind of order zero. Substitution in eq 2.26 and rearrangement gives

$$W(f) = 8\pi \int_0^\infty F_A(\kappa, 0)\,\kappa d\kappa \int_0^\infty J_0(\kappa V_n \tau)\cos(2\pi f\tau)d\tau. \qquad (2.28)$$

Finally, by calculating the second integral and substituting, Tatarski obtains

$$W(f) = \frac{8\pi}{V_n} \int_0^\infty F_A\left(\sqrt{\kappa^2 + \frac{4\pi^2 f^2}{V_n^2}}, 0\right)d\kappa. \qquad (2.29)$$

Eq 2.29 gives the relationship between the frequency spectrum and the two-dimensional spectral density of the electromagnetic wave amplitude fluctuations. The latter is related to the three-dimensional refractive index spectral density by eq 2.7.

To compare experimental data with the above result, Tatarski uses the normalized spectrum

$$U(f) = \frac{fW(f)}{\bar{\chi}^2} \qquad (2.30)$$

in which eq 2.29 is substituted for W(f), eq 2.16 for $F_A(\kappa, 0)$, and eq 2.19 for $\bar{\chi}^2$. The result is

$$U(f) = 1.35\,\Omega \int_0^\infty \left[1 - \frac{\sin(t^2+\Omega^2)}{t^2+\Omega^2}\right](t^2+\Omega^2)^{-11/6}dt \qquad (2.31)$$

in which $t = \kappa(L/k)^{\frac{1}{2}}$

$\Omega = f/f_0$

$f_0 = V_n(2\pi\lambda L)^{-\frac{1}{2}}$.

Tatarski displays the scintillation frequency spectrum represented by eq 2.31 in two ways. His Figure 28, p. 218, shows $f_0 W(f)/\bar{\chi}^2$ vs $\ln(f/f_0)$ and Figure 31, p. 222 (curve 1), shows U(f) vs lnf. Similar curves are reproduced in Figures 3 and 4 from data given in Table I. They were obtained by numerical integrations of eq 2.31 with the aid of a digital computer. For Figure 4, 1 m/sec was used for V_n and 1.78 cm for $\sqrt{\lambda L}$.

The practical question of the influence of the size of a telescope diaphragm on the scintillation that may be observed under the conditions of interest here is dealt with by Tatarski in his Chapter 13. The analysis is made for the case of scintillation observed by a photocell placed at the focal point of an objective. In this situation the photocell receives all the light incident on the aperture area and therefore the total scintillation observed decreases with increase in size of the diaphragm. A second effect is the shifting of the scintillation spectrum toward lower frequencies since

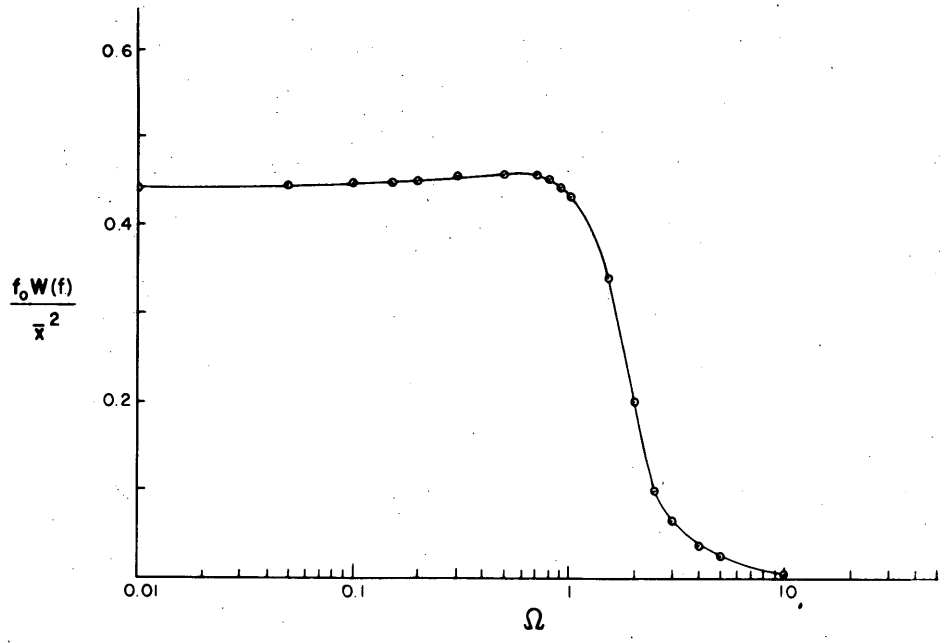

Figure 3. Tatarski's spectrum of fluctuations of logarithmic amplitude for constant wind velocity.

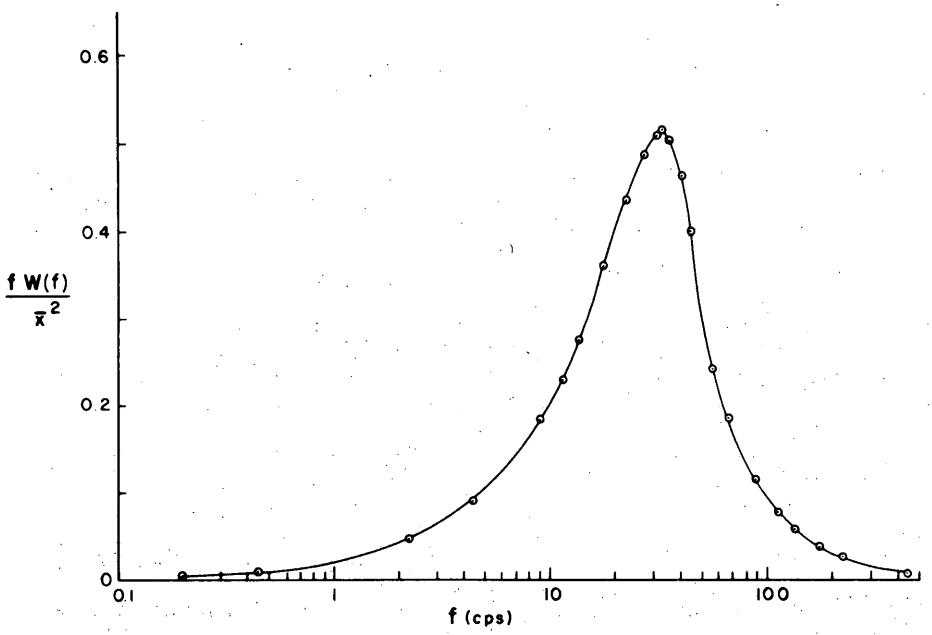

Figure 4. Tatarski's normalized spectrum of fluctuations of logarithmic amplitude obtained by numerical integration of eq 2.31 for V_n = 1 m/sec and $\sqrt{\lambda L}$ = 1.78 cm.

Table I. Spectral data from numerical integrations of eq 2.31 (V_n = 1 m/sec, $\sqrt{\lambda L}$ = 1.78 cm).

Ω	f (cps)	$fW(f)/\overline{\chi}^2$	$f_0 W(f)/\overline{\chi}^2$
.005	0.11	.002	.441
.010	0.22	.004	.441
.020	0.45	.009	.442
.100	2.24	.045	.446
.200	4.49	.090	.450
.400	8.97	.183	.458
.500	11.21	.229	.459
.600	13.46	.275	.459
.800	17.90	.360	.450
1.000	22.43	.434	.434
1.200	26.91	.486	.405
1.400	31.39	.510	.364
1.450	32.52	.511	.352
1.600	35.89	.502	.314
1.800	40.37	.462	.257
2.000	44.86	.399	.199
2.500	56.07	.240	.096
3.000	67.28	.186	.062
4.000	89.71	.114	.029
5.000	112.14	.077	.015
6.000	134.57	.058	.010
8.000	179.42	.035	.004
10.000	224.28	.024	.002
15.000	336.42	.012	.001

the averaging effect is most marked for fluctuations characterized by scales smaller than the aperture diameter. The result is obtained in terms of a normalized spectrum analogous to eq 2.31

$$\frac{fW_P(f)}{\sigma^2} = 1.35\Omega \int_0^\infty \left[1 - \frac{\sin(t^2+\Omega^2)}{t^2+\Omega^2}\right](t^2+\Omega^2)^{-11/6} \times$$

$$\times \left[\frac{2J_1(\rho\sqrt{t^2+\Omega^2})}{\rho\sqrt{t^2+\Omega^2}}\right]^2 dt \qquad (2.32)$$

in which $W_P(f)$ is the spectral density observed with an aperture of radius R, $\rho = \sqrt{2\pi/\lambda L}\ R$, and $\sigma^2 = [\overline{\ln(I/I_0)}]^2$. Equation 2.32 is used in a following section as a basis for comparing measured laser scintillation spectra and for studying the effects of anisotropic turbulence.

C_n^2 and its relation to turbulence parameters

Tatarski uses the theories of Obukhov (1949) and Yaglom (1949) to show that the refractive index structure function coefficient can be expressed in terms of the mean velocity and refractive index gradients and the turbulent transfer coefficient, K. First it is shown, with dimensional reasoning, that

$$C_n^2 = a^2 \overline{N} \, \varepsilon^{-\frac{1}{3}}. \tag{2.33}$$

a^2 is a coefficient whose value may be related to the Richardson number. $\overline{N}$ is a measure of the rate of dissipation of refractive index inhomogeneities and may be expressed as

$$\overline{N} = K\left(\frac{\partial N}{\partial z}\right)^2. \tag{2.34}$$

It is assumed that the rate of creation of inhomogeneities equals the rate of their dissipation in analogy with the Kolmogorov (1941) equilibrium concept. The mechanical energy dissipation rate for the equilibrium condition is given by

$$\varepsilon = K\left(\frac{\partial \overline{U}}{\partial z}\right)^2 \tag{2.35}$$

when mean wind shear $(\partial \overline{U}/\partial z)$ is the only mechanism creating turbulence. Eq 2.34 and 2.35 apply when horizontal gradients in wind and refractive index are negligible as they may be for many natural atmospheric conditions of interest. Substitution of eq 2.34 and 2.35 in eq 2.33 gives

$$C_n^2 = a^2 K^{\frac{2}{3}} \left(\frac{\partial \overline{U}}{\partial z}\right)^{-\frac{2}{3}} \left(\frac{\partial N}{\partial z}\right)^2. \tag{2.36}$$

To make use of eq 2.36 it is necessary to express $(\partial N/\partial z)$ in terms of atmospheric variables commonly measured, i.e., pressure, p, temperature, T, or potential temperature, θ, and specific humidity, q. Tatarski chooses the relationship

$$(n-1) \times 10^6 = N = \frac{79p}{\theta - \gamma_a z}\left(1 + \frac{7800q}{\theta - \gamma_a z}\right) \tag{2.37}$$

in which γ_a is the dry adiabatic lapse rate. The difference between the index of refraction of a parcel of air displaced in the vertical from its equilibrium position, by a turbulent motion, and its new environment may be approximated by

$$\delta N \sim \left(\frac{\partial N}{\partial \theta}\frac{\partial \theta}{\partial z} + \frac{\partial N}{\partial q}\frac{\partial q}{\partial z}\right)\delta z$$

because θ and q may be regarded as conservative properties of the parcel during displacement. If

$$M = \left(\frac{\partial N}{\partial \theta}\frac{\partial \theta}{\partial z} + \frac{\partial N}{\partial q}\frac{\partial q}{\partial z}\right) \times 10^{-6}$$

then, from eq 2.37

$$M = \frac{-79 \times 10^{-6} p}{T^2} \left(1 + \frac{15500q}{T}\right)\left[\left(\frac{dT}{dz} + \gamma_a\right) - \right.$$

$$\left. - \frac{7800}{1 + \frac{15500q}{T}} \frac{dq}{dz}\right]. \qquad (2.38)$$

The terms involving specific humidity are often negligible in real situations so that eq 2.38 becomes

$$M = \frac{-79 \times 10^{-6} p}{T^2} \frac{\partial \theta}{\partial z} \qquad (2.39)$$

in which the relation

$$\theta = T + \gamma_a z$$

has been used. Eq 2.36, with substitution of eq 2.39, becomes

$$C_n^2 = \left[\frac{-79 \times 10^{-6} p}{T^2}\right]^2 a^2 K^{\frac{2}{3}} \left(\frac{\partial \overline{U}}{\partial z}\right)^{-\frac{2}{3}} \left(\frac{\partial \theta}{\partial z}\right)^2 . \qquad (2.40)$$

Except for the term $(-79 \times 10^{-6} p/T^2)^2$ eq 2.40 is identical to an expression that can be derived for the structure function coefficient for the temperature inhomogeneities in the inertial subrange:

$$C_T^2 \cong a^2 K^{\frac{2}{3}} \left(\frac{\partial \overline{U}}{\partial z}\right)^{-\frac{2}{3}} \left(\frac{\partial \theta}{\partial z}\right)^2 . \qquad (2.41)$$

It is found expedient to discuss the influence of refractive index fluctuations on optical propagation in terms of C_T^2, $\partial\theta/\partial z$, and K because there exist very few data on C_n^2. In the development so far, it has been assumed that a single transfer coefficient is applicable to turbulent diffusion of momentum, index of refraction, and heat. It is generally accepted in micrometeorological analyses, however, that the transfer coefficient for momentum, K_M, and that for heat, K_H, are not identical except for small values of $\partial\theta/\partial z$, i.e., when the turbulent motion is not significantly influenced by buoyancy forces. This means that eq 2.36 and 2.41 are strictly correct only when the optical effects of turbulence are weak.

In the absence of buoyancy effects in shear flow it is possible to relate the momentum transfer coefficient, K_M, to the wind shear by dimensional reasoning and obtain

$$K_M = k_v^2 z^2 \frac{\partial \overline{U}}{\partial z} \qquad (2.42)$$

in which $k_v \approx 0.41$, the von Karman number.

Substitution in eq 2.41 with $K = K_M$ gives

$$C_T^2 \cong a^2 k_v^{4/3} z^{4/3} \left(\frac{\partial \theta}{\partial z}\right)^2 . \tag{2.43}$$

Tatarski carries the argument further for the near-adiabatic condition ($\partial\theta/\partial z$ not far from zero) by invoking the hypothesis of similarity of wind and temperature gradients, i.e., the ratio

$$\frac{\partial \overline{U}/\partial z}{\partial \theta/\partial z}$$

is assumed constant with height. In this case $\overline{\theta}(z)$ has the same form as $\overline{U}(z)$ and dimensional argument backed by many empirical results gives

$$\overline{U}(z) = \frac{u_*}{k_v} \ln \frac{z}{z_0} \tag{2.44}$$

and

$$\overline{\theta}(z) = \text{const} + T_* \ln \frac{z}{z_0} \tag{2.45}$$

in which u_* is the "friction" or "reference" velocity, T_* the analogous reference temperature and z_0 the "roughness" length. The reference velocity is related to the momentum flux and T_* to the heat flux H by the relations

$$\tau = \rho u_*^2 \tag{2.46}$$

$$H = \rho c_p T_* . \tag{2.47}$$

Differentiation of eq 2.45 gives

$$\frac{\partial \theta}{\partial z} = \frac{T_*}{z} \tag{2.48}$$

and by substitution into eq 2.43, finally, Tatarski gets

$$C_T^2 = a^2 k_v^{4/3} z^{-\frac{2}{3}} T_*^2 . \tag{2.49}$$

Tatarski used eq 2.49 to correlate a large number of simultaneous measurements of C_T and temperature profiles and the results are shown in his Figure 16, p. 195. Good correlation is found for $\partial\theta/\partial z < 0$ (unstable thermal stratification) with the constant, a, determined to be 2.4. The agreement is not so good, however, for stable stratification, $\partial\theta/\partial z > 0$, and he suggests use of the empirical curve to estimate C_T from temperature profile data for that condition.

It should be recognized that Tatarski's data shown in his Figure 16 cover a relatively limited range of thermal stability and that the scatter of points seems to increase with magnitude of $\partial\theta/\partial z$ as one would expect. The effect is clearly evident in the data shown in his Figure 17, p. 197, in which it can be seen that the measured C_T values are greater than the computed ones by a factor of about two for the midday period when $\partial\theta/\partial z$ is greatest. One may conclude that eq 2.49 may be used to estimate C_T from temperature gradient data in the surface layer of the atmosphere when the absolute magnitude of $\partial\theta/\partial z$ is not great. This condition occurs near the ground when it is overcast and windy (either day or night) and for short periods before sunset and after sunrise on cloudless days.

3. FIELD EXPERIMENTS AND RESULTS*

Field experiment plan

Field experiments were designed for simultaneous measurements of (1) intensity and frequency of laser scintillation, (2) profiles† of temperature and wind speed, (3) fluctuations of wind velocity (three components) and (4) wind direction. They were conducted at the University of Michigan's field station for micrometeorological research located near the east edge of the infield portion of Willow Run Airport. The airport itself is a 1000-acre level and uniform tract of land about 1 mile wide (N-S) and 1.5 miles long (E-W). A list of the observation periods and general weather conditions for them is given in Table II.

Table II. Observation periods and weather summaries, Willow Run Field Station, 1965.

Date	Time (EST)	Cloudiness	Avg wind vel (mph)	Avg temp (°C)
21 Jan	1220-1320	1200 ft sctd	SW 12	-9
	1439-1450	Clear		-6
	1837-1906			-5
	2043-2117			-4
29 Apr	1350-1515	Clear	W 10+15	+21
	2022-2122			+11
3 May	1530-1650	Hi thin sctd	SW 15+25	+31

For reasons given below, field experiments were performed only during (1) steady weather conditions and (2) average wind directions between southwest and northwest. It was reasonable to expect, therefore, that as a result of condition (1) there would be the desirable stationarity of wind and temperature structures for time intervals long enough to obtain meaningful spectral estimates of scintillation and turbulence components. As a result of condition (2), it could be expected that there would be the desirable statistical homogeneity throughout the length of the optical path because the

*by Edward Ryznar

† The word profile means the time average vertical distribution of a variable such as wind or temperature.

air would have passed over nearly uniform roughness for several hundred meters before it moved through the optical path and past the wind and temperature sensors.

With these conditions fulfilled, the statistical properties of the meteorological parameters during each observation period were independent of the horizontal position of measurement and of time and depended only on the height of measurement. In this way it was possible to obtain representative scintillation and turbulence data for different but steady meteorological conditions.

Optical measurements

Scintillation data were obtained with a laser and receiver separated by a 500-m horizontal optical path 1 m high. All laser scintillation measurements were made with a Spectra-Physics Model 115 continuous-wave helium-neon gas laser with an output wavelength of 0.6328 microns. It was operated in a plane-parallel mode and had an output of 0.8 milliwatts. The diameter of the laser beam increased from about 0.35 cm to 20 cm for the 500-m optical path.

The optical receiver was the photometer described in detail in USA CRREL Research Report 111, Part I. It consisted of a DuMont type 6467 multiplier phototube located at the focus of a lens system. The phototube provided an electrical analog of the luminous flux at the objective lens of the photometer. The following improvements in the photometer were made for use in the present experiment:

(1) The aperture diameter was decreased to 0.7 cm to minimize an averaging effect of an aperture, and

(2) A spectral filter with a peak transmittance of 79% at 0.6338 microns and 76% transmittance at 0.6328 microns was included within the photometer to eliminate most background light having wavelengths other than that of the laser.

Components of the optical recording system were similar to those described in detail in USA CRREL Research Report 111, Part I but were upgraded for use in the present field experiments in the following ways:

(1) A facility was built to record the a-c component (the component of the received signal due to fluctuations in light intensity) directly on magnetic tape instead of on a strip chart recorder as in previous experiments;

(2) The facility used only to indicate the d-c level (the component of the received signal due to the average brightness of the source) was modified and the d-c level was recorded on an Esterline-Angus 0-1 ma recorder;

(3) A vacuum tube voltmeter was built into the system to provide a means of monitoring the signal at various points in the circuit;

(4) A stable and adjustable power supply necessary for the electronics was built and included in the system;

(5) All components listed above were enclosed in one portable unit.

Wind and temperature measurements

Wind and temperature profiles and wind direction were measured continuously throughout all periods of scintillation measurement. The profiles were measured with sensors at heights of 0.5, 1, 2, and 4 m and wind direction was measured at 1 m.

Temperature and wind profiles were measured with equipment similar to that described in detail in USA CRREL Research Report 111, Part I. The thermocouple circuit was designed to measure temperature differences for three height intervals: 4 to 0.5, 4 to 1, and 4 to 2 m. The differences were recorded together with the absolute temperature at 4 m in sequence in $\frac{1}{3}$-minute intervals on a Honeywell ElectroniK 17 recorder. A Leeds and Northrup d-c amplifier was used to provide a choice of recorder ranges of 6.25, 12.5, or 25 C full-scale deflection, depending on the magnitude of the existing vertical temperature gradient. The first two ranges were used in the field experiments and gave a resolution of either 0.06 or 0.125 C per recorder chart scale division.

Four matched Beckman and Whitley Model 170-34 anemometers were used to measure wind speed profiles and a Beckman and Whitley wind vane measured wind direction at the 1-m height of the optical path.

Turbulence data were obtained with hot-wire anemometers mounted at a height of one meter and oriented to measure longitudinal (along-wind) and transverse (horizontal and vertical) components of wind speed fluctuations. Major components of the system were (1) a hot-wire amplifier unit designed by Kovasznay (1963) and (2) Flow Corporation hot-wire probes.* The latter were orthogonal pairs (X-probes) of tungsten wires whose diameters were about 4×10^{-5} cm and effective lengths 0.25 cm. With a combination of two X-probes mounted in close proximity, it was possible to obtain the three components u, v, and w of the wind vector simultaneously. The time constant of individual wires was about 4×10^{-4} sec so that the scales of turbulence significant for scintillation could be measured.

Data recording and processing

All scintillation and turbulence data except for the d-c voltage from the photometer were recorded simultaneously on a 7-channel Ampex SP-300 Instrumentation Tape Recorder. Four channels were used for turbulence data, one for a signal for monitoring time, and one for the photometer signal.

The hot-wire data were processed with an electronic computer system using both analogue and digital techniques. From the voltages produced by the four hot-wire amplifiers, the processing yielded a voltage analogue for each of the velocity components, u', v', and w'. A frequency spectrum was then obtained for each component by the method described in Appendix A. Estimates of the spectral densities for five periods during which laser scintillation was measured are shown in logarithmic coordinates in Figure 5.

The method of processing the scintillation spectral data is discussed in Appendix A of the present report. The final output of the method was the number of millivolts for each of 28 frequencies between 1.25 and 1000 cps for a given 6-minute recording of the a-c signal. The procedure was then (1) to compensate for effects of filters in the photometer, photometer range,

*The amplifier units were obtained from Leslie T. Miller, 310 Regester Avenue, Baltimore, Maryland, and the hot-wire probes from Flow Corporation, 127 Coolidge Hill Road, Watertown, Massachusetts.

attenuation range, wave analyzer bandwidth, and d-c (average brightness) level, since some of these varied from period to period, (2) to square the compensated millivolts at each frequency to get spectral density, $W_P(f)$, (3) to multiply (2) by each frequency to obtain $fW_P(f)$, (4) to graph $fW_P(f)$ as the ordinate on a linear scale against frequency on a log scale, and (5) to measure (with a planimeter) the area under the curve between frequencies of 1.25 and 1000 cps to get

$$\sigma_P^2 \cong \int_{1.25}^{1000} W_P(f)df = \int_{1.25}^{1000} fW_P(f)d(\ln f).$$

σ_P^2 is thus the variance obtained by integrating the spectral density $W_P(f)$. The subscript P denotes the fact that measurements were made with a photometer whose aperture diameter was not negligible.

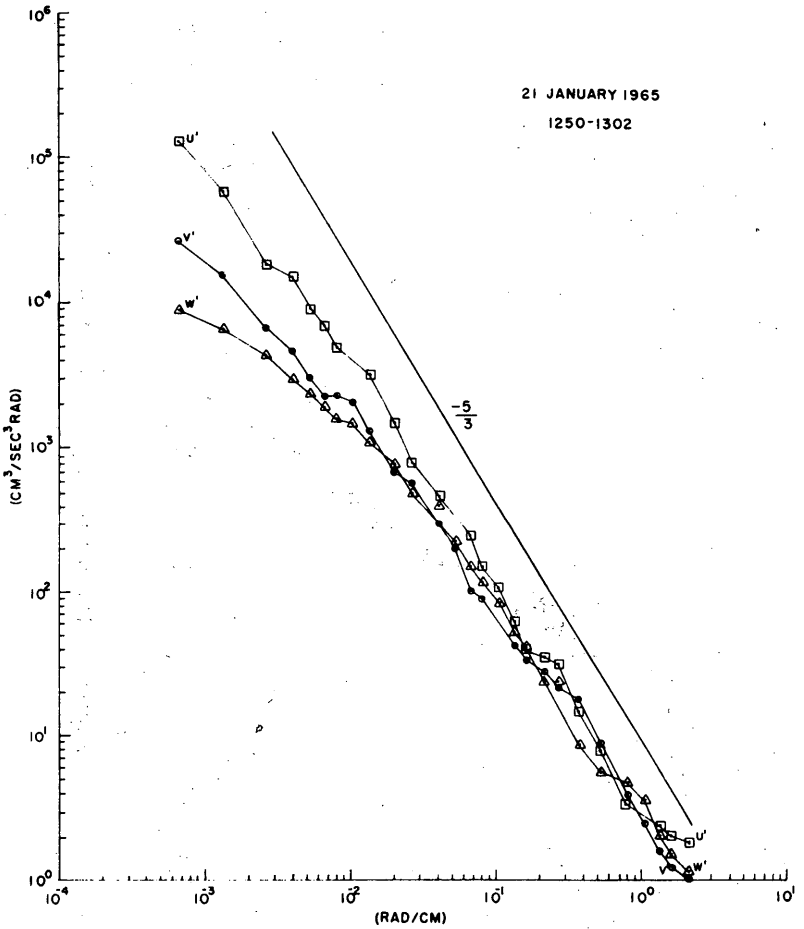

Figure 5. Spectral densities for u', v', and w' wind components.

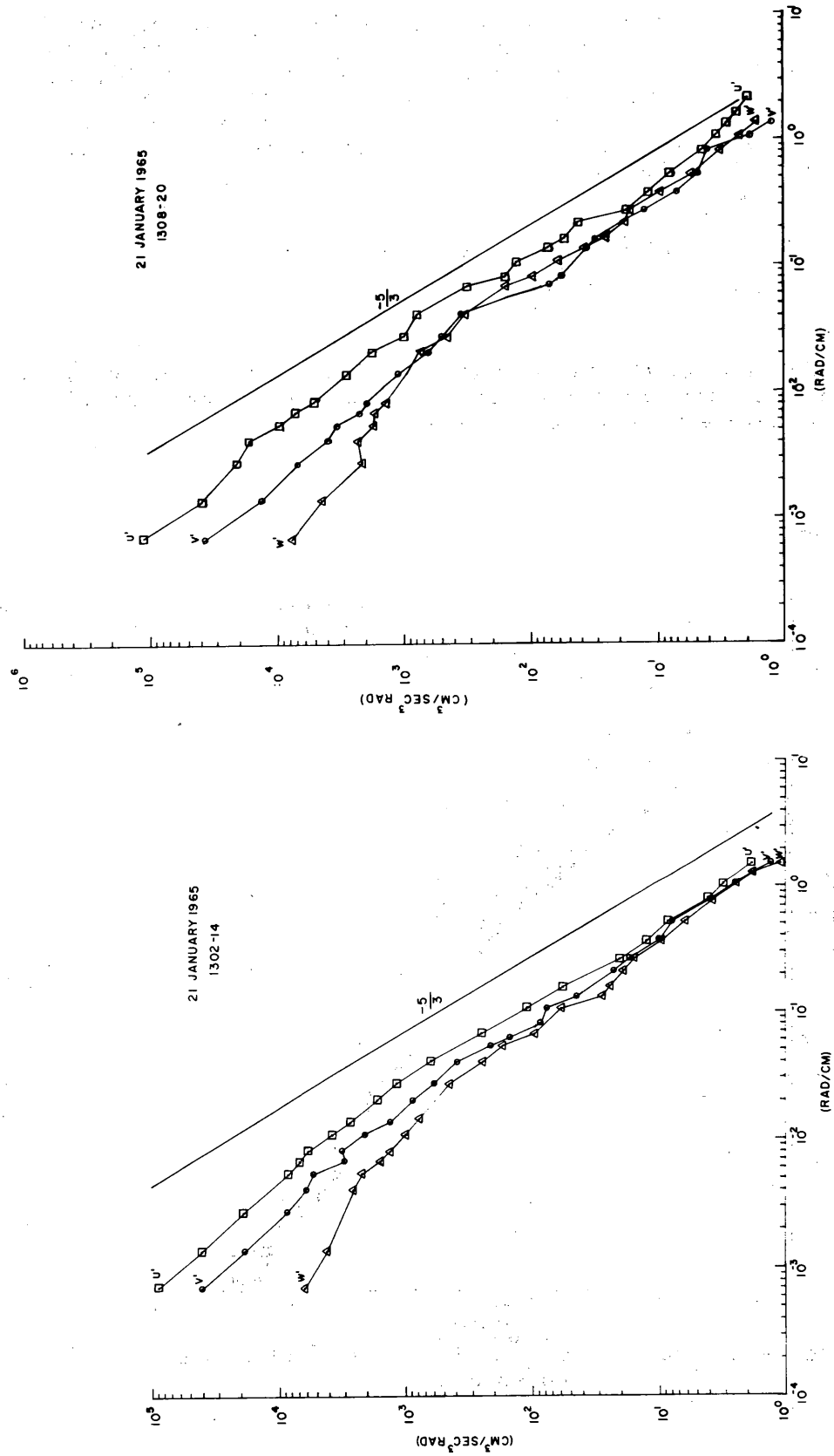

Figure 5 (Cont'd). Spectral densities for u', v', and w' wind components.

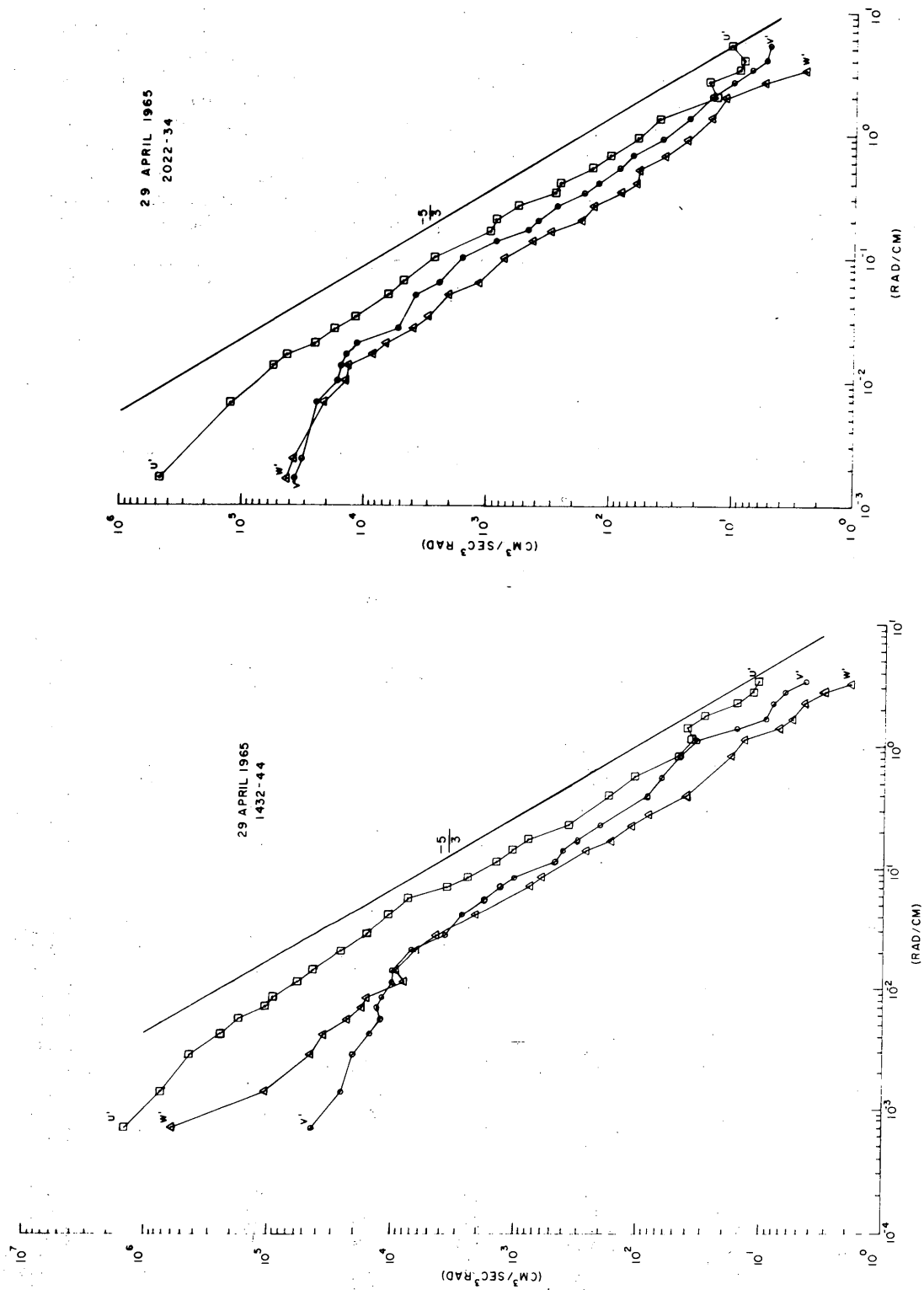

Figure 5 (Cont'd). Spectral densities for u', v', and w' wind components.

Scintillation spectral data

Scintillation spectral data for thirty-seven 6-minute and two 12-minute periods are given in Table III along with various turbulence parameters derived from coincident wind and temperature measurements. All symbols are defined on p. 3-5. The values for the turbulence parameters are valid for the 1-m height of the optical path. A negative $T_{1.4} - T_{0.7}$, Ri, or C_T means an unstable lapse rate. All spectra are for 6-minute periods and cover a frequency range of 1.25 to 1000 cps except for two 12-minute spectra beginning at 1837 and 2043 EST on 21 Jan which cover a frequency range of 0.625 to 500 cps. (Ri and C_T were computed by methods described in Section 5.

The quantities $U_p(f) = fW_P(f)/\sigma^2_P$ and Ω were also computed for each spectrum listed in Table III and are shown in individual graphs in Figure 6. For the measured spectra,

$$f_0 = \frac{\overline{V}_n}{(2\pi\lambda L)^{\frac{1}{2}}} = \frac{\overline{V}_n}{4.4587}.$$

Since $\overline{V}_n$ varied from about 1.6 to 6.8 m sec^{-1}, f_0 varied from approximately 36 to 153 cps.

Table III. Turbulence parameters and scintillation spectral data, Willow Run Field Station, 1965.

Path length: 500 m Aperture diam: 0.7 cm
Path height: 1 m Path dir: 180-360 deg

Time (EST)	$T_{1.4} - T_{0.7}$ °C	Ri	C_T (°C cm$^{-\frac{1}{3}}$)	$\overline{U}$ (cm sec^{-1})	α (deg)	$\overline{V}_n$ (cm sec^{-1})	f_m (cps)	σ_p^2 (mv^2)
Date: 1/21								
1220-26	-0.20	-0.015	-0.059	551	218	339	238	0.339
1226-32	-0.16	-0.015	-0.023	511	222	339	246	0.406
1232-38	-0.13	-0.009	-0.018	549	242	486	257	0.366
1250-56	-0.18	-0.014	-0.057	576	218	355	229	0.339
1256-02	-0.12	-0.009	-0.017	595	210	295	247	0.346
1308-14	-0.12	-0.009	-0.017	575	214	319	243	0.250
1314-20	-0.27	-0.017	-0.039	601	214	336	286	0.216
1439-45	-0.07	-0.006	-0.019	635	219	408	248	0.217
1837-49	+0.16	+0.015	+0.047	488	202	183	144	3.199
2043-55	+0.14	+0.017	+0.041	407	207	219	184	2.449
Date: 4/29								
1350-56	-0.55	-0.022	-0.179	572	271	572	340	1.579
1356-02	-0.44	-0.018	-0.141	581	256	564	326	1.465
1402-08	-0.53	-0.013	-0.169	666	251	629	389	1.469
1408-14	-0.54	-0.012	-0.172	566	249	528	352	1.245
1414-20	-0.54	-0.016	-0.172	611	255	590	335	1.242
1420-26	-0.61	-0.039	-0.205	463	269	463	376	1.342
1426-32	-0.58	-0.021	-0.189	558	270	558	355	1.536
1432-38	-0.42	-0.009	-0.132	551	255	532	343	1.583
1438-44	-0.43	-0.015	-0.138	585	270	585	384	1.715
1444-50	-0.45	-0.019	-0.145	578	279	572	377	2.144
2022-28	+0.61	+0.058	+0.139	243	232	191	133	1.459
2028-34	+0.68	+0.081	+0.133	227	240	197	142	1.307
2034-40	+0.54	+0.059	+0.123	218	242	192	134	1.161
2040-46	+0.69	+0.089	+0.129	208	238	177	125	1.642
2046-52	+0.68	+0.077	+0.137	213	236	177	126	1.567
2052-58	+0.64	+0.087	+0.121	204	231	157	123	1.247
Date: 5/3								
1530-36	-0.10	-0.002	-0.031	699	235	573	370	0.029
1536-42	-0.07	-0.001	-0.021	747	225	528	388	0.022
1542-48	-0.12	-0.002	-0.037	801	230	614	399	2.7×10^{-3}
1548-54	-0.06	-0.001	-0.018	782	224	503	351	2.9×10^{-3}
1554-00	-0.08	-0.001	-0.024	810	225	573	355	2.0×10^{-3}
1600-06	-0.10	-0.002	-0.031	726	238	616	367	2.1×10^{-3}
1606-12	-0.05	-0.001	-0.015	705	236	584	355	2.4×10^{-3}
1612-18	-0.09	-0.002	-0.012	702	236	582	406	1.7×10^{-3}
1618-24	-0.01	-2×10^{-4}	-0.004	708	232	558	347	2.1×10^{-3}
1624-30	-0.01	-1×10^{-4}	-0.004	847	234	685	380	1.2×10^{-3}
1630-36	$+7\times10^{-3}$	$+1\times10^{-4}$	+0.002	725	234	587	371	9.7×10^{-4}
1636-42	$+7\times10^{-3}$	$+1\times10^{-4}$	+0.002	776	234	628	354	7.3×10^{-4}
1642-48	+0.03	$+5\times10^{-4}$	+0.009	725	227	530	368	4.7×10^{-4}

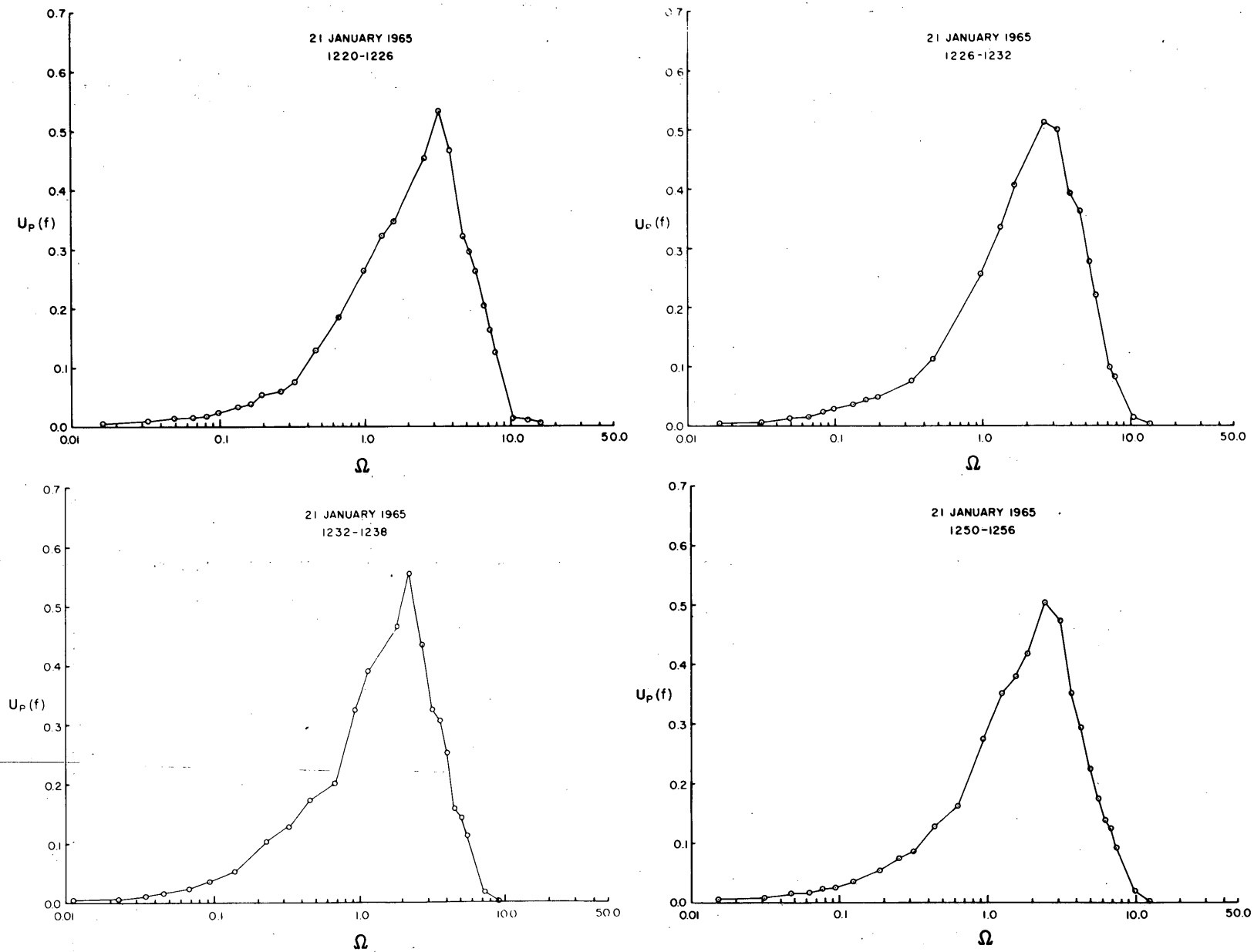

Figure 6. Measured frequency spectra of laser scintillation.

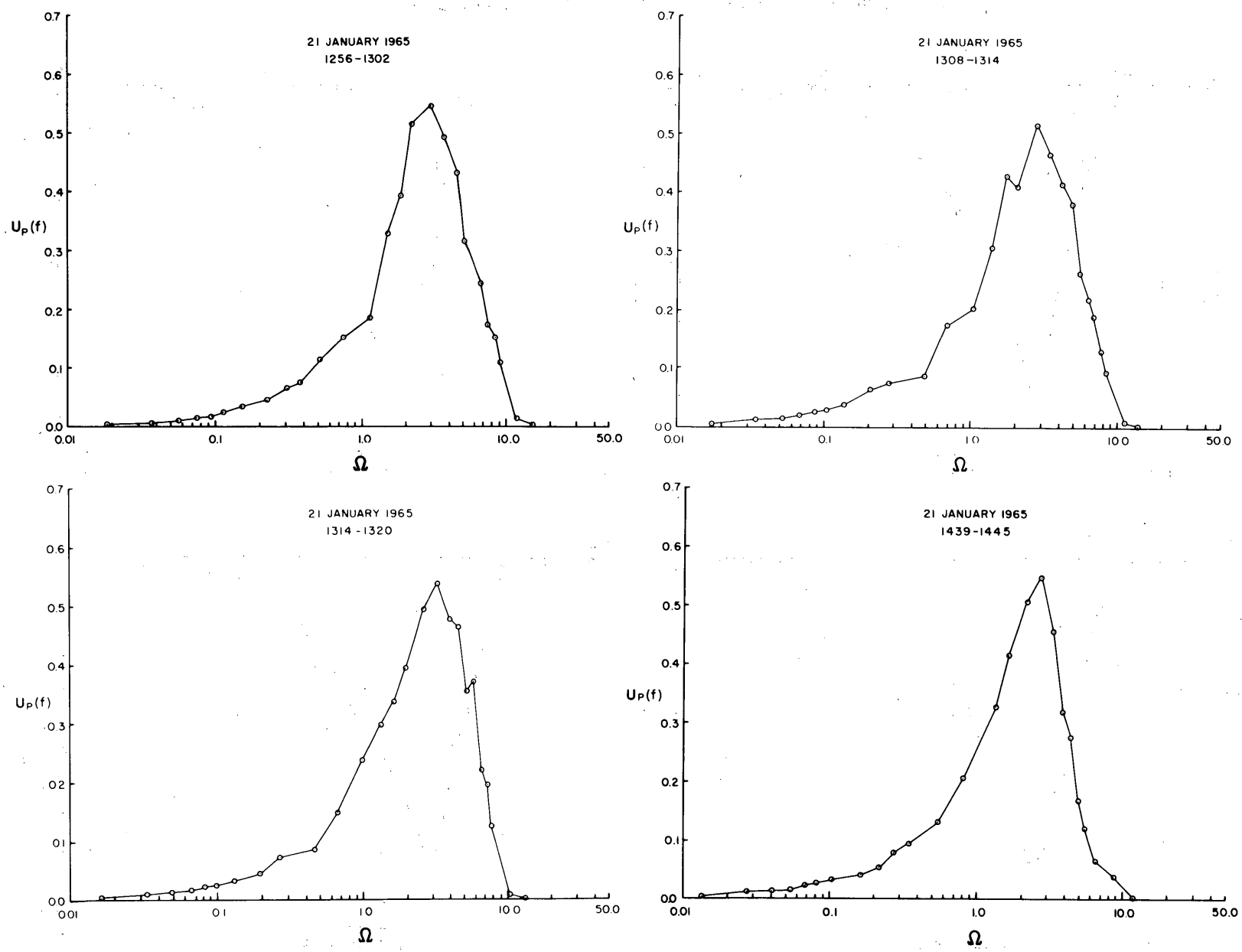

Figure 6. Measured frequency spectra of laser scintillation.

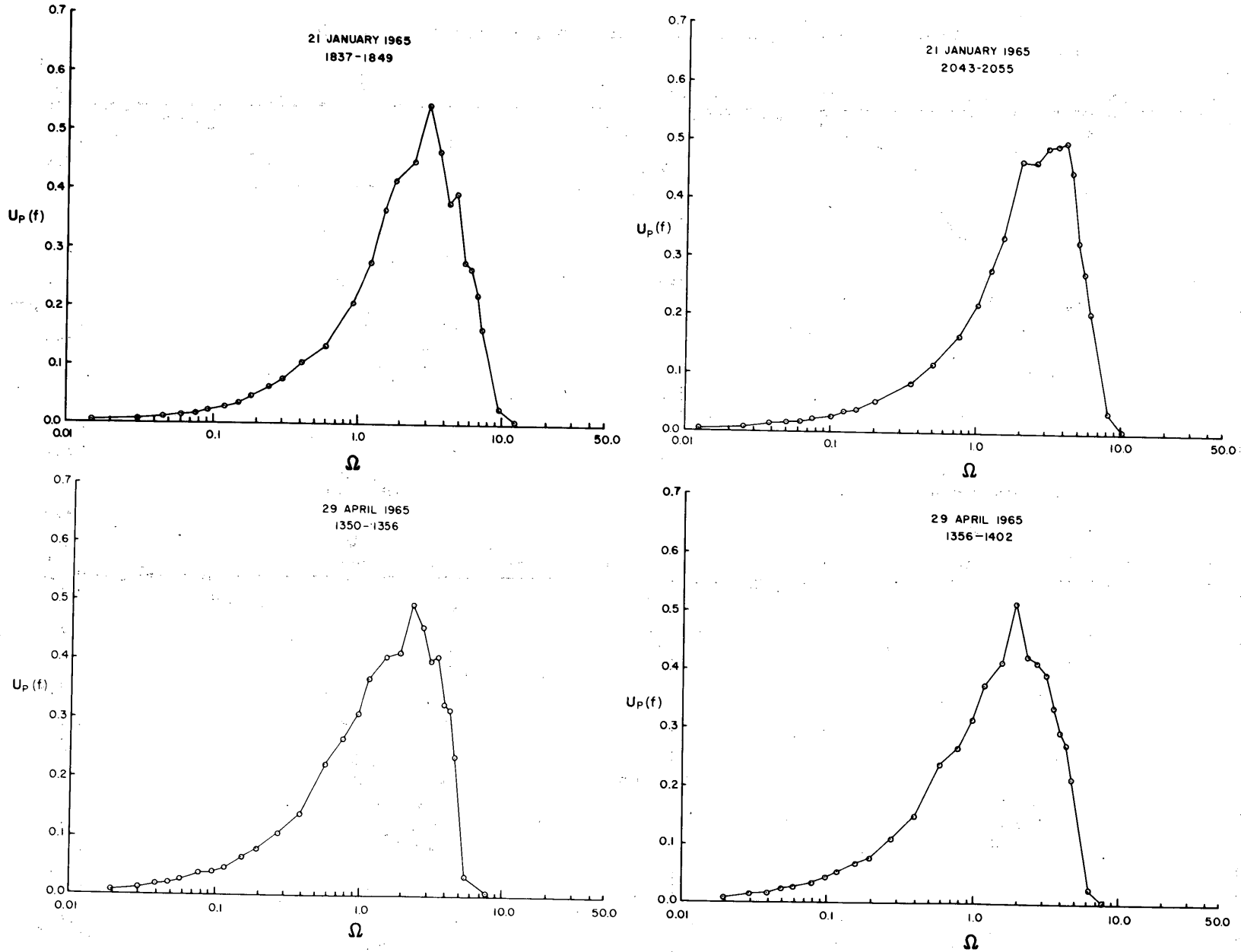

Figure 6. Measured frequency spectra of laser scintillation.

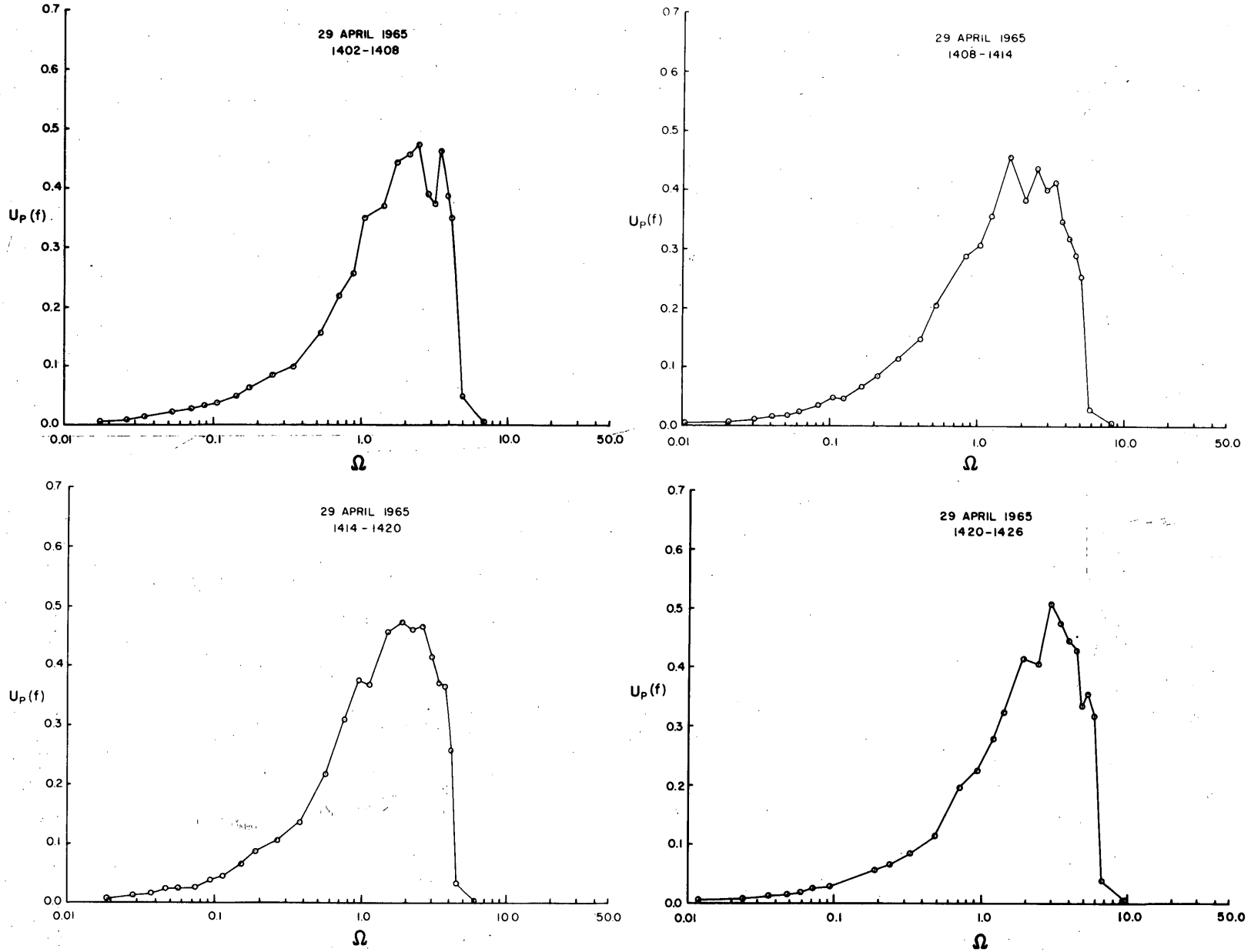

Figure 6. Measured frequency spectra of laser scintillation.

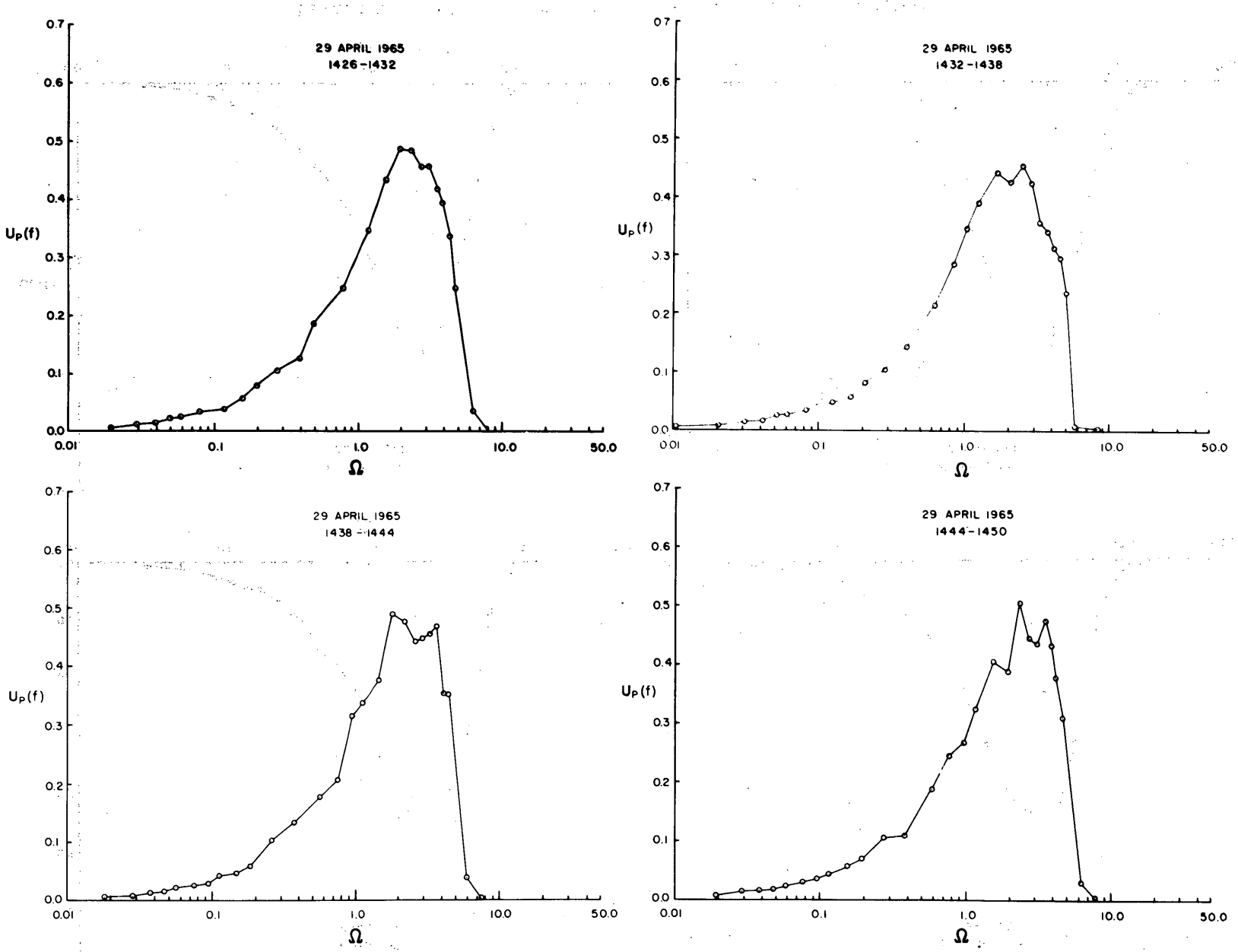

Figure 6. Measured frequency spectra of laser scintillation.

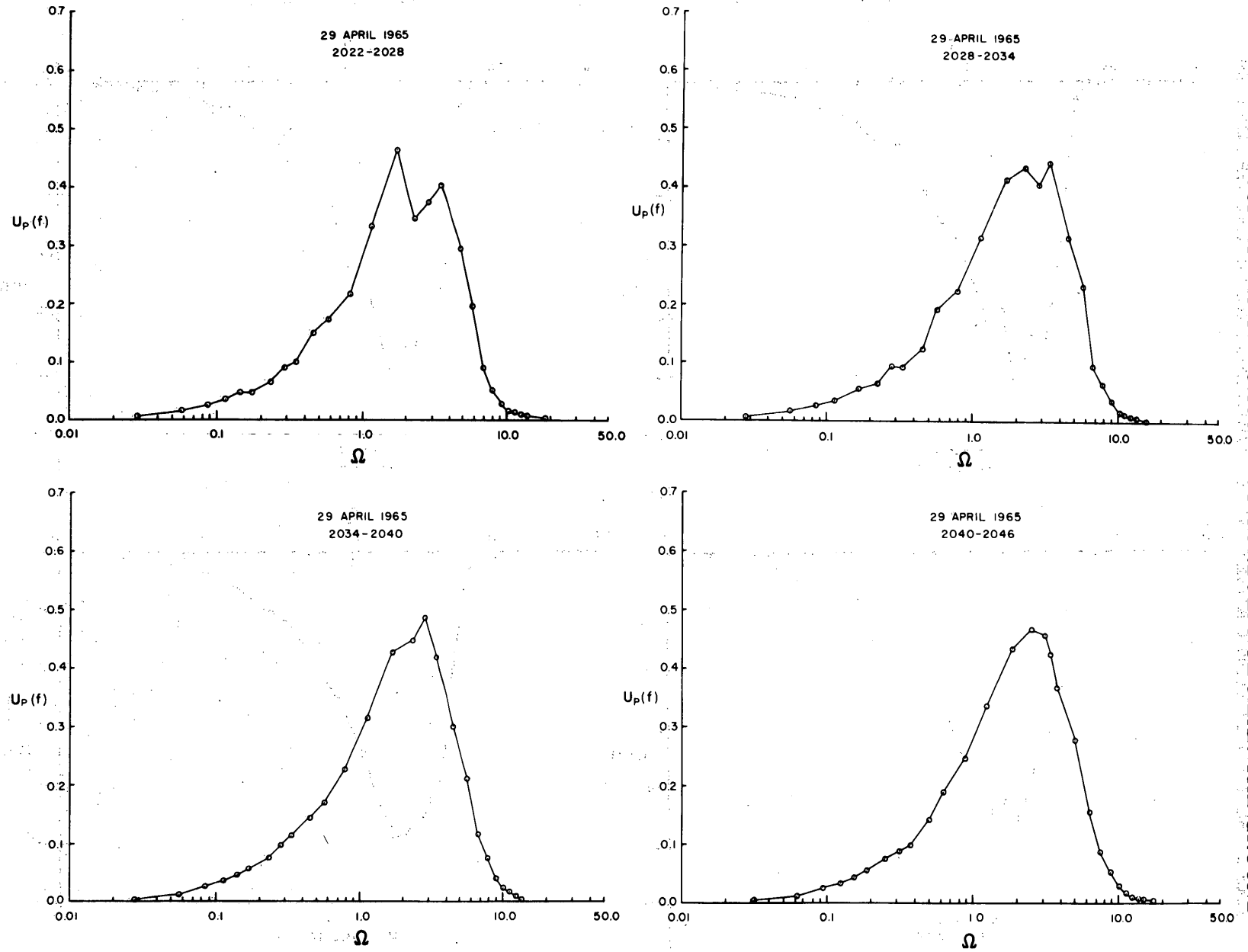

Figure 6. Measured frequency spectra of laser scintillation.

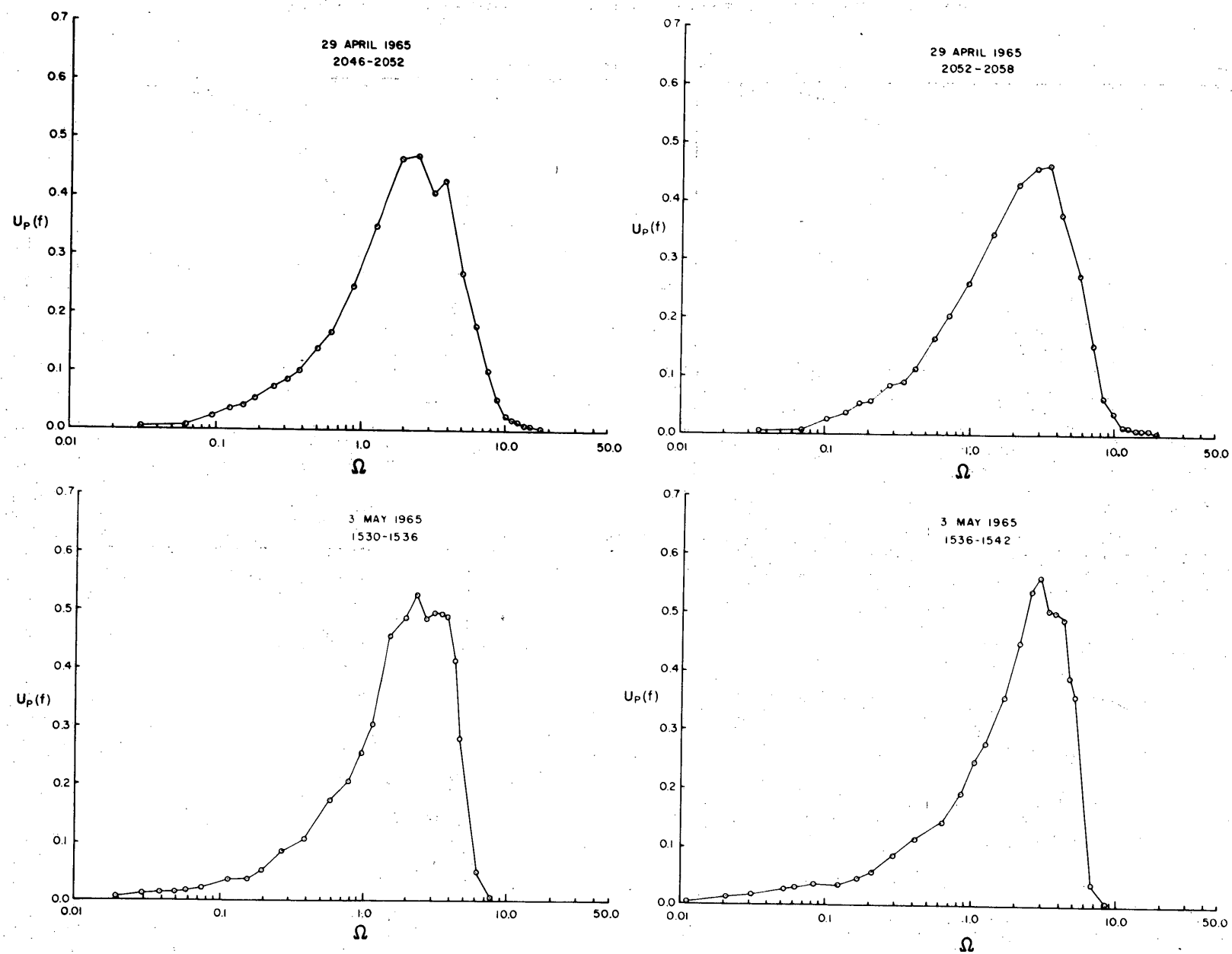

Figure 6. Measured frequency spectra of laser scintillation.

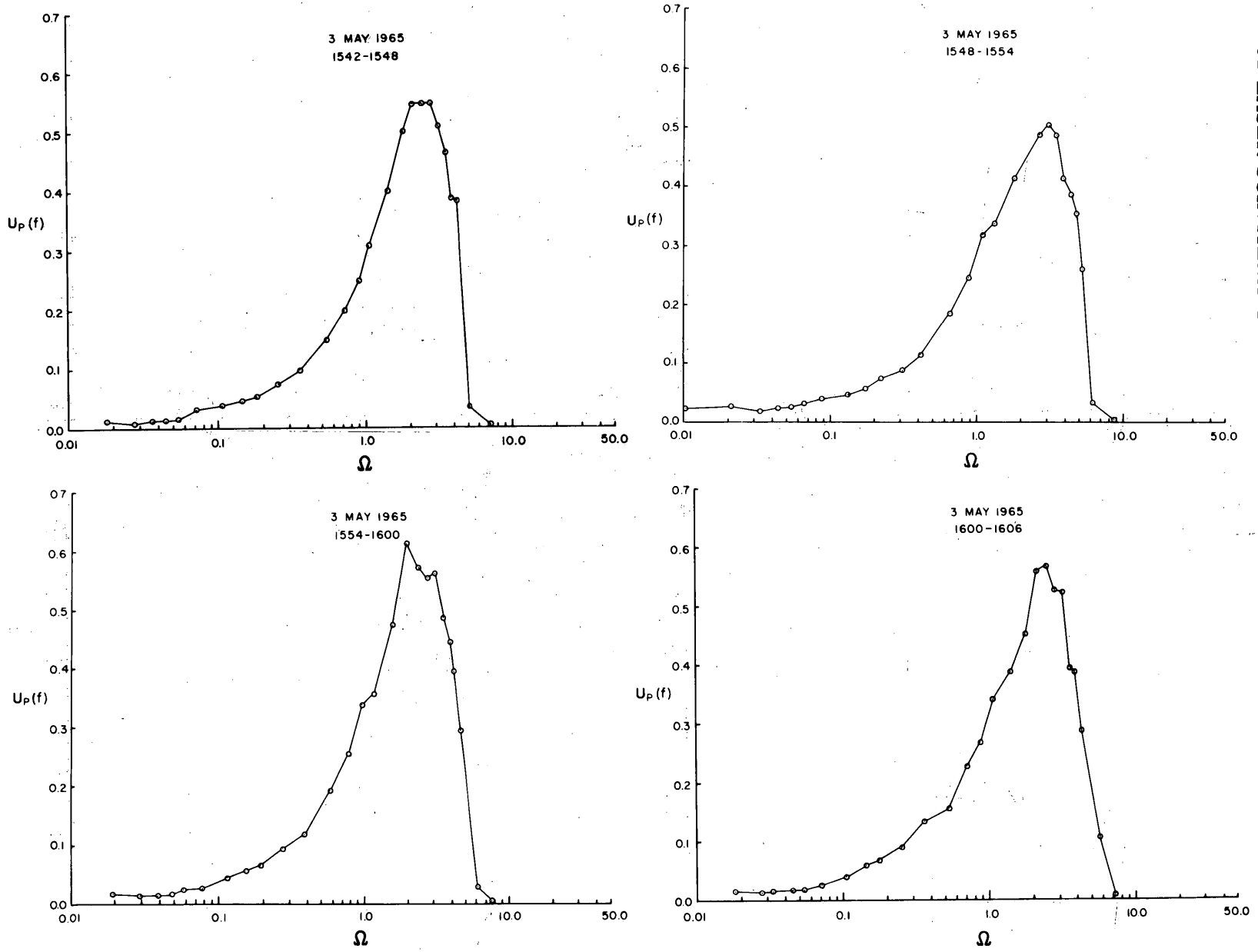

Figure 6. Measured frequency spectra of laser scintillation.

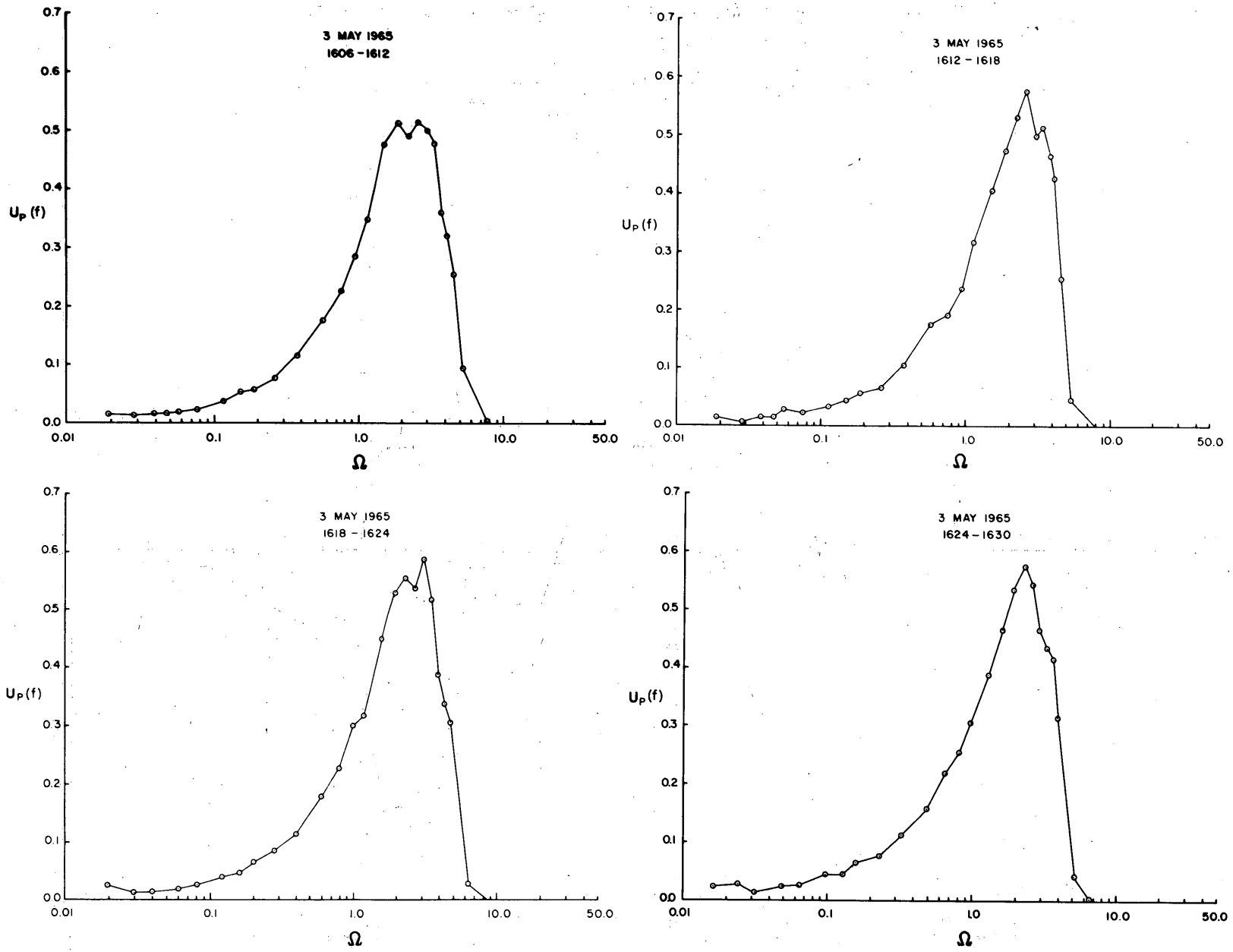

Figure 6. Measured frequency spectra of laser scintillation.

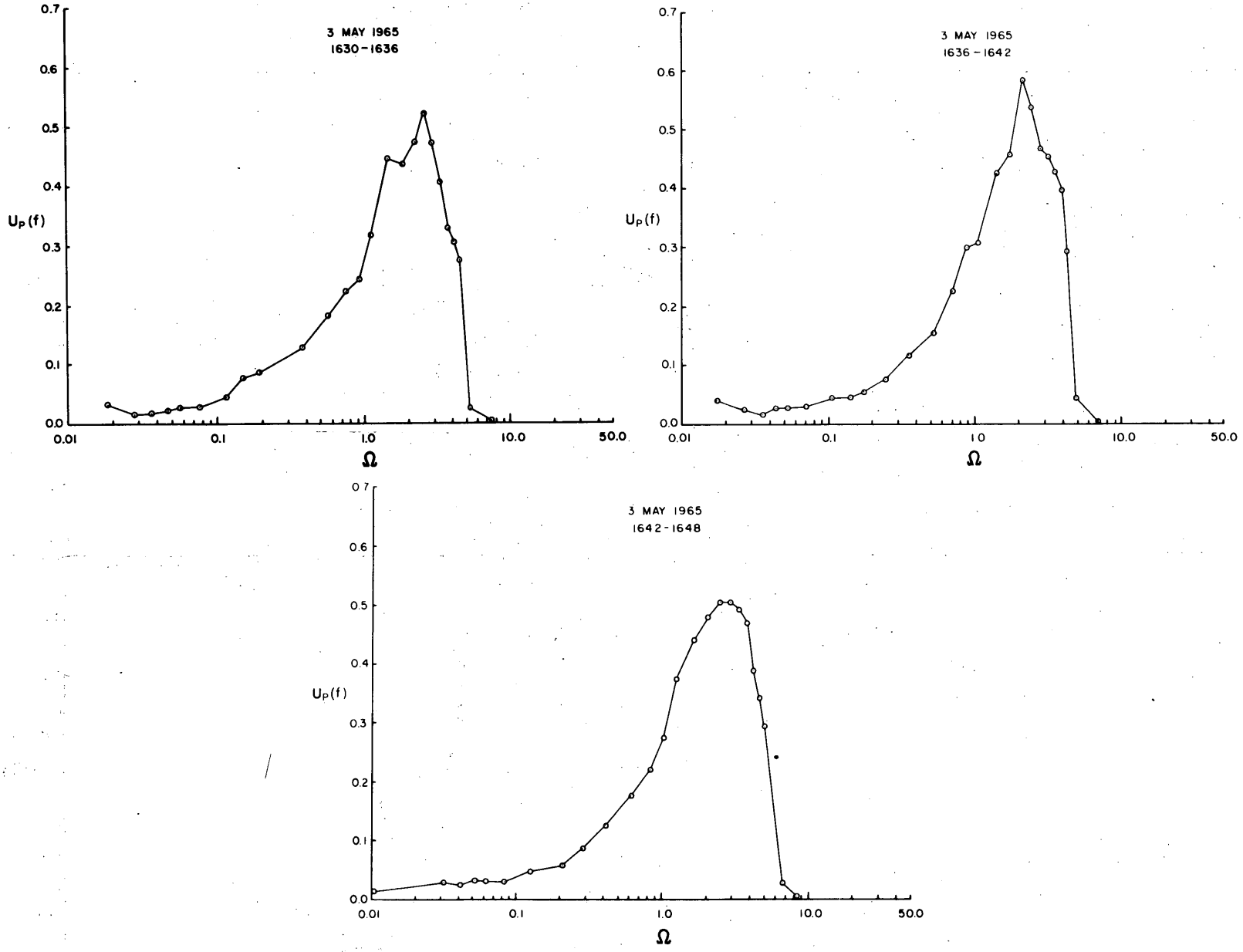

Figure 6. Measured frequency spectra of laser scintillation.

4. ANALYSIS AND DISCUSSION OF EXPERIMENTAL RESULTS*

Experimental conditions significant to the theory

To discuss the experimental results in relation to Tatarski's theory one should examine actual experimental conditions in relation to those required by the model. Among the conditions to be considered are that (1) $\ell_0 << \sqrt{\lambda L} << L_0$, (2) the wind angle relative to the optical path be small compared to $\sqrt{\lambda / L}$, (3) the laser beam be parallel and (4) the turbulence be stationary, homogeneous and isotropic. The extent to which the basic conditions of the theory are satisfied by the experiments and the possible influence when they are not met are discussed in the following paragraphs.

Inequalities involving characteristic lengths. The condition expressed by inequality 2.1 is approximately satisfied for the experiments. The laser wavelength of 0.6328 microns and the optical path length of 500 m give $\sqrt{\lambda L} = 1.78$ cm. For the optical path height of 1 m the inner scale may be taken to be on the order of 0.1 cm and the outer scale to be 100 cm. Wind directions for all experimental data reported formed angles greater than 20 degrees relative to the optical path, completely satisfying the condition that the angle be much greater than $\sqrt{\lambda / L}$.

Laser beam characteristics. The laser was operated in the "plane-parallel" mode and emitted a plane-polarized, coherent light. The beam diameter at its source was about 3.5 mm and was observed to diverge to a diameter of about 20 cm at a distance of 500 m in the absence of atmospheric refractive and diffractive effects. Except for the beam divergence, the laser energy characteristics meet satisfactorily the conditions of Tatarski's model reviewed in Section 2.

The influence of beam divergence on scintillation measurements, as compared to theoretical results for a parallel ray beam, apparently is to cause an increase in non-dimensional frequency (f/f_0) of observed fluctuations. It may be thought of as a magnification produced by the projection of the motion of diffracting turbulent elements on the plane of the receiving aperture of the photometer. If the significant turbulent elements along the optical path are equal in their influence on the scintillation frequency observed and if the horizontal section of the beam is an isosceles triangle with apex at the beam source, the average magnification would be a factor of two. Apparently, furthermore, the angle of divergence is not significant; any divergence would produce a frequency approximately twice as great as that produced by a parallel ray beam. The experimental results discussed below seem to confirm the divergent beam effect and, in fact, good agreement of observed with predicted spectra is obtained if the non-dimensional frequencies of the Tatarski spectrum are increased by a factor of 2.

Turbulence characteristics. The Tatarski scintillation spectrum was derived for homogeneous, isotropic and stationary turbulence. The conditions of stationarity and horizontal homogeneity for the experimental periods were probably as nearly ideal as could be expected in natural conditions. As mentioned in Section 3, both the location of the measurements and the selection of wind

*by Donald J. Portman

and weather conditions helped assure realization of these requirements. For turbulence scales of interest the existence of both isotropy and vertical homogeneity, however, may be questioned at the height of 1 m above ground. Because the optical path is horizontal, it is unlikely that the vertical variation of turbulence characteristics could have a direct and important influence. Isotropy, however, is a significant condition invoked at several points in the development of the theory and it would appear that its absence could have an important influence on observed scintillation spectra.

In the final expression of Tatarski's model given by eq 2.31 and 2.32 the isotropic assumption is extended to include a specific form for the three-dimensional spectral density for the refractive index field

$$\phi_n(\kappa) = 0.033 C_n^2 \kappa^{-11/3}. \qquad (2.15)$$

As noted in Section 2, eq 2.15 is derived from a similar expression for the three-dimensional velocity field which described the Kolmogorov inertial subrange. The latter is expected to exist when the turbulence-creating mechanisms have scales significantly larger than the scales that characterize the smallest turbulent motions in the spectral range at which viscous dissipation takes place. It is often assumed that turbulence-generating mechanisms near the ground (horizontal wind shear and buoyancy forces) give rise to anisotropic turbulent motions whose sizes are on the order of the height above ground. The scale of viscous dissipation is usually considered to be on the order of 0.1 cm so that, for turbulence at a height of 1 m, the question is whether or not three orders of magnitude represent a sufficient range for the existence of an inertial subrange. Equally important, of course, is the extent of the subrange in relation to the function $f(\kappa)$ shown in Figure 2.

The turbulence spectra shown in Figure 5 represent four periods of relatively weak unstable stratification and one period of weak stable stratification. None shows evidence of isotropy because, according to von Karman and Howarth (1938), in stationary isotropic turbulence, the spectral densities of longitudinal component (u') must be numerically less than either of the spectral densities of the transverse components (v' and w'). The latter spectral densities should be identical. It is noted, however, that all spectra seem to approach a -5/3 slope at high wave numbers. It may be concluded that isotropic turbulence did not exist for significant wave number ranges for these periods in spite of the fact that a $\kappa^{-5/3}$ dependency is seen at higher wave numbers. Because of the apparent lack of isotropy, the index of refraction spectra for these periods should not be expected to follow, necessarily, the -5/3 relationship and the scintillation spectrum obtained in such conditions can be expected to deviate from that given by eq 2.31.

Bolgiano (1959) and Monin (1962) have discussed the nature of temperature spectra in thermally stratified shear flow. Bolgiano analyzed the case of a stably stratified layer and identified a "buoyant subrange" adjacent to the low wave number limit of the inertial subrange. Dimensional analysis yielded a temperature fluctuation spectrum proportional to the -7/5 power of the wave number. The results of Monin's analysis were in agreement with those of Bolgiano for stable stratification. For unstable stratification Monin found that, for wave numbers less than those of the inertial subrange, the temperature spectrum should decrease with increasing wave number at a rate

greater than $\kappa^{-5/3}$. For both stable and unstable stratification, Monin's spectra merge with the -5/3 law at large wave numbers.

It is reasonable to expect that index of refraction spectra in anisotropic turbulence would be similar to temperature spectra and that the Bolgiano and Monin analyses might be used to describe them. If this is so, and if eq 2.31 may be used to suggest the form of scintillation spectra in anisotropic turbulence, relatively large scintillation spectral densities would appear at low non-dimensional frequencies in unstable stratification while the reverse would be found for stable stratification. The fact that eq 2.31 was derived strictly for the condition of isotropy, however, should not be ignored.

Variation of scintillation intensity with refractive index structure function coefficient

Experimental values of σ_P^2 obtained from the frequency spectra were compared with values of σ^2 computed by means of Tatarski's theoretical relationship

$$\sigma = 1.23\, C_n^2\, k^{7/6} L^{11/6} \tag{2.24}$$

with

$$C_n^2 = \left(\frac{-79 \times 10^{-6} p}{T^2}\right)^2 C_T^2 \tag{4.1}$$

as discussed in Section 2. The following numerical values were used:

$k^{7/6}$	6.757×10^5	rad cm^{-1}
$L^{11/6}$	4.119×10^8	cm
p	1.000×10^3	millibars
T	2.64×10^2	Deg Absolute, 21 January
	2.94×10^2	Deg Absolute, 29 April, 1350-1450
	2.84×10^2	Deg Absolute, 29 April, 2022-2058
	3.04×10^2	Deg Absolute, 3 May

The results are plotted in Figure 7 in logarithmic coordinates. The cluster of points for values greater than 1 on both scales represents data obtained on 29 April. Those in midrange represent 21 January, and those at extremely small values represent 3 May. Although scintillation was more intense on 29 April than for the other observation periods, it was moderate compared to that observed for several periods discussed in USA CRREL Research Report 111, Part I and Part II. The least scintillation possible, however, was represented by some of the data for 3 May when the temperature profile became nearly adiabatic.

As shown in Figure 7, all but four values of measured variance were less than those computed, in general agreement with the fact that the latter represents the variance to be obtained with an infinitesimally small aperture. The relatively large scatter of points for small variances may be due to inaccuracies in temperature profile measurement as well as in spectrum analyses. For the smallest variances the signal-to-noise ratios in the spectrum analyses were too small for reliable interpretation.

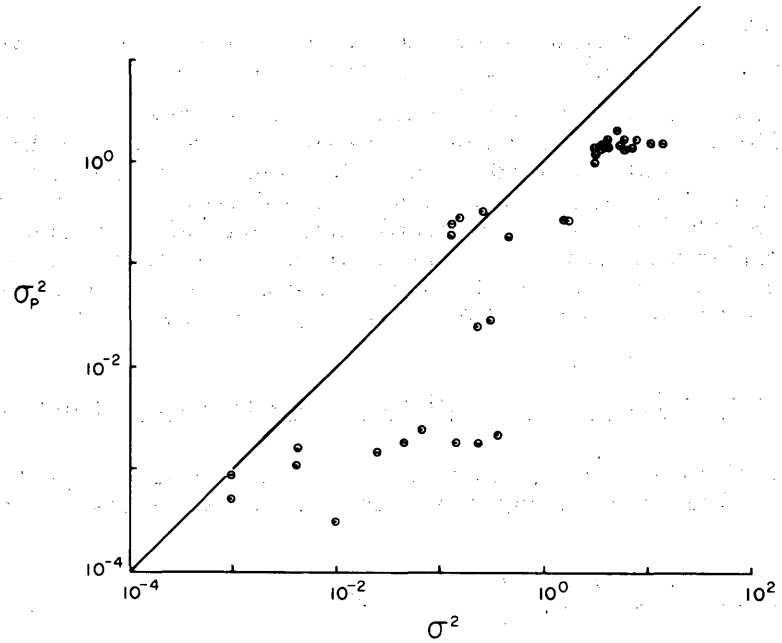

Figure 7. Comparison of measured (σ_P^2) and calculated (σ^2) scintillation spectral variances. The line has a slope of unity.

Tatarski (1961, p. 236-237) shows that for a given aperture the ratio $\ln(1 + \sigma_P^2)/\sigma^2$ increases as σ^2 increases. Although the data shown in Figure 7 may be interpreted as showing this effect, the uncertainty in the values of the smaller variances and the limited range of the data make such a statement unwarranted.

Variation of frequency of maximum power with wind speed

To describe measured scintillation spectra Tatarski defined the frequency f_m as the average of two frequencies for which $fW_P(f)$ is one-half the maximum measured value. Values of f_m were computed for all spectra obtained in the present experiments and were used as a basis for studying the effect of the wind speed component normal to the optical path.

A similar frequency, F_m, was computed for the theoretical spectrum given by eq 2.32 for $\rho = 0.493$ and found to be

$$F_m = 2.65\, f_0 = 1.06\, \frac{\overline{V}_n}{(\lambda L)^{\frac{1}{2}}}. \qquad (4.2)$$

A relationship of measured values of f_m to $\overline{V}_n$ is shown in Figure 8 for the 39 spectra listed in Table III. Values of f_m increased linearly from about 120 cps to 400 cps as $\overline{V}_n$ increased from about 1.6 to 7 m sec^{-1}. A least squares analysis gave

$$f_m = 45.9 + 0.551\, \overline{V}_n. \qquad (4.3)$$

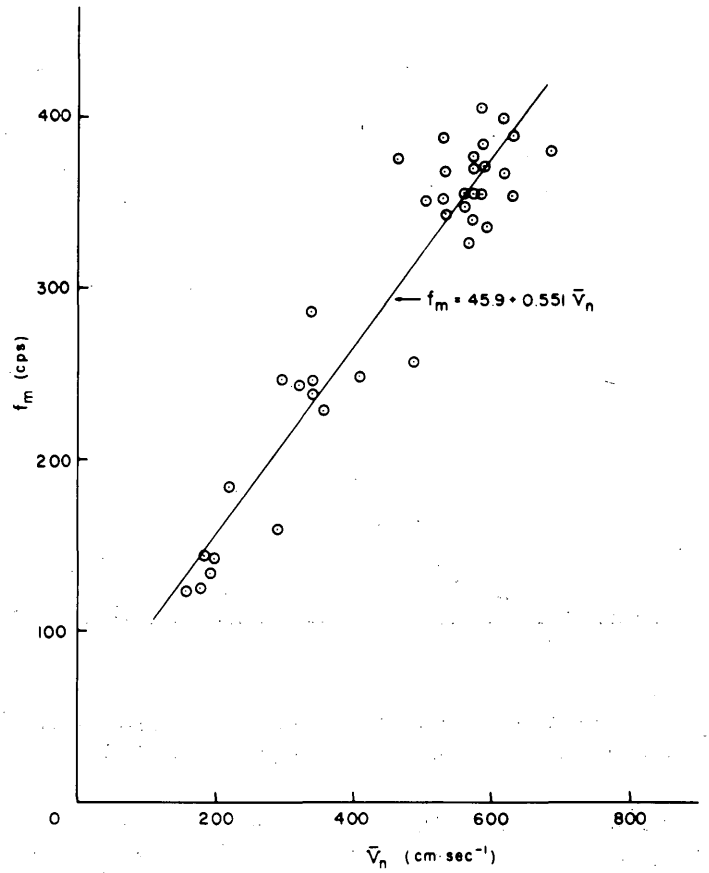

Figure 8. Frequency of maximum power (f_m) versus wind speed component normal to the optical path ($\overline{V}_n$).

The fact that the relationship does not give a zero frequency for zero normal wind speed is an unacceptable result. Although it may be argued that scintillation can occur in the presence of motion due to buoyancy effects alone, a f_m value as high as nearly 46 cps in such a condition would seem unlikely. It is more reasonable to account for the above result, as well as the scatter of points around the regression line, by variations in wind conditions along the optical path.

The above result was compared with the theoretical result given by eq 4.2. In the present experiments $(\lambda L)^{\frac{1}{2}}$ was 1.78 which, by substitution into eq 4.3, gives

$$f_m = 45.9 + 0.98\,\frac{\overline{V}_n}{(\lambda L)^{\frac{1}{2}}}. \qquad (4.4)$$

There is close agreement between the factors 1.06 and 0.98 of eq 4.2 and 4.4. These, however, are about four times greater than similar data obtained from experiments reported in USA CRREL Research Report 111, Part II and described by Ryznar (1965). The latter results were obtained

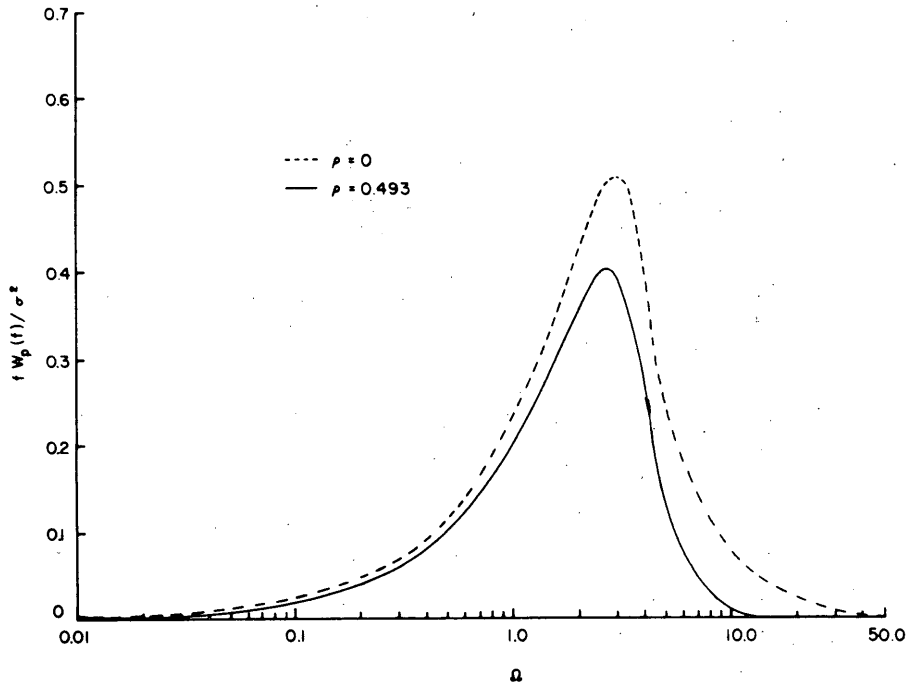

Figure 9. Tatarski's normalized spectra of scintillation obtained by numerical integrations of eq 2.32.

with an incandescent source and with a photometer having an aperture diameter of 5 cm. The parameter ρ was about 4 for the latter experiments, and $(\lambda L)^{\frac{1}{2}}$ was slightly greater. It is clear from eq 2.32 that Ω_{max} for $\rho \cong 4$ is significantly less than Ω_{max} for smaller values of ρ. A resulting smaller increase of f_m with $\overline{V}_n$ is supported by the experimental results discussed above.

Spectral shape characteristics

To compare measured scintillation spectra with Tatarski's theory eq 2.32 was integrated numerically with the aid of a digital computer. Eq 2.32 takes into account the effect of the aperture of the photometer receiver in terms of the dimensionless parameter $\rho = R(2\pi/\lambda L)^{\frac{1}{2}}$ in which R is the radius of the aperture. For the present experiments $\rho = 0.493$. The results for $\rho = 0.493$ and also for $\rho = 0$ are shown in Figure 9. The spectral densities have been plotted at non-dimensional frequencies twice those given by eq 2.32 to account for the divergence of the laser beam as explained above.

The theoretical spectrum taking the size of the aperture into account has (a) a significantly smaller total variance and (b) a lower frequency of maximum spectral density than does the spectrum for $\rho = 0$ as noted in the first section. It is to be noted, also, that because the spectral densities computed with eq 2.32 are normalized by the total variance that would be observed with a zero radius aperture, measured spectra cannot be compared directly to it. If the measured spectra conform to the Tatarski model, however, they should fall between the two spectra displayed here.

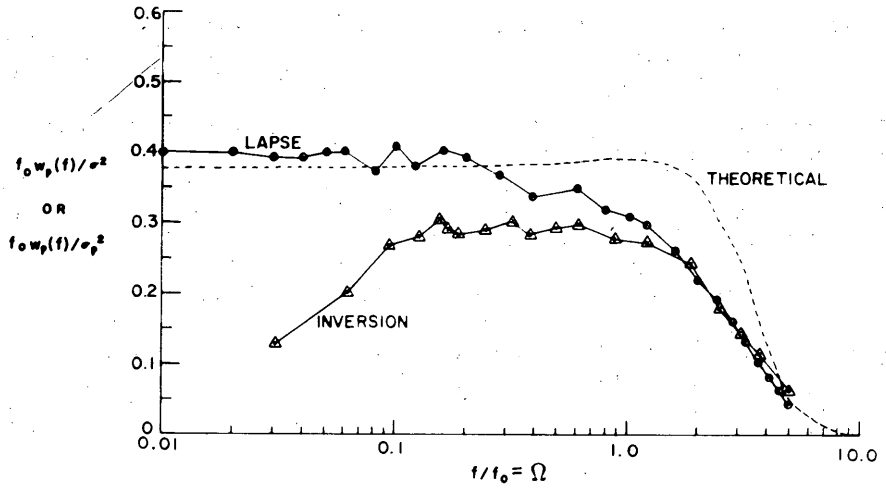

Figure 10. Average scintillation spectra for lapse and inversion conditions.

Inspection of the measured spectra in Figure 5 shows their shapes to be generally similar to the theoretical model. In many of the spectra, however, the spectral densities for $0.1 < \Omega < 1.5$ had higher values than the corresponding theoretical values. For some it may be possible to account for the effect on the basis of unstable thermal stratification in accordance with the reasoning given above. This form of spectral display, however, minimizes spectral differences at low non-dimensional frequencies and, in addition, tends to emphasize shifts in non-dimensional frequency that may be due to experimental error in the measurement of horizontal wind velocity.

To examine the possible influence of anisotropy more carefully, scintillation spectra measured on 29 April were averaged for the periods 1350 to 1426 and 2022 to 2058 and are shown in Figure 10 along with a graph of eq 2.32. In this figure the ordinate is scaled in units of $f_0 W_P(f)/\sigma_P^2$ for the observations and in units of $f_0 W_P(f)/\sigma^2$ for eq 2.32. The observation period of 1350 to 1426 was characterized by unstable thermal stratification with Richardson numbers not greatly different from those measured during the periods 1250 to 1320 on 21 January and 1432 to 1444 on 29 April for which turbulence spectra are shown in Figure 5. Both the mean vertical temperature differences ($T_{1.4} - T_{0.7}$) and the values of σ_P^2 were significantly larger for the 1350 to 1426 observation period than for the periods of turbulence measurement. It is likely, therefore, that the "lapse" spectrum in Figure 10 represents a period of greater deviation from the -5/3 law than indicated by the daytime (lapse) turbulence spectra of Figure 5. The influence of anisotropy in this case seems to be a weak enhancement of low frequency spectral densities and a suppression of spectral densities at non-dimensional frequencies between 0.3 and 5. It will be recalled that an increase at low frequencies was suggested above on the basis of the temperature spectrum model of Monin.

The inversion spectrum, on the other hand, shows a marked suppression of spectral densities for low values of non-dimensional frequency as expected. The turbulence spectra in Figure 5 for 2022-2034, 29 April, were measured during this period and would appear to represent well the conditions for the entire period 2022 to 2058 on the basis of data given in Table III. In addition

to the suppressed spectral densities at low frequencies, the inversion spectrum shows spectral densities less than those of the lapse spectrum at all non-dimensional frequencies less than the value of 1.7.

On the basis of the limited number of observations and the nature of the Tatarski theoretical spectrum it may be concluded that buoyancy and shear effects in turbulence near the ground cause index of refraction spectral densities to be such that low frequency scintillation is suppressed in stable thermal stratification and enhanced in unstable thermal stratification. It is to be expected that the effect increases with increasing intensity of scintillation at all frequencies because the total intensity increases with absolute magnitude of the vertical temperature gradient in accordance with eq 2.41. In this sense, then, Tatarski's spectrum may be regarded as a limiting condition which could be observed only when buoyancy effects are absent and they can be absent, entirely, only when the vertical temperature gradient and, therefore, scintillation vanish.

5. VARIATION OF OPTICAL SCINTILLATION WITH HEIGHT*

Prior to the availability of a laser and hot wire anemometers, field experiments were conducted with an incandescent light source to determine the variation of scintillation intensity and frequency with height near the ground. The observed variation was studied in relation to turbulence parameters discussed in Section 4. The field experiments and an analysis of the results obtained from them are discussed below.

Field experiments

Equipment and procedures. Measurements of the variation of optical scintillation with height were made with identical light sources located at heights of 0.5, 1.0, 2.0, and 4.0 m above ground at a distance of 500 m from a photometer. The light sources used in this experiment were the incandescent type shown in USA CRREL Research Report 111, Part II. Each consisted of a pre-focused projector lamp powered by a 12-v battery. Within the unit, light from the lamp passed through two condensing lenses, a 0.5-cm aperture and finally through a projector lens having a diameter of 5 cm. The light diverged to a diameter of about 8 m at the 500-m distance of a photometer. Light from the source was polychromatic, but a spectral filter within the photometer had a peak transmittance for $\lambda = 0.8 \times 10^{-4}$ cm. For a 500-m path length, $(\lambda L)^{\frac{1}{2}}$ was 2.0 cm. The photometer aperture had a diameter of 5 cm.

The measurement sequence consisted of (1) remotely activating the light at 0.5 m, (2) aligning the photometer at the same height with it, and (3) recording 2 to 3 minutes of scintillation intensity and frequency data. The light at 0.5 m was then turned off, that at 1.0 m was turned on, the photometer was placed at 1.0 m and aligned with the light, and similar recordings were made. The procedure was repeated at heights of 2.0 and 4.0 m and started anew at 0.5 m. A sweep upward through the four heights was completed in approximately 15 minutes when both intensity and frequency recordings of scintillation were made and in about 7 minutes when only intensity recordings were made.

*by Edward Ryznar

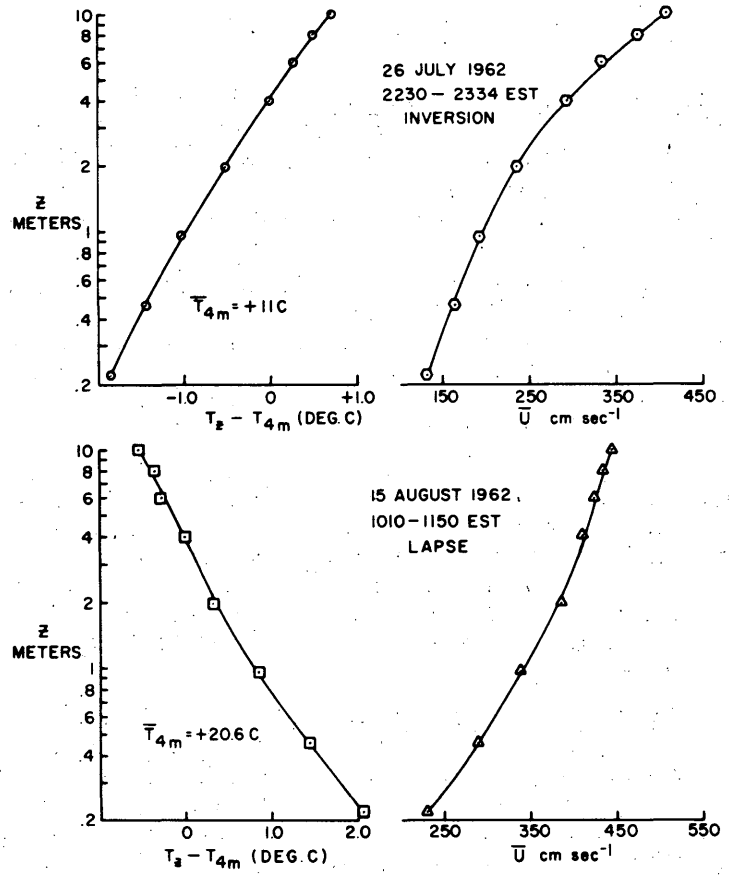

Figure 11. Average wind and temperature profiles.

Scintillation intensity was measured in terms of percent modulation (Pm), a measure of the relative intensity of brightness fluctuations detected by the photometer. It is defined in detail in USA CRREL Research Report 111, Parts I and II.

Observation periods. Measurements were made during a nighttime inversion on 26 July 1962, from 2230 to 2334 EST, and during a daytime lapse on 15 August 1962, from 1010 to 1150 EST. For each period the sky was clear and wind and temperature conditions were unusually steady, so that little change in average scintillation characteristics occurred during either period.

Results

Wind and temperature profiles. The average wind and temperature profiles for both periods are shown in Figure 11 in semi-logarithmic coordinates. For the inversion, the average temperature difference between 0.5 and 4.0 m was +1.4 C and the average wind speed at 1 m was about 2 m sec^{-1}. For the lapse condition, the average temperature difference between the same two heights was -1.4 C and the wind speed was about 3.4 m sec^{-1}. It can be noted that curvature of each wind profile is consistent with that expected from the effects of buoyancy in stable and unstable flow (Sutton, 1953). Roughness parameters for the grass-covered field were computed

for adiabatic conditions and were 1.16 cm on 26 July and 1.37 cm on 15 August.

Height variation of frequency of maximum power. Two frequency spectra were obtained for each of the four measurement heights for both the lapse and the inversion. The parameter f_m, a measure of the frequency of maximum power, was computed for each spectrum according to the method described in Section 4 and was averaged for the two spectra at each height.

Profiles of (1) f_m, (2) average horizontal wind speed $\overline{U}$, corresponding to the periods of frequency recordings, and (3) the ratio $f_m/\overline{V}_n$ are shown in Figure 12 in semi-logarithmic coordinates. The temperature difference between 0.5 m and 4 m is also noted. It is evident that f_m increased with height in both conditions. Average values increased from about 20 cps at 0.5 m to about 49 cps at 4.0 m in the inversion condition and from about 24 cps at 0.5 m to 49 cps at 2.0 m in the lapse condition.

It can be noted that curvatures in the average profiles of f_m are similar to those of the wind profiles in both stability conditions. Values of $\overline{V}_n$ increased from about 1.4 m sec^{-1} to 2.9 m sec^{-1} and from 2.3 m sec^{-1} to 3.5 m sec^{-1} between 0.5 m and 4.0 m in the inversion and lapse conditions, respectively. The effect of an increase of $\overline{V}_n$ with height, however, was to increase f_m in such a way that $f_m/\overline{V}_n$ remained approximately constant. Average values were about 0.14 cm^{-1} and 0.13 cm^{-1} for the inversion and lapse conditions respectively.

Height variation of scintillation intensity (Pm). The variation of scintillation intensity with height for the inversion and lapse conditions is shown in logarithmic coordinates in Figure 13. Pm for the lapse was almost twice that for the inversion and decreased with height about 30% more. The points shown are averages of five and six successive measurement sweeps through the four heights for the inversion and lapse, respectively. For the inversion, Pm decreased from 59 at 0.5 m to 29 at 4.0 m, and for the lapse Pm decreased from 95 at 1.0 m to 48 at 4.0 m. A least squares analysis gave

$$Pm \propto z^{-0.35}$$

and

$$Pm \propto z^{-0.49}$$

for the inversion and lapse, respectively. It was not possible to measure Pm at 0.5 m for the lapse because mean refraction caused the apparent position of the light source to be partly obscured by the ground surface when the light was viewed from the distance of the photometer.

Height variation of C_T and Richardson number (Ri). Based on the discussion in Section 4, the observed height variation of Pm may be interpreted as a corresponding height variation of the structure constant for refractive index fluctuations, C_n, which may be expressed in terms of the corresponding structure function coefficient for temperature fluctuations, C_T. The equation for computing C_T from temperature profile data proposed by Tatarski (1961) is

$$C_T = a k_v^{\frac{2}{3}} \frac{\overline{T}_1 - \overline{T}_2}{(z^{\frac{1}{3}})(\ln \frac{z_1}{z_2})} \qquad (5.1)$$

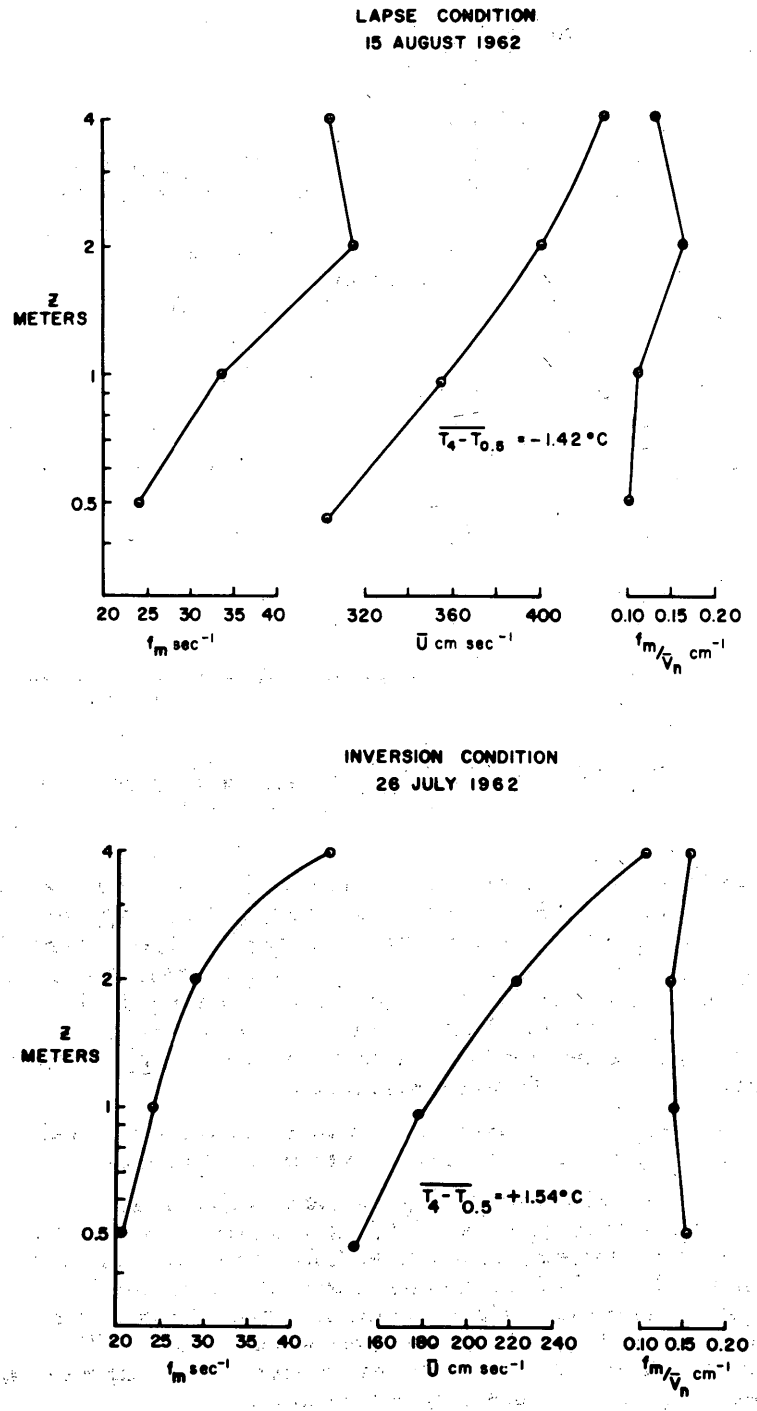

Figure 12. Profiles of scintillation frequency of maximum power (f_m), horizontal wind speed ($\overline{U}$) and the ratio of f_m to the wind speed component normal to the optical path (f_m/V_n) for inversion and lapse conditions.

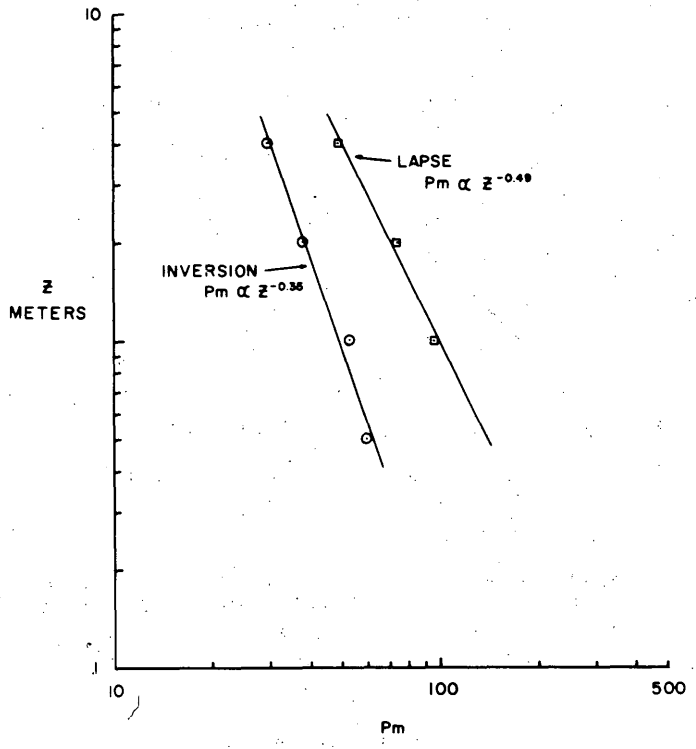

Figure 13. Height variation of scintillation intensity (Pm).

in which k_v is von Karman's constant ($\cong 0.4$), "a" is a coefficient whose value depends on Richardson number, T is temperature and z is height. Tsvang (1960) determined the dependence of the coefficient "a" on Ri. In order to compute C_T, values of Ri were first computed for several heights according to the method proposed by Lettau (1957) for "quasi-local" Ri and values of "a" were then determined from Tsvang's relationship. Because of its dependency on Ri, "a" was found to be proportional to $z^{-0.14}$ for the inversion and to $z^{0.11}$ for the lapse.

Average wind and temperature data for several height increments were obtained from the profiles shown in Figure 11. Each computation of Ri and C_T was valid for the geometric mean height, $z = (z_1 z_2)^{\frac{1}{2}}$, of each height increment (Lettau, 1957). A ratio of $z_2 / z_1 = 2$ was used and height increments ranged from $z_1 = 0.22$ m and $z_2 = 0.44$ m for a geometric mean height of 0.31 m to $z_1 = 3.0$ m and $z_2 = 6.0$ m for a geometric mean height of 4.24 m. The maximum temperature difference in the computations was 0.57 C which was measured between 0.5 and 1.0 m during the lapse and the maximum difference in wind speed was 0.6 m sec^{-1} measured between 3 and 6 m during the inversion.

The height variation of Ri in logarithmic coordinates for the inversion and lapse is shown in Figure 14. Absolute values of Ri increased from about 0.06 at 0.5 m to 0.12 at 4.0 m in the inversion and from 0.03 to 0.56 for the same height interval in the lapse. A least squares analysis gave

$$Ri \propto z^{0.23}$$

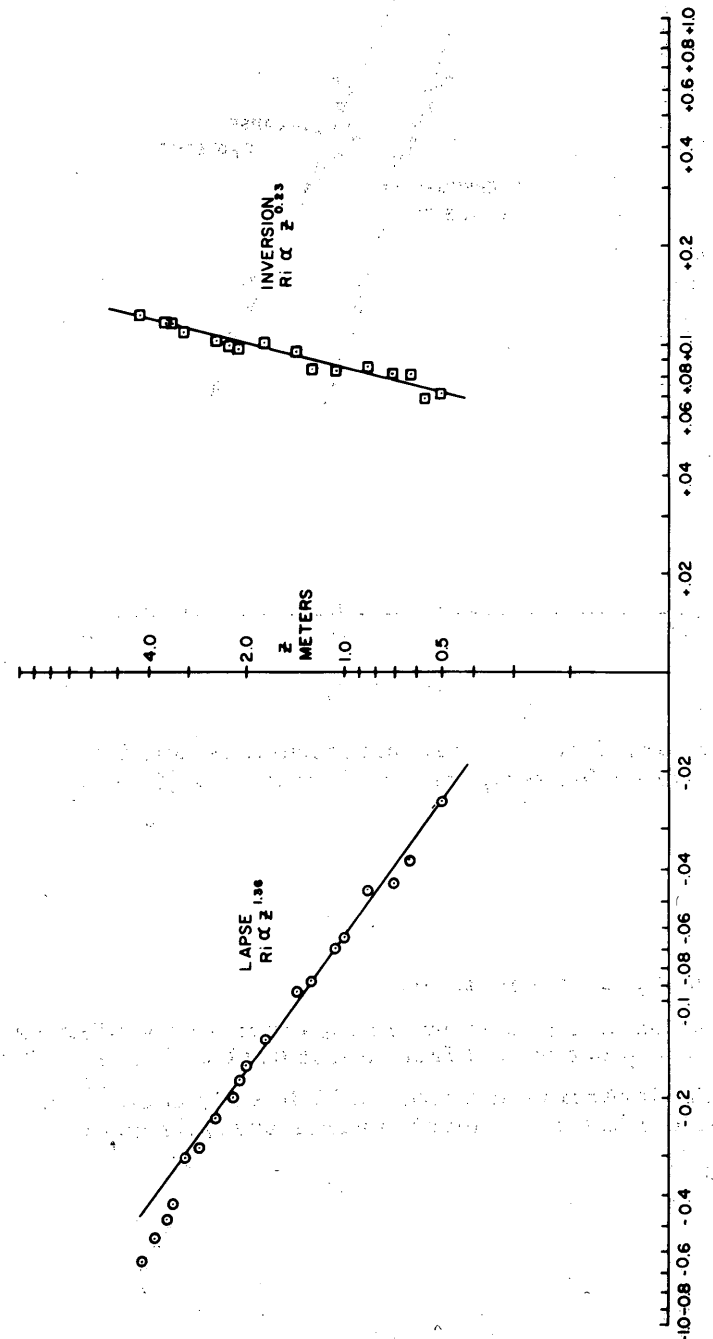

Figure 14. Height variation of Richardson number (Ri).

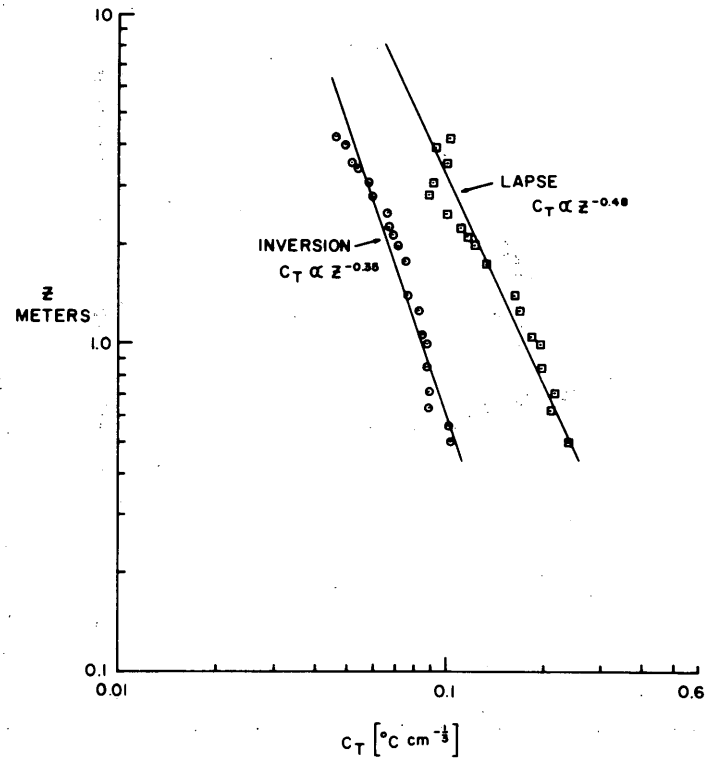

Figure 15. Height variation of structure function coefficient for temperature fluctuations (C_T).

and

$$-Ri \propto z^{1.36}$$

for the inversion and lapse, respectively.

The height variation of C_T is shown in logarithmic coordinates in Figure 15. Values of C_T decreased from about 0.11 at 0.5 m to 0.05 C cm$^{-\frac{1}{3}}$ at 4.0 m for the inversion and from 0.21 to 0.09 C cm$^{-\frac{1}{3}}$ for the same height increment for the lapse. A least squares analysis gave

$$C_T \propto z^{-0.35}$$

and

$$C_T \propto z^{-0.48}$$

for the inversion and lapse, respectively.

Height variation of temperature gradient ($\Delta T/\Delta z$). Temperature gradients were computed by dividing temperature differences by corresponding height increments appropriate for geometric mean heights of 0.5, 1.0, 2.0, and 4.0 m. Height increments ranged from $z_1 = 0.35$ and $z_2 = 0.7$ m for a

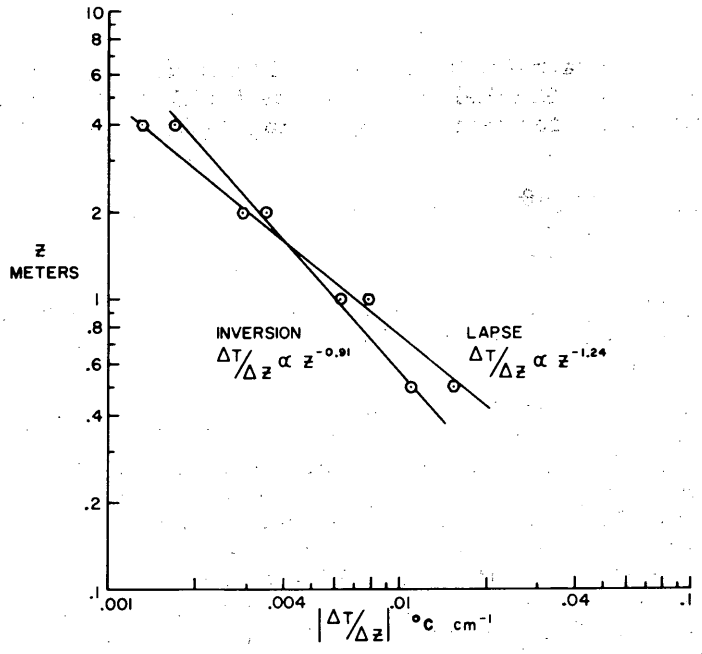

Figure 16. Height variation of temperature gradient ($\Delta T/\Delta z$).

geometric mean height of 0.5 m to $z_1 = 2.83$ and $z_2 = 5.66$ for a geometric mean height of 4.0 m. Results of the computations are shown in Figure 16.

In each stability condition $|\Delta T/\Delta z|$ decreased with height. Values of $\Delta T/\Delta z$ decreased from +0.011 C/cm at 0.5 m to 0.0017 C/cm at 4.0 m for the inversion and from -0.015 C/cm at 0.5 m to -0.0013 C/cm at 4.0 m for the lapse. A least squares analysis gave

$$|\Delta T/\Delta z| \propto z^{-0.91}$$

and

$$|\Delta T/\Delta z| \propto z^{-1.24}$$

for the inversion and lapse conditions, respectively.

The results described above are summarized in Table IV.

Table IV. Height exponents for scintillation and turbulence parameters.

	Inversion	Lapse
Pm	-0.35	-0.49
a	-0.14	+0.11
$\|Ri\|$	+0.23	+1.36
C_T	-0.35	-0.48
$\|\Delta T/\Delta z\|$	-0.91	-1.24

Discussion

It is evident that C_T and Pm have nearly identical height exponents for both stability conditions. The height exponents for C_T were further substantiated by adding those for terms comprising eq 5.1, using the identity

$$z\frac{\partial\theta}{\partial z} \equiv \frac{\delta\theta}{\delta \ln z} = \frac{\theta_2 - \theta_1}{\ln \frac{z_2}{z_1}}$$

proposed by Lettau (1957). The sum of the exponents was -0.37 and -0.46 for the inversion and lapse, respectively, which was close agreement with those given in Table IV.

The similarity of Pm and C_T indicates that eq 5.1 for computing C_T for stability conditions not very different from adiabatic was valid for the conditions of turbulence which existed during the experiments. Eq 5.1 was developed by assuming a turbulence regime of forced convection, one in which the production of convective energy by temperature differences is small compared to the rate of production of mechanical energy by shear forces. A typical weather condition for which this type of flow can be expected is a windy day or night with an overcast sky. A free convection regime, on the other hand, is one in which the vertical transfer of heat and momentum by mechanical turbulence is very small compared to that by buoyancy resulting from surface heating. A typical weather condition for which this type of flow can be expected is near midday in the summertime with a clear sky and a very low wind speed.

Much work has been done by others to establish criteria for the structure of temperature and wind in forced and free convection. How well the results of the scintillation measurements agree with these criteria in relation to flow characteristics for the lapse and inversion is discussed below.

Flow characteristics for the lapse data. Deductions concerning the height variations of C_T may be based on the theory of locally uniform and isotropic turbulence. In shear flow for a fully forced convection regime it can be shown that if temperature fluctuations obey the $\frac{2}{3}$ law, then

$$C_T \propto z^{-\frac{1}{3}}$$

and for free convection, Obukhov (1960) showed with dimensional analysis of a self-simulating regime that

$$C_T \propto z^{-\frac{2}{3}}.$$

Recent work by Tsvang (1963) supported the latter result with airplane measurements of temperature spectra at several heights between 50 and 3000 m during strongly developed convection.

For the present experiments, the height exponents for C_T and Pm were approximately the average of those expected for free and forced convection which indicates a transitional type of flow. Additional supporting evidence is the work by Priestley (1959) and Crawford (1963) in terms of Ri. Both workers showed that a regime of predominantly forced convection changed

to one of free convection for Ri between -0.02 and -0.05. The value of Ri at 0.75 m was -0.04 in the present experiments.

A similar result in relation to the type of flow was obtained for the variation of $\Delta T/\Delta z$ with height. The height exponent -1.24 compares to values of -1 for forced convection, -1.33 for free convection, and -2 for natural convection, i.e., no horizontal wind, found by others. A 30% greater slope of $\Delta T/\Delta z$ for the lapse than for the inversion is similar to that for Pm and C_T.

Flow characteristics for the inversion data. For inversion conditions, a transition from a turbulent regime of forced convection to laminar motion occurs as thermal stability increases. The effects on scintillation were discussed in USA CRREL Research Report 111, Part II. Comparatively little experimental or theoretical information, however, is available concerning the height variation of C_T or $\Delta T/\Delta z$ as far as establishing criteria for the transition in flow regimes for inversion conditions is concerned. Tsvang (1963) reported results of one flight during an inversion in which measurements of temperature spectra were made between 100 and 1000 m. He found

$$C_T \propto z^{-1},$$

which is much different from our findings, but he did not account for his result.

Most of the work in this regard has been in relation to Ri. For example, Portman et al. (1962), Townsend (1957), and Ellison (1957) estimated values of +0.35, +0.1 and +0.1, respectively, for Ri at which turbulence changes character and is gradually replaced by internal gravity waves. It is likely that the present experiments were conducted in a forced convection regime in which turbulence had not begun to decay, since Ri = +0.08 at 0.75 m.

Summary and conclusions

Scintillation intensity was three times greater at a height of 0.5 m than at 4 m for a lapse and two times greater for an inversion. A consistent decrease with height was corroborated by information obtained from wind and temperature profiles. Close agreement between the height variation of scintillation intensity and the structure constant for temperature fluctuations was obtained.

The height exponents for both Pm and the computed turbulence parameters indicated a mode of heat transfer between that of forced and free convection for the lapse and between forced convection and laminar flow for the inversion.

Spectral analysis of scintillation frequency showed an increase in the frequency of maximum power with height in each stability condition. The increase agreed closely with the wind profile measured simultaneously. Even though the measurements of scintillation discussed above were made with an incandescent light source, a similar height variation of scintillation intensity and frequency would also have been expected for the same meteorological conditions if the laser described in Section 3 had been used. The results are, therefore, also applicable to the problem of laser propagation discussed above.

LITERATURE CITED

Biggs, W.G. (1966) Measurement and analysis of turbulence near the ground with a hot-wire anemometer system, PhD. Thesis, University of Michigan, 128 p.

Bolgiano, R., Jr. (1962) Structure of turbulence in stratified media, Journal of Geophysical Research, vol. 67, no. 8, p. 3015-3023.

Chernov, L.A. (1960) Wave propagation in a random medium. Translation by R.A. Silverman. New York: McGraw-Hill Book Company.

Crawford, T.V. (1963) Eddy diffusivity as a function of stability, Department of Agricultural Engineering and Department of Irrigation, University of California, Final Report, USAEPG Contract No. DA-36-039-SC-80334, p. 125-133.

Ellison, T.H. (1957) Turbulent transport of heat and momentum from an infinite rough plane, Journal of Fluid Mechanics, no. 2, p. 456-466.

Gurvich, A.S.; Tatarski, V.I.; and Tsvang, L.P. (1958) An experimental research on the statistical characteristics of scintillation of a light source at ground level, (translation by E.R. Hope). Proc. Doklady Akad Nauk SSSR, 123, p. 655-658.

Hufnagel, R.E. and Stanley, N.R. (1964) Modulation transfer function associated with image transmission through turbulent media, Journal of the Optical Society of America, vol. 54, no. 1, p. 52-61.

Karman, Th. von and Howarth, L. (1938) On the statistical theory of isotropic turbulence, Proceedings of the Royal Society (London), vol. 164A, no. 2, p. 192-215.

Kolmogorov, A.N. (1941) Local structure of turbulence in an incompressible liquid for very large Reynolds numbers, Proc. Akad Nauk SSSR, vol. 30, no. 4.

Kovasznay, L.S.G.; Miller, L.T.; and Vasudeva, B.R. (1963) A simple hot-wire anemometer, The Johns Hopkins University, Project Squid, Technical Report. JHU-22-P.

Lettau, H.H. and Davidson, B. (1957) Exploring the atmosphere's first mile. Pergamon Press Inc., 1, 376 p.

McCready, P.B. (1962) The inertial subrange of atmospheric turbulence, Journal of Geophysical Research, p. 1051-1059.

Meyer-Arendt, J.R. and Emmanuel, C.B. (1965) Optical scintillation; a survey of the literature, U.S. Department of Commerce, National Bureau of Standards, Technical Note 225, 139 p.

Monin, A.S. (1962) On the turbulence spectrum in a thermally stratified atmosphere, (translation by Irving Emin). Izvestia Akad Nauk SSSR, Geophys. Ser., p. 266-271.

Obukhov, A.M. (1949) Structure of the temperature field in turbulent flow, Izvestia Akad Nauk SSSR, Geogr. and Geophys. Ser., vol. 13, p. 58.

_____ (1953) On the effect of weak atmospheric inhomogeneities on sound and light propagation, Izvestia Akad Nauk SSSR, Geophys. Ser., vol. 2, p. 155-165.

LITERATURE CITED (Cont'd)

Obukhov, A.M. (1960) The structure of temperature and velocity fields in free convection, Izvestia Akad Nauk SSSR, Geophys. Ser., vol. 9, p. 1392-1396.

Portman, D.J.; Elder, F.C.; Ryznar, E.; and Noble, V.E. (1962) Some optical properties of turbulence in stratified flow near the ground, Journal of Geophysical Research, vol. 67, no. 8, p. 3223-3235.

_____; Ryznar, E.; Elder, F.C.; and Noble, V.E. (1964) Visual resolution and optical scintillation over snow, ice, and frozen ground, U.S. Army Cold Regions Research and Engineering Laboratory Research Report 111, Part I, 32 p.

_____; Ryznar, E.; and Elder, F.C. (1965) Visual resolution and optical scintillation over snow, ice, and frozen ground, USA CRREL Research Report 111, Part II, 44 p.

Priestley, C.H.B. (1959) Turbulent transfer in the lower atmosphere. Chicago: University of Chicago Press, 130 p.

Ryznar, E. (1965) Dependency of optical scintillation frequency on wind speed, Applied Optics, vol. 4, no. 11, p. 1416-1418.

Sutton, O.G. (1953) Micrometeorology. New York: McGraw-Hill Book Co., 333 p.

Tatarski, V.I. (1961) Wave propagation in a turbulent medium. Translation by R.A. Silverman, New York: McGraw-Hill Book Co., 285 p.

_____; Gurvich, A.S.; Kallistratova, M.A.; and Terenteva, L.V. (1958) The influence of meteorological conditions on the intensity of light scintillation near the earth's surface, Journal of Soviet Astronomy, vol. 2, p. 578-581. Translation by American Institute of Physics Advisory Board of Russian Translations.

Townsend, A.A. (1957) Turbulent flow in a stably stratified atmosphere, Journal of Fluid Mechanics, vol. 3, p. 361-372.

Tsvang, L.R. (1960) Measurements of temperature-pulse frequency spectra in the surface layer of the atmosphere, Izvestia Akad Nauk SSSR, Geophys. Ser., p. 833-838. Translation by K. Syers.

_____ (1963) Some characteristics of the spectra of temperature pulsations in the boundary layer of the atmosphere, Izvestia Akad Nauk SSSR, vol. 10, p. 961-965. Translation by C.M. Wade.

Yaglom, A.M. (1949) On the local structure of the temperature field in turbulent flow, Proc. Akad Nauk SSSR, vol. 69, no. 6, p. 743.

APPENDIX A. SPECTRAL ANALYSIS

by

Arif A. Waqif

Introduction

This appendix discusses the technique used for estimating the spectral densities of random signals encountered in the data acquisition and data analysis. The technique used basically employs analog filtering. And, as in most spectral analysis techniques, assumptions of stationarity and ergodicity are implicit.* When random processes in nature are assigned chi-square distributions, a certain confidence level and the acceptable region of variability of the estimated statistic from its true value can be established. It is also important that all statistical estimates be interpreted with an awareness of estimation errors and instrument errors. Estimation errors arise due to the variance of the estimate about its true value and a bias error, while instrument errors may arise because of equipment noise and their time and frequency domain characteristics.

In the following, these errors are discussed for the spectral analysis technique. The following two sections are intended as a tutorial on spectral density and its analog estimation. The later sections describe the equipment used, and errors and difficulties encountered. Data acquisition instrumentation is covered elsewhere (Portman et al., 1964; Biggs, 1966).

Background for spectral analysis

The subject of spectral analysis has been covered widely in the literature, e.g.: Davenport and Root (1958), Blackman and Tukey (1958), and Bendat and Piersol (1966). The following section develops, briefly, the general concepts involved in spectral interpretation of random variables.

List of symbols

$b[f(\circ)]$	bias error in $f(\circ)$
$f^{(n)}(\circ)$	nth derivative of $f(\circ)$ with respect to the argument $(\circ)$
$\hat{f}(\circ)$	estimate of $f(\circ)$
j	$\sqrt{-1}$
$p(x)$	probability density function of a random variable $x(t)$
$w(t)$	impulse response function
A'	effective value of A, a constant
B_e	equivalent bandwidth
$E[f(\circ)]$	expectation operator

*Analysis of nonstationary random processes is discussed by Bendat and Piersol (1966), and others.

E_n	energy in the nth order filter
$G_{xx}(f)$	spectral density defined as a function of non-negative frequency
$MS[f(\circ)]$	mean square value of $f(\circ)$
R_s	frequency scanning rate in cps/sec
$R_{xx}(t, t+\tau)$	autocorrelation function
$S_{xx}(f)$	spectral density defined as a function of both positive and negative frequency
T_a	true averaging time constant
T_e	rise time for a short cutoff filter
T_m	delay introduced by the lag window
T_n	sample length
T_s	scanning time per frequency in sec/cps
$X(f)$	Fourier transform of x(t)
$Y(f)$	frequency response function
ϵ_m	modulation error
ϵ_n	normalized standard error in the estimate
ϵ_s	statistical error in the estimate
Δf_e	elementary frequency bandwidth resulting from the periodicity of the loop tape
Δf_r	resolution bandwidth
$\sigma[\hat{G}_{xx}(f)]$	standard deviation of the estimated spectrum from its true value

Definitions. Spectral density (or power spectral density) may simply be defined as that function which gives the distribution in frequency of the power of a signal or a noise. If x(t) is a real or complex-valued periodic function of a real variable t, and if x(t) is absolutely integrable over a period T (for non-periodic x(t), T may be ∞), i.e., if

$$\int_0^T \left| x(t) \right| dt < \infty, \qquad \text{(A1)}$$

then x(t) has associated with it a Fourier series

$$\hat{x}(t) = \sum_{n=-\infty}^{\infty} a_n e^{jnw_0 t}, \quad w_0 = \frac{2\pi}{T},$$

$$\left(a_n = \frac{1}{T} \int_0^T x(t)\, e^{-jnw_0 t}\, dt\right) \tag{A2}$$

where a_n are Fourier coefficients.

If x(t) is of integrable square, i.e.,

$$\int_0^T \left| x(t) \right|^2 dt < \infty, \tag{A3}$$

then the Fourier series converges in the mean to the function x(t). Under the same conditions,

$$\sum_{n=-\infty}^{\infty} \left| a_n \right|^2 = \frac{1}{T} \int_0^T \left| x^2(t) \right| dt \quad \text{(Parseval).} \tag{A4}$$

If the Fourier transform X(f) of x(t), defined as

$$X(f) = \int_{-\infty}^{\infty} x(t)\, e^{-j2\pi ft}\, dt, \tag{A5}$$

is also of integrable square, then

$$\int_{-\infty}^{\infty} \left| X(f) \right|^2 df = \int_{-\infty}^{\infty} \left| x(t) \right|^2 dt. \tag{A6}$$

The spectral density $S_{xx}(f)$ of x(t) may then be defined as a function of the Fourier coefficients:

$$S_{xx}(f) = \sum_{n=-\infty}^{\infty} \left| a_n \right|^2 \delta(f - nf_0), \quad f_0 = \frac{1}{T}. \tag{A7}$$

Thus spectral density at any frequency is the time average of the energy at that particular frequency.

Usually, a one-sided spectral density, or power spectrum, $G_{xx}(f)$ is defined such that

$$\int_{-\infty}^{\infty} S_{xx}(f)df = \int_{0}^{\infty} G_{xx}(f)df, \tag{A8}$$

and since $S_{xx}(f)$ is an even function of f,

$$2S_{xx}(f) = G_{xx}(f). \tag{A9}$$

Total energy in x(t) is

$$\int_{0}^{\infty} G_{xx}(f)df = \sum_{n=-\infty}^{\infty} \left|a_n\right|^2 = \frac{1}{T} \int_{0}^{T} \left| x^2(t) \right| dt. \tag{A10}$$

Two functions x(t) and x'(t) with Fourier coefficients of the same magnitude but different phases have the same spectral density. For x(t) real, $S_{xx}(f)$ is an even function of f. $S_{xx}(f)$ is non-negative.

Spectral density, or more precisely, power spectrum $G_{xx}(f)$, may be interpreted in a more statistical sense: it is the distribution of the mean square value of a random variable x(t) as a function of frequency. Thus if $G_{xx}(f_1)$ exists for a certain frequency f_1, and in a bandwidth Δf, then

$$G_{xx}(f_1) = \lim_{\Delta f \to 0} \lim_{T \to \infty} \frac{1}{\Delta f T} \int_{0}^{T} x^2(t, \Delta f)dt. \tag{A11}$$

That is, $G_{xx}(f_1)$ is the mean square value of the function x(t) in the bandwidth Δf around frequency f_1. In general,

$$G_{xx}(f) = \lim_{\Delta f \to 0} \lim_{T \to \infty} \frac{1}{\Delta f T} \int_{0}^{T} x^2(t, f, \Delta f)dt. \tag{A12}$$

Then the mean square value over the entire frequency range is equal to the total Fourier energy:

$$MS[x] = \int_{0}^{\infty} G_{xx}(f)df = \sum_{n=-\infty}^{\infty} \left|a_n\right|^2. \tag{A13}$$

The root mean square value is then interpreted as the standard deviation σ_x. The dc component, or the mean value, which appears as a delta function at f = 0 on the spectral plot, is usually not considered a useful statistical property.

Preference of one interpretation of spectral density over the other is more or less a personal matter. Although both meanings are equally

correct, it is sometimes difficult to reconcile oneself to the statement that a random variable, which is by definition nondeterministic, has a time domain representation as a Fourier series.

Assumptions. Stationarity: Stationary random processes are those whose statistical properties, computed from their ensemble averages, are time-invariant. However, it is not necessary to require that all moments of a process be independent of time for general statistical analysis. It is sufficient to require that second moments of a random process be time-invariant. This is referred to as wide-sense stationarity. If the ensemble autocorrelation function

$$R_{xx}(t,\ t+\tau) = E[x(t)\ x(t+\tau)] = \int_{-\infty}^{\infty} x(t)\ x(t+\tau)\ p(x)dx, \quad \text{(A14)}$$

(where $p(x)$ is the probability density function), then for a wide-sense stationary process $R_{xx}(t,\ t+\tau)$ is independent of t, i.e.,

$$R_{xx}(t,\ t+\tau) = R_{xx}(\tau). \quad \text{(A15)}$$

For a wide-sense stationary process, according to the Wiener-Khintchine theorem, autocorrelation function and spectral density are Fourier transforms of each other. Thus, for one-dimensional spectral density to exist, wide-sense stationarity is a necessary and sufficient condition.

Most random processes in nature can be assumed to be wide-sense stationary, at least for some time interval. Analysis of stationary processes is considerably simplified and their statistical properties are more familiar than those of non-stationary processes. The latter have multi-dimensional statistical properties which are more difficult to interpret.

Ergodicity: In a very general sense, an ergodic random process is one in which each sample function eventually takes on nearly all the modes of behavior of each other sample function. In statistics, ergodicity derives its usefulness from Birkoff's ergodic theorem which states that for a stationary random process, the time average exists for every sample function except for a set with probability zero, and under the condition of ergodicity, the time average is equal to the ensemble average with probability one. One direct result of Birkoff's theorem is the following:

$$E[x(t)\ x(t+\tau)] = \int_{-\infty}^{\infty} x(t)\ x(t+\tau)\ p(x)\ dx$$

$$= \lim_{T\to\infty} \frac{1}{2T} \int_{-T}^{+T} x(t)\ x(t+\tau)\ d\tau, \quad \text{(A16)}$$

i.e., the time autocorrelation function is equal to the ensemble autocorrelation function. In general, all ensemble averages can be interchanged for

time averages when the condition for ergodicity is satisfied. This condition is usually a complex mathematical requirement whose discussion is beyond the scope of this report. However, for gaussian random processes with continuous autocorrelation functions, the following condition implies ergodicity:

$$\int_{-\infty}^{\infty} \left| R_{xx}(\tau) \right| d\tau < \infty. \tag{A17}$$

When dealing with statistical properties of random processes in the real physical world, it is impracticable to use ensemble averages. Ergodicity condition ensures that all properties computed from time averages are the same as those computed from ensemble averages. In other words, one need not have an ensemble of random outputs available from the same random process to study its statistical properties. It is possible to study a wide-sense stationary ergodic random process by computing its statistical properties from a single observed time history.

Chi-square distribution: Physically observed phenomena are usually the net result of various random variables. The interplay of these variables in producing the phenomena observed may be quite complex. However, a physically observed phenomenon approaches a generalized distribution of the type chi-square

$$\chi_k^2 = y_1^2 + y_2^2 + \ldots\ldots + y_k^2, \tag{A18}$$

where y_i are normally distributed independent random variables. The y_i may themselves be sums of other independent random variables which may not be normally distributed. By virtue of the central limit theorem, however, y_i can be assumed to be normal. The theorem states essentially that sums of independent random variables under fairly general conditions will be approximately normally distributed, regardless of the underlying distributions. Thus the chi-square distribution seems to be an appropriate statistical description for most physical phenomena.

The chi-square distribution is also a very convenient and useful statistical tool. Its assumption helps a great deal in interpreting the random phenomenon. One can establish confidence intervals for the estimated statistical properties from distribution tables. In eq A18, the chi-square distribution has k degrees of freedom. As k becomes large ($k \gg 2$) the chi-square distribution itself approaches a normal distribution. The spectral density of a random variable with a large k is well-behaved and smooth, i.e., the first derivative of the spectral plot with respect to frequency is bounded and continuous.

Analysis of technique

The technique used for the estimation of spectral density utilized analog equipment. In its simplest form, the method involves passing the random signal through a narrow bandwidth filter which sweeps through the range of frequencies of interest at a desired rate to yield an analog voltage or current whose amplitude varies with power at and around each frequency. However, in practice, various parameters come into play: filter shape;

bandwidth and the sample period; noise, distortion, and the heterodyne effect; time constant of the power-averaging circuits; and frequency scanning rate.

Shape of the filter transfer function. For true spectral density, as defined by eq 12, ideally we would like a sharp cutoff filter with zero bandwidth. But in practice we can obtain only an estimate of the true spectral density because both these characteristics are physically non-realizable.

Very simply, the following holds for a filter:

$$G_{xx_{out}}(f) = \left|Y(f)\right|^2 G_{xx}(f), \tag{A19}$$

where $x_{out}(t)$ is the output of a filter with $x(t)$ as its input, the filter transfer function being $Y(f)$. $Y(f)$ may be thought of as a "spectral window" whose Fourier transform, the "lag window," is the impulse response of the filter. For an ideal sharp cutoff filter of bandwidth Δf,

$$Y(f) = 1, \; f_1 - \frac{\Delta f}{2} < f \leq f_1 + \frac{\Delta f}{2}, \tag{A20}$$

$$= 0 \text{ otherwise.}$$

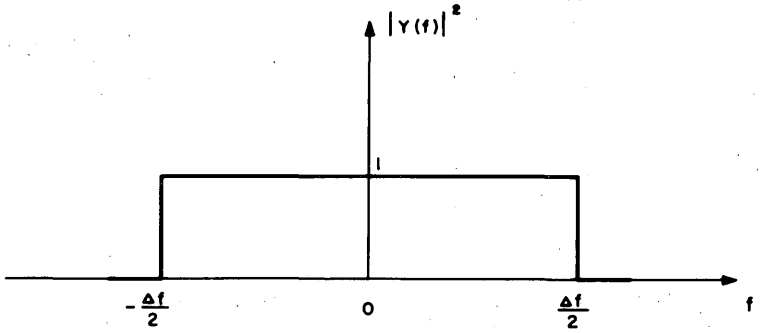

Figure A1. Amplitude transfer function of an ideal band-pass filter; $f_1 = 0$.

The impulse response of the ideal filter is of the form

$$w(t) = \Delta f \frac{\sin t \frac{\Delta f}{2}}{t \frac{\Delta f}{2}}. \tag{A21}$$

APPENDIX A

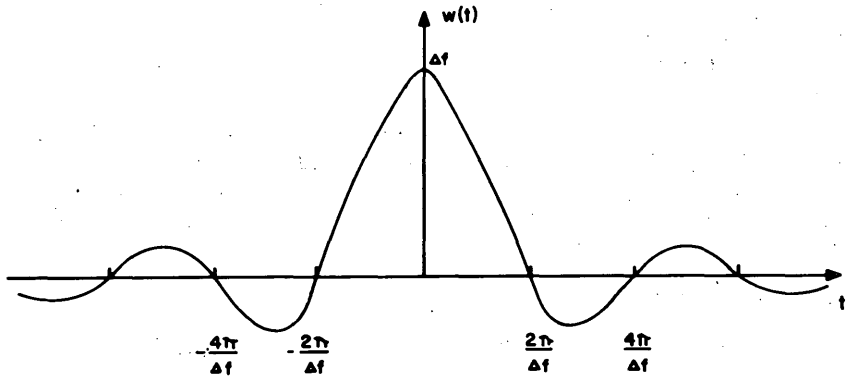

Figure A2. Impulse response of an ideal band-pass filter.

The following is apparent from Figures A1 and A2: As $\Delta f \rightarrow 0$ for the ideal narrow-band filter, the Y(f) function approaches an impulse function, and the w(t) function asymptotically approaches a horizontal line parallel to the t axis. For Δf very small, w(t) extends from $t = -\infty$ to $t = +\infty$. In other words, a narrow-band, ideal sharp cutoff filter requires infinite weighting in the time domain. Such a filter is physically non-realizable.

In the laboratory, one must deal with realizable filters, i.e., those whose impulse responses vanish for $|t|$ greater than some finite value of time. As this condition of realizability is introduced, the sharp cutoff characteristic of the frequency transfer function is lost.

A non-ideal, realizable, first order band-pass filter may be defined as the polynomial:

$$Y_1(s) = \frac{k_1 s}{\left(1 + \frac{s}{w_\ell}\right)\left(1 + \frac{s}{w_h}\right)}, \tag{A22}$$

where k_1 is a gain constant so that the peak gain is unity, s is the complex Laplace frequency; w_ℓ and w_h are, respectively, lower and higher frequencies off resonance at which the attenuation is 3 db. We can simplify this function by substituting $s = jw$:

$$Y_1(jw) = \frac{k_1 jw}{\left(1 + \frac{jw}{w_\ell}\right)\left(1 + \frac{jw}{w_h}\right)}. \tag{A23}$$

The actual $\ln(Y_1(jw))$ versus $\ln w$ may be approximated by the asymptotic representation for high frequencies. Figure A3 then represents the filter function graphically. In general,

$$Y_n(jw) = \frac{k_n (jw)^n}{\left(1 + \frac{jw}{w_\ell}\right)^n \left(1 + \frac{jw}{w_h}\right)^n}. \tag{A24}$$

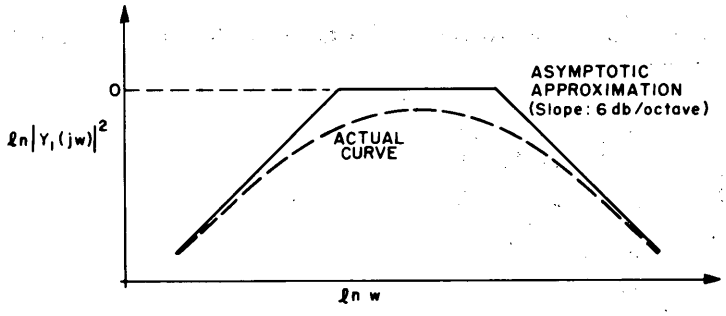

Figure A3. Amplitude transfer function of first order band-pass filter.

For $Y_n(jw)$, the slopes of the inclined lines are 6n db/octave. It should be noted that as n approaches ∞, the filter transfer function approaches the ideal rectangular transfer function.

A filter represented by eq A24 also introduces phase lags and leads. Every zero in the polynomial introduces a lead of approximately $\pi/2$ radians; a pole introduces a lag of $\pi/2$ radians. These phase changes shift frequencies in the filter to some extent. The predominantly lag effect, combined with random phases of neighboring frequencies acting as noise, makes it difficult to identify frequencies exactly.

As is apparent from eq A24, the analytical computation of both gain and phase errors from this expression for non-ideal filtering seems rather involved. McRae (1961) and McRae and Smith (1962) integrated this and other expressions for non-ideal filters numerically to study their effect on interpolation techniques. A "feeling" for the error can be obtained from his tables for interpolation errors. For band-limited white data (sharp cutoff at f_m) sampled at 24 times f_m a second order Butterworth interpolating filter introduces about 2% error, a third order filter about 0.5%, a fourth order filter about 0.2%. For a third order data roll-off (-18 db/octave) and a sampling rate of about 9 times f_m (f_m here is the -3 db point), the interpolation error figures corresponding to second and third order filters are 10% and 5%.

Let us now define certain parameters associated with filters. For non-ideal filters, we assume that a maximum time delay of T_m seconds is required. Then the "resolution bandwidth," Δf_r, is defined as the minimum bandwidth for which the spectral density can be estimated:

$$\Delta f_r \triangleq \frac{1}{T_m}. \tag{A25}$$

If T_n is the total sample length in seconds, then the "elementary frequency band," Δf_e, which is considered the fundamental Fourier frequency due to the periodicity of the tape loop, is given by

$$\Delta f_e \triangleq \frac{1}{2T_n}, \tag{A26}$$

For non-ideal filters, the "equivalent bandwidth," B_e, is defined as the bandwidth of a hypothetical rectangular filter which would pass the signal

with the same mean square statistical error as the actual filter when the input is white noise:

$$B_e \triangleq \frac{\left[\int_0^\infty |Y(f)|^2 \, df\right]^2}{\int_0^\infty |Y(f)|^4 df}. \tag{A27}$$

Both amplitude and frequency resolution of a filter are closely related to the filter bandwidth and sample length. We therefore turn to a discussion of these parameters.

Filter bandwidth and sample length. From eq A25, for good frequency resolution, we would like T_m to be very large. On the other hand, T_m cannot exceed T_n. It is also apparent that T_m should be less than or equal to the period of the lowest frequency in the data.

If a chi-square distribution for the random variable is assumed, then, by using the distribution tables, a formula for the amplitude accuracy of the spectral density estimate can be derived (Blackman and Tukey, 1958):

$$(90\% \text{ range in db})^2 = \frac{200}{T_n \Delta f_r}. \tag{A28}$$

If the term in parentheses is, say, 3 db, it implies that 90% of the spectral density estimates are within ± 3 db (± 50%) of the true spectral density. Thus

$$(90\% \text{ range in db})^2 = \frac{200 T_m}{T_n}. \tag{A29}$$

From eq A25 and A29, we see that we gain frequency resolution at the expense of amplitude accuracy, and vice versa. Thus a compromise has to be made. Usually,

$$T_m = 0.1 \, T_n \tag{A30}$$

is considered adequate. However, smaller T_m can be used to improve accuracy of the estimate if frequency resolution is not a prime consideration.

The degrees of freedom of the chi-square distribution can be calculated by the following formula:

$$k = \frac{B_e}{\Delta f_e} = 2 \, T_n \, B_e. \tag{A31}$$

Thus large T_n (or B_e) yields large k, which implies smoother spectrum plots, greater accuracy, and more discrete frequencies for which the spectral density can be estimated.

Any finite time history of a truly random process is a unique sample, so that spectral density estimated from this time history is itself a random function. Thus $\hat{G}_{xx}(f)$ has a mean square error about the true value $G_{xx}(f)$:

$$MS[\varepsilon_s] = E[\{\hat{G}_{xx}(f) - G_{xx}(f)\}^2]. \tag{A32}$$

On expanding the above equation, one can arrive at the following:

$$MS[\varepsilon_s] = \sigma^2[\hat{G}_{xx}(f)] + b^2[\hat{G}_{xx}(f)]. \tag{A33}$$

That is, the total mean square statistical error in the estimate is the sum of the variance of the estimate about its true value and the square of some bias error. In general, under certain compromises, both these errors may be made arbitrarily small as the sample period T_n becomes very large and B_e very small. However, this error can never be made equal to zero, as pointed out in the following.

The variance, $\sigma^2[\hat{G}_{xx}(f)]$, is a result of the fact that the difference between the estimate $\hat{G}_{xx}(f)$ and the true value $G_{xx}(f)$ is a random variable. This randomness is a direct consequence of the finiteness of the sample length. The following three equations are from Bendat and Piersol (1966). The expression for $\sigma^2[\hat{G}_{xx}(f)]$ is

$$\sigma^2[\hat{G}_{xx}(f)] = E[\hat{G}^2_{xx}(f)] - E^2[\hat{G}_{xx}(f)] \cong \frac{G^2_{xx}(f)}{B_e T_n}. \tag{A34}$$

The bias error is introduced because of averaging over a finite bandwidth in the filter:

$$b[\hat{G}_{xx}(f)] \cong \frac{1}{24} B_e^2 G^2_{xx}(f). \tag{A35}$$

Thus smaller bandwidth yields smaller bias error, but larger variance.

We see from above that the statistical error is related to the $B_e T_n$ product. A normalized standard error ε_n is defined in terms of the $B_e T_n$ product:

$$\varepsilon_n = \frac{\sigma[\hat{G}_{xx}(f)]}{G_{xx}(f)} \cong \frac{1}{\sqrt{B_e T_n}}, \tag{A36}$$

where $\varepsilon_n \times 100$ is percent error. The ε_n is a convenient means of determining a reasonable value of the $B_e T_n$ product. Usually $B_e T_n > 5$ is considered reasonable (error < 44%).

Noise and distortion. The subject of noise, distortion due to intermodulation and spectral "fold-over" (error of commission), and non-linear effects due to heterodyning (time domain multiplication of signals with intermediate or carrier frequencies) is considerably involved (see, for instance, Nichols and Rauch, 1966). Nevertheless, unless a fairly noisy

communication channel is used, available signal-to-noise ratios are usually fairly large (S/N > 20 db). Even then, unless the random signal to be analyzed has a more or less sharp cutoff spectrum, its tails are bound to be lost in low and high frequency noise in the equipment. High frequency noise is usually introduced from active elements in the electronics and low frequency noise may arise from high frequency drifts and characteristics of the transmission channels.

It is pointed out by Nichols and Rauch (1966) that for white band-limited noise (spectral density S_{nn}) in a frequency-modulated system, the mean square modulation error is

$$MS[\varepsilon_m] = \frac{2S_{nn}f_m^3}{3A_c^2} \qquad \text{(A37)}$$

where f_m = maximum frequency at which x(t) has non-zero power,

A_c = the amplitude of f_c, the carrier frequency.

It can be seen from the above equation that the error is considerably smaller for a relatively narrow-band signal than for a broad-band signal. If $f_m < f_c/2$, then "fold-over" distortion may be totally avoided. Intermodulation distortion, which arises due to heterodyning of two strong frequencies, may necessitate prewhitening of x(t) if $G_{xx}(f)$ is not relatively smooth or flat (see Bennet and Davy, 1965, and Bower and Schultheiss, 1958). Modulation products obtained in a non-linear modulation (of the type of FM) may have noise components which have reached the "threshold" value where it becomes difficult to separate noise from signal. For a given FM system, an expression can be derived for the frequency at which small noise assumptions break down and one has to use statistical estimators to separate signal from noise.

Time constant. The time constant of the power-averaging circuit determines the combined effect of transients in the filter and the amplifier circuits. If it is of the same order of magnitude as the sample length then considerable information about the variation of power density at any particular frequency may be lost. On the other hand, for low frequencies whose periods are comparable to the sample length, it may be necessary to have the time constant of the power-averaging circuit approach the sample length in magnitude in order to retain information at these frequencies.

It is sometimes recommended that the averaging time constant equal the effective sample length. But it is generally found that if the data bandwidth is narrow, and if the sample length is an order of magnitude, or more, larger than the period of the lowest frequency in the data, smaller time constants are quite satisfactory. Analysis time may be further reduced by decreasing the time constant as the analysis goes up in frequency.

Scanning rate. Frequency scanning rate is determined by the stability of the filter at low frequencies, transients in the electronics, and the filter bandwidth. Each frequency is scanned for a time T_s which allows for resonance build-up in the filter and for the transients in the power-averaging circuit to die down.

The rise time for an ideal sharp cutoff filter of bandwidth B_e is $T_e = 1/B_e$. If T_a is the true averaging time constant of the power averaging

circuit then each frequency should be looked at for at least $T_s = T_e + T_a$ seconds. Thus a scan rate $R_s = 1/(T_e + T_a)$ should be adequate for manual scanning.

The stability of the tuning circuit and bandwidth determines the minimum difference in frequencies for spectral density estimation. As mentioned above, a slowly varying spectrum implies more degrees of freedom and hence more discrete points for spectral density estimation.

Sometimes the scan rate R_s in cps per second is taken proportional to B_e/T_a. Usually $R_s < B_e/T_a$. In automated systems for spectral analysis, considerable analysis time can be saved by increasing the bandwidth and decreasing the averaging time as analysis goes up in frequency. This results in higher scanning rate at higher frequencies, and therefore faster analysis, without any increased loss of accuracy.

Description of instrumentation

In the previous section, the method used for analog estimation of power spectrum is analyzed with emphasis on errors introduced by the statistics of $G_{xx}(f)$ and the instrumentation used. We now turn to the equipment set-up and study its operation in some detail.

The following is a list of equipment used for spectral analysis:

I) Ampex Instrumentation Recorder SP-300

II) IBM-7090, CDC-160A Digital Computers, Applied Dynamics 2-64 PBC Analog Computer

III) Honeywell FM Recording Oscillator Model 4207

IV) Honeywell Direct Recording Amplifier Model 4114

V) Honeywell Laboratory Recorder/Reproducer Model KAR 7490

VI) Honeywell Tape Transport Model 3191

VII) Honeywell Data Discriminator Model 5207

VIII) Spectrum Analyzers:

Hewlett-Packard Harmonic Wave Analyzer Model 300A

Hewlett-Packard Harmonic Wave Analyzer Model 302A

Quantech Wave Analyzer Model 304

IX) Esterline-Angus MA Current Recorder

Figure A4 is a block diagram of the spectrum-analyzing system:

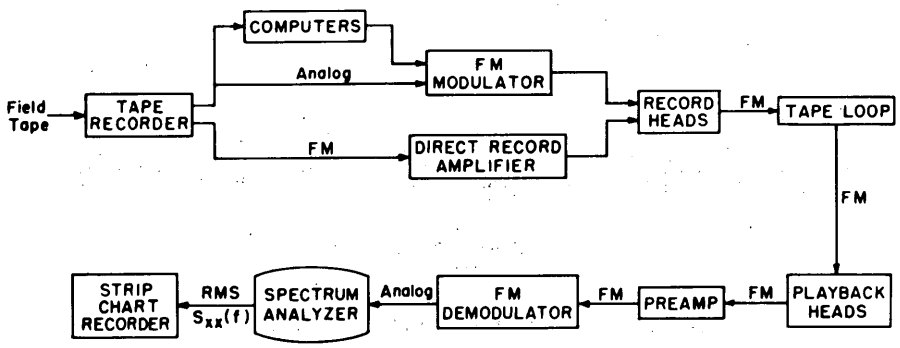

Figure A4. System block diagram.

The details of computations performed on computers to obtain wind component fluctuations are described by Biggs (1966).

The spectral analysis technique employs recording the frequency-modulated random signal on a continuous tape loop and repeatedly playing the demodulated signal back through a spectrum analyzer.

The random signal which is recorded at $3\frac{3}{4}$ ips as an FM signal can be played back either as a modulated signal (carrier frequency 3375 cps, modulation index ± 40%) or as a demodulated analog signal at one of the following speeds: $1\frac{7}{8}$, $3\frac{3}{4}$, $7\frac{1}{2}$, 15 ips. The ratio of the speed at which the signal is played back from the loop to the speed at which it is recorded on the loop gives the "frequency compression." By increasing the frequency compression, the capability of the spectrum analyzer can be enhanced to lower frequencies. The frequency compression used for spectral analysis was 1:16 or 1:32 (loop playback speed 60 ips; loop record speed $3\frac{3}{4}$ ips or $1\frac{7}{8}$ ips). The bandwidth of the FM system response is a function of the record speed (dc to 625 cps at $3\frac{3}{4}$ ips and dc to 312 cps at $1\frac{7}{8}$ ips).

FM recording electronics. These modules transfer the field data to the tape on the loop machine. The frequency-modulated signal from the tape recorder can be demodulated in the tape recorder and then recorded on the loop-tape through an FM modulator. Or, it can be recorded on the loop-tape without intermediate demodulation and modulation through a direct record amplifier.

The FM recording oscillator (FM modulator) is a transistorized module consisting of three basic sections (Fig. A5): a driver amplifier, a center frequency card, and a core oscillator-output amplifier.

The data signal is amplified in the dc driver amplifier. This amplified input is then frequency modulated in the core oscillator, the amplified output of which is applied to the recording head.

If the frequency-modulated signal is transferred to the loop through intermediate demodulation and modulation, the noise in the FM signal is essentially squared due to the heterodyning in the modulation process. By directly transferring the modulated signal from the SP-300 to the loop, multiplication of noise is avoided. A direct record module amplifies the modulated signal sufficiently to drive the recording head. A high frequency bias oscillator, whose output is mixed with the FM signal after amplification, causes the data signal to be recorded on the most linear portion of the magnetic hysteresis loop. Record level and bias level adjustments are provided on the panel.

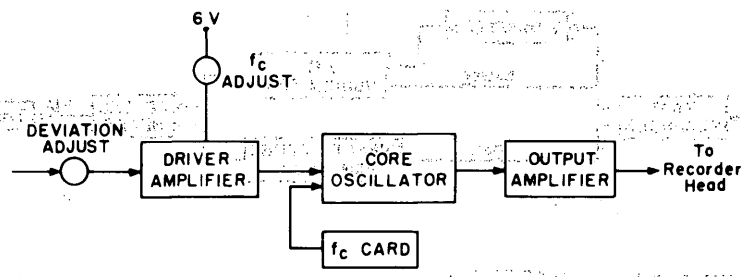

Figure A5. FM modulator block diagram.

The tape transport. To provide recording and continuous reproduction of data the tape transport has a loop of magnetic tape 105 ft long. It is capable of driving $\frac{1}{2}$-in. magnetic tape at six different speeds from $1\frac{7}{8}$ ips to 60 ips. There are seven tracks available for recording, and an erase oscillator to "erase" all tracks simultaneously.

Push-button controls are provided for stopping, playing back, recording, and erasing. The different modes are operated by actuating a series of interlocking relays. A closed-loop drive system is used to reduce flutter. The capstan is driven by a hysteresis-synchronous motor through a jack shaft and belt arrangement. A preamplifier is provided for each track to amplify signals from the playback head sufficiently to drive playback amplifiers or FM discriminators. In the laboratory arrangement, only one set of record and playback electronics was available. Hence, information was recorded on the seven tracks, when necessary, one at a time, and similarly played back.

The FM discriminator. Figure A6 is a block diagram of the demodulator used to convert the frequency-modulated signal from the loop tape to the original signal x(t):

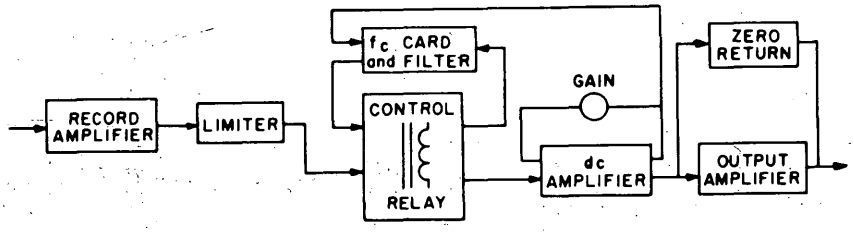

Figure A6. FM discriminator block diagram.

In conjunction with the tape loop, the FM discriminator module may be used with signals that have center frequencies ranging from 1.687 kc to 54 kc (corresponding to $1\frac{7}{8}$ ips to 60 ips tape speed). Four center frequency cards may be plugged in simultaneously and automatically switched on by the speed selector switch on the transport.

The FM is demodulated by essentially passing it through various stages of limiting and amplification. To remove the carrier frequency components from the output of the discriminator, an active filter is used in conjunction with the dc amplifier. The filter is in the form of an RC ladder structure on the center frequency card with positive and negative feedback from the dc amplifier. A feedback loop in the dc amplifier and a zero potentiometer, which determines the amount of bias applied to the amplifier, provide an output gain control. This gain control is usually adjusted to give a ratio 1:1 of the modulating input to the demodulated output. However, when input peak-to-peak values are in excess of ± 5 volts, the discriminator output-to-input ratio is adjusted to 0.5:1 in order to avoid clipped, and hence erroneous, outputs. A "zero-return" circuit is provided to protect instruments connected to the output of the discriminator. This circuit shorts the output terminals whenever the input signal becomes comparable to noise in the circuit or whenever the input signal is excessively high.

The data discriminator can receive a compensation signal – from a compensation discriminator – which is 180° out of phase with the data signal. This will electronically cancel out any distortion in the data signal resulting from variation in tape speed during recording and playback. This provision, however, was not made in the setup used.

The harmonic wave analyzer. This is the pivotal instrument in spectral analysis. As pointed out earlier, filter bandwidth, power-averaging time constant and frequency sweep rate are determining factors with respect to the accuracy of spectral density estimation. Harmonic wave analyzers provide control over these factors.

Three different analyzers were employed at one time or another. The general principle involved is the same, however, for all of them. A wave analyzer acts as a selective voltmeter and measures the voltage amplitude of complex waveforms within fixed or adjustable bandwidths. The input signal is heterodyned with an intermediate frequency (IF, around 100 kc). This mixing affords a simpler circuit design and sharper bandwidth control. The mixed signal is then passed through a tuned amplifier. Figure A7 is a generalized block diagram of the wave analyzer.

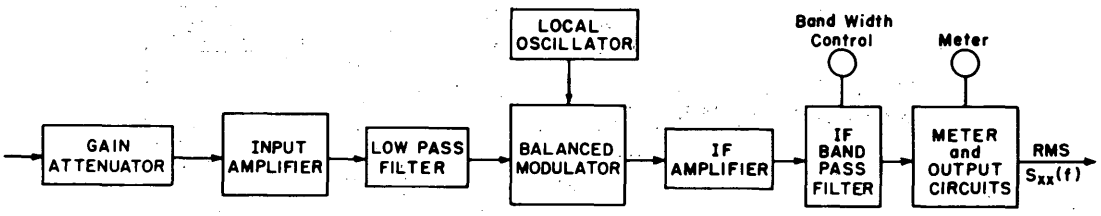

Figure A7. Wave analyzer block diagram.

The input attenuation and gain control keep the signal from overloading the input amplifier. The amplified signal is usually filtered to remove frequency components above the frequency range of the analyzer. This also removes any high-frequency noise that may have been added in the modulation and demodulation processes. The filtered signal is then mixed with an intermediate frequency from a local oscillator. The latter, which is usually voltage-controlled, has provisions for automatic gain and frequency control, and for calibration through inductive and capacitive control. The balanced modulator has a wide dynamic range and has various controls for carrier balancing. The frequency-converted signal is then amplified – and, sometimes, filtered again – before it is sent through a narrow-band-pass filter. The output of this filter is further amplified and then rectified. The rectified output is displayed on a current meter and is also available as a current or voltage output for strip chart recording.

The frequency range on the HP-300A analyzer is 20 cps to 16 kc, on the HP-302A 20 cps to 50 kc, and on the QT-304 1 cps to 5 kc. Thus, in principle, a frequency range of 1/32 cps to 3125 cps may be looked at. In fact, however, bandwidth, noise and other considerations (discussed in the following section) narrowed this to a useful range of about 1 cps to 625 cps.

Variable bandwidths on the HP-300A (7 cps to 40 cps at 3 db point) and QT-304 analyzers (1, 10, 100 cps at 3 db point) were available. A fixed bandwidth of 7 cps was available on the HP-302A.

Evaluation of instrumentation and procedures

In the section on analysis of technique, parameters which determine the accuracy of the estimated spectral density and types of errors introduced are discussed. The previous section describes the equipment that was used for spectral analysis. In this section, an attempt is made to determine the magnitude of errors introduced by various parameters. Only one wave analyzer is discussed in detail, but the results are applicable to the other two without much modification.

Shape of the filter transfer function. The filters used in the three wave analyzers were far from ideal. The HP-300A wave analyzer filter, for instance, has a roll-off which is about -12 db/octave at 10 cps off resonance, but which eventually approaches -18 db/octave for higher frequencies. We can approximate this to a third order filter.

The error introduced by a non-ideal filter in a power spectrum $G_{xx}(f)$ can be calculated by comparing the spectral energy in the non-ideal filter to that of an ideal filter in the specified bandwidth. It is apparent that a non-ideal filter passes more energy in a bandwidth than an ideal filter of the same bandwidth. By bandwidth for a non-ideal filter, a -3 db bandwidth is implied.

Let us ignore the phase error introduced by the filter in the HP-300A. We can assume that the amplitude versus frequency relationship is described by the Butterworth equation:

$$\left|Y_n(f)\right|^2 = \frac{1}{1 + \left(\frac{f}{f_0}\right)^{2n}}, \tag{A38}$$

where n is the order of the filter and f_0 is the -3 db frequency (n = 3, f_0 = 3.5 cps for HP-300A). This equation is plotted in Figure A8 for n = 1, 2, 3, 4 and ∞. Note that the plots are symmetric about the center frequency $f_1 = 0$.

Since we want to compare the energy differences between ideal and non-ideal filters, we consider the integral of eq A38 over a specified frequency range

$$E_n = \int_{f_1}^{f_2} \frac{1}{1 + \left(\frac{f}{f_0}\right)^{2n}}\, df, \tag{A39}$$

where E_n is the energy in the nth order filter.

The above equation was integrated graphically from Figure A8 for n = 2, 3, 4 and ∞. The percent difference in energies passed by non-ideal filters and the ideal filter, and percent of total energy lying outside the -3 db bandwidth were calculated. Frequencies at which gain decreased to less than 98% (.175 db attenuation) were read off the curves. Following is a tabulation of the results:

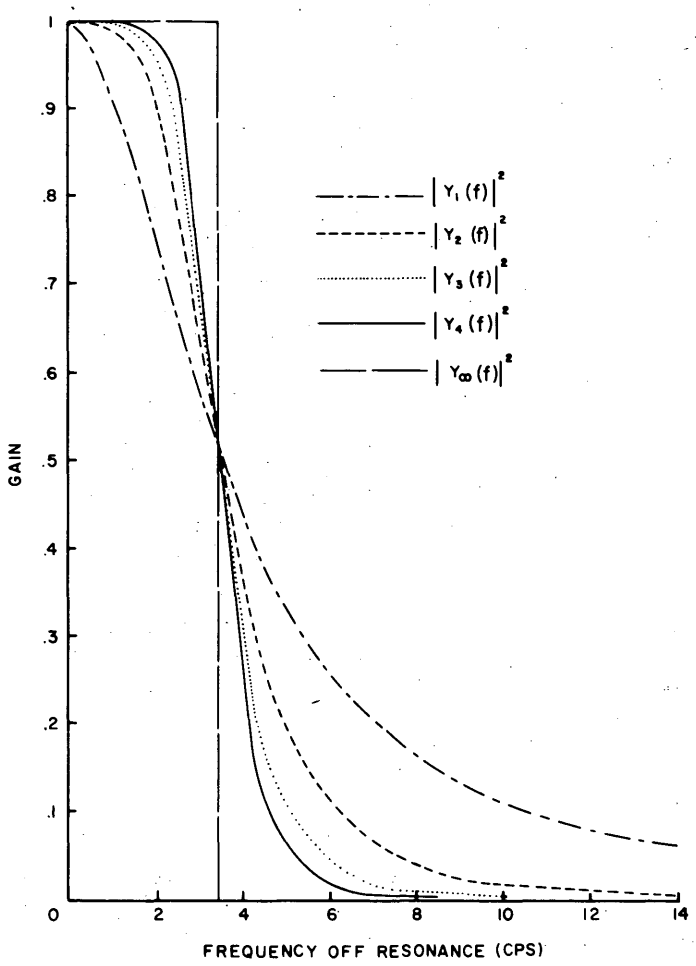

Figure A8. Butterworth amplitude characteristics for nth order filters $Y_n(f)^2$; $f_1 = 0$.

Order of filter	Percent energy difference	Percent energy for f > 3.5 cps	0.175 db cutoff freq
2	+22.62	40.4	1.25 cps
3	+11	28.2	1.75 cps
4	+ 8.6	20.8	2.1 cps
∞	0	0	3.5 cps

Thus it seems that a 3rd order filter is fairly reasonable, despite its 11% error. Going to a higher order filter does not reduce the error substantially. However, the fact that 11% more energy is passed through the 3rd order filter and that about 28% of energy lies outside the -3 db bandwidth should be kept in mind when evaluating spectral results.

We must now calculate the various parameters associated with the filter in the HP-300A.

To calculate the delay T_m, we observe that the amplitude characteristic of the filter is like the "hamming window." Knowing the dynamic range of the spectral analysis system to be 35 db, we can calculate a time delay $T_m = 1/20$ second. This T_m compares favorably with the one computed from the Butterworth shape of a third order filter (McRae, 1961):

$$T_m = \frac{2}{w_0} = \frac{2}{2\pi x\,(2x3.5)} \cong \frac{1}{22} \text{ second.}$$

This evidently shows that our assumptions of "hamming window" and a third order Butterworth filter are not too unreasonable. We will use $T_m = 1/20$ sec.

Sample lengths of $T_n = 5.5$ minutes and $T_n = 11$ minutes were possible on the loop machine. When the loop tape was played back at 60 ips, with a frequency compression of 16, the effective sample length $T_n' \cong 20$ sec.

Then, from eq A25, we have $\Delta f_r = 1/T_m = 20$ cps, and, from eq A26, $\Delta f_e = 1/2T_n = 1/660$ cps for $T_n = 330$ sec. For the equivalent bandwidth B_e, Blackman and Tukey (1958) show that B_e may be taken approximately equal to $1.3/T_m$ for hamming and hanning windows. Then $B_e = 1.3 \times 20 = 26$ cps.

Errors due to filter bandwidth and sample length. In general, it seems obvious that the shape of the $\hat{G}_{xx}(f)$ plot depends heavily on the filter bandwidth. If the filter bandwidth is large, greater smoothing and averaging take place and the $\hat{G}_{xx}(f)$ plot is relatively flat. For a filter with infinite bandwidth, or bandwidth greater than the data band, the $\hat{G}_{xx}(f)$ plot is a horizontal line, showing the overall mean square value of x(t). Forlifer (1964) has shown that as filter bandwidth increases, the half-power bandwidth of the measured spectrum increases and the peak value of the measured spectrum decreases.

As shown previously, B_e and T_n impose conflicting requirements for least error. We can now calculate the errors in the estimated power spectrum. Using eq A28:

$$(90\% \text{ range in db})^2 \cong \frac{200}{T_n' \Delta f_r} = \frac{200 \times 1}{20 \times 20} = \frac{1}{2}$$

$$\therefore \quad 90\% \text{ range in db} = \frac{1}{1.414} = 0.7072$$

i.e., 90% of the estimates are within approximately ± 11% of the true spectral density.

To calculate the degrees of freedom for a chi-square distribution we use eq A31. Due to the frequency compression at playback, we use effective sample length $T_n' = 20$ sec and effective equivalent bandwidth $B_e' = 26/16$ cps.

$$k = 2T_n' B_e' = 2 \times 20 \times \frac{26}{16} = 2.5 \times 26 = 65.0.$$

From the tables for a chi-square distribution, we interpret k = 65 as follows: If the long run average of an estimate is, say, 10 volts^2 /cps, then 90% of the estimates should lie between 7.7 volts^2 /cps and 12.3 volts^2 /cps. Also, if a single observed estimate is, say, 10 volts^2 / cps, then we have 80% confidence that the long run average lies between 8.1 volts^2 /cps and 12.9 volts^2 /cps.

The statistical error from eq A36:

$$\epsilon_n \cong \frac{1}{\sqrt{B_e' T_n'}} = \frac{1}{\sqrt{1.625 \times 20}} .$$

$$\% \text{ error} = \frac{100}{5.701} = 17.5\%.$$

Thus we find that the instrument error due to the shape of the filter function is about 11%, while statistical error due to variation of the estimate from its true value is about 17%.

Noise and frequency threshold. If the dynamic range (signal-to-noise ratio and frequency response) of the recording and data analyzing system is known, "threshold frequencies" may be established beyond which the spectral density estimates are predominantly influenced by noise. A noise test for dc signals indicated that noise levels were around 20 MV below $\frac{1}{8}$ cps, and dropped off sharply above 1 cps to a .1 to .5 MV range. For "erased" tapes on the loop, the noise level was around 200 μv below $\frac{1}{8}$ cps, and dropped off to 10 μv above $\frac{1}{2}$ cps. Thus it seems that spectral density estimates for frequencies below 1 cps were unreliable.

The high frequency threshold was obtained by either recognizing that the signal level had fallen down to the "noise floor" (less than 0.5 MV), or by considering the filter response of the low pass filter in the playback circuits in the SP-300 and the FM demodulator. A check on the reproduce electronics showed that the gain was nearly 1 (0 db) to about 600 cps for a tape speed of $3\frac{3}{4}$ ips. The half-power point was near 780 cps, and the filter roll-off rate was quite high (greater than 50 db/octave) beyond 800 cps. Thus it seems reasonable to assume that no significant error of "omission" was introduced by the playback filter for signal components up to 600 cps.

With the assumption of a "hamming window" it was shown that the resolution bandwidth Δf_r = 20 cps. Then $\Delta f_r'$ = 20/16 = 1.25 cps. Hence, to avoid multiple integration of power at lower frequencies an effective frequency range of 1.25 cps to 600 cps for the spectral analysis system was used.

Time constant. The power averaging circuit time constant used was T_a = 1 sec for frequencies f > 10 cps. For lower frequencies (1 < f ≤ 10) a time constant of 10 sec was sometimes used to avoid excessive variations on the strip chart record. With T_a = 1 sec, some of the nonstationary behavior of the spectral density was displayed on the strip chart. The lower time constants ($T_a < T_n'$ = 20 sec) also enabled quick identification of the spike in the strip chart record due to the splice in the loop-tape. Thus, no error was introduced due to the averaging circuit time constant.

Scanning rate. Only manual scanning was employed. Each frequency was usually looked at for a minimum of T_s = 40 sec. Although this T_s is

longer than the T_s theoretically necessary ($T_s \geq T_e + T_a = [1/1.625] + 1$), it was found convenient to use the longer scanning time as it reduced considerably errors introduced by visual averaging of the strip chart record, and as it facilitated discounting the spike due to the splice in the loop-tape. Considering the effective resolution bandwidth $\Delta f'_r = 1.25$ cps, the spectral density estimates at lower frequencies, starting from 1.25 cps with increments of 1.25 cps, avoided multiple averaging.

In this section amplitude and frequency resolution were discussed for the equipment setup used for spectral analysis. It was found that instrument amplitude error is about 11% while statistical amplitude error is about 17%. The useful frequency range was found to be 1.25 cps to about 600 cps.

Comments

The following specific comments can be made about the procedure.

Record mode. It was found, as expected, that the overall playback gain on data recorded on the loop-tape directly (without intermediate demodulation and modulation, see Figure A4) was higher than on the data recorded through a frequency modulator. The gain on a sine wave recorded through a frequency modulator was found to be about 75% of the gain on the same signal recorded directly on the loop as a frequency-modulated signal from the tape recorder. The principal reason for this loss of signal is, of course, the squaring of the noise power that results from intermediate modulation. But, with the equipment used in the laboratory, there were other factors which contributed to the loss of signal.

In direct record mode, the signal-to-noise ratio was greater than 50 db. Total harmonic distortion was about 1% maximum. The bias frequency of 460 kc, introduced to cause the data signal to be recorded on the most linear portion of the hysteresis loop, could be continuously adjusted, while recording, by a front panel meter control.

In the FM record oscillator, however, the signal-to-noise ratio decreased with recording speed (from 50 db at 60 ips to 40 db at $1\frac{7}{8}$ ips). Total harmonic distortion due to frequency mixing was higher (about 2%). Deviation and center frequency adjustments could not be made easily. Zero drift, sensitivity drift, and linearity drift introduced further inaccuracies in the data signal. The drifts were dependent on environmental temperature, and were not conveniently detected.

Spectrum repeatability. Spectra of the same data could not be repeated exactly on different days or on different wave analyzers. Part of the difficulties arose because only a finite time history was available. But instrument errors seem to account predominantly for lack of exact repeatability.

i) It was found that the FM discriminator gain setting is very sensitive to the playback speed and elapsed time between adjustments. Tests indicated the following: If the discriminator gain is adjusted to 1:1 for a known sine wave played back at 60 ips, gain goes down about 20% (to 0.8:1) at 15 ips, and about 25% (to 0.75:1) at $1\frac{7}{8}$ ips, all other parameters remaining unchanged. In an "over-night" test, it was found that the discriminator gain went down almost 30% for the same known sine wave recording. An average 10% decrease in power density was observed for a random signal.

ii) The calibration of the local oscillator in the wave analyzer is usually quite critical, especially for low frequency analysis. Wave analyzer electronics are temperature-sensitive, and even otherwise, not drift-free. The magnitude and direction of frequency drifts in analyzers is unpredictable. The HP-300A, being an older and a vacuum tube model, had large frequency drifts, as did the QT-304. (The HP-302A was relatively more stable.) Frequency drifts of 1 to 5 cps in an hour were sometimes observed. Thus exact frequency identification was not possible.

iii) General difficulty arose in being unable to calibrate two wave analyzers exactly to a "matched" gain and frequency state. The HP-300A calibration procedure is quite involved and time-consuming. The HP-302A and QT-304 calibration procedures are simpler, and can be more easily repeated.

iv) Some discrepancy was introduced because of different filter characteristics in the wave analyzers. The HP-300A has a four-stage RLC-tuned amplifier circuit for IF filtering, while the HP-302A uses a double crystal IF filter. The QT-304 uses 2-sec modulators with two active RC filters for IF filtering.

Although exact filter characteristics were not known for the HP-302A and QT-304 models, it would be unreasonable to assume that all three wave analyzers had the same filter response.

v) Some human error is introduced in dial settings on the wave analyzers, in sometimes-involved analyzer calibration procedures, in visually averaging the strip chart record, and in discriminator gain adjustment.

Concluding remarks

The analog technique utilizing the wave analyzer is usually quite suitable for spectral analysis when results are not needed for on-line use. This technique is quite flexible with respect to formating, pre-analysis monitoring and frequency range. Low cost and manpower requirements – as compared to those of the more sophisticated techniques using analog, digital, or hybrid computers – are also recommending factors. But, exact spectral density estimates cannot be obtained from a spectrum analyzer. The nature and magnitude of errors introduced, however, can be calculated quite accurately. Furthermore, these errors can be reduced considerably – though not totally eliminated – by using narrower, sharper filters, longer time histories, narrower data bands, higher signal-to-noise ratios, more stable electronics, and frequent equipment calibration and adjustment.

Spectral analysis techniques utilizing analog or digital computers have been developed for more accuracy and for large volumes of data. These techniques, based on the Wiener-Khintchine theorem, calculate the autocorrelation function using a special purpose analog or a digital computer, and then compute its Fourier transform. In a hybrid computer installation, the Wiener-Khintchine theorem can be used to calculate the spectral density estimate on the digital computer while the analog computer is programmed for pre-emphasis and de-emphasis of data (Thomas, 1966). Hybrid computer techniques based on the narrow-bandpass filter principle – where analog filters are digitally controlled through a hybrid interface – have also been developed (Hansen, 1966).

The decision to use a particular technique rests on various factors not the least important of which are: cost; desired accuracy; volume; use of spectral data; frequency range and data format; and availability of equipment, personnel and computer time. For most off-line operations, however, the technique using the spectrum analyzer is quite satisfactory.

LITERATURE CITED

Bendat, J.W. and Piersol, A.G. (1966) Measurement and analysis of random data. New York: John Wiley and Sons.

Bennet, W.R. and Davey, J.R. (1965) Data transmission. New York: McGraw-Hill.

Biggs, W.G. (1966) Measurement and analysis of the structure of turbulence near the ground with a hot wire anemometer system. University of Michigan, PhD thesis.

Blackman, R.B. and Tukey, J.W. (1958) Measurement of power spectra. New York: Dover Publications.

Bower, J.L. and Schultheiss, P.M. (1958) Introduction to the design of servomechanisms. New York: John Wiley and Sons.

Davenport, W.B. and Root, W.L. (1958) An introduction to the theory of random signals and noise. New York: McGraw-Hill.

Forlifer, W.R. (1964) The effects of filter bandwidth in spectrum analysis of random vibrations, Dept. of Defense, Washington, D.C., Shock Vibration and Associated Environments Bulletin No. 33, Part II.

Hansen, P.D. (1966) New approaches to the design of active filters, parts 1 and 2, Simulation, vol. 6, no. 5, 6.

McRae, D.D. (1961) Interpolation errors, Radiation Inc., Melborne, Florida, Advanced Telemetry Study Technical Report 1, parts 1 and 2.

_____ and Smith, E.F. (1962) Computer interpolation, Radiation Inc., Melborne, Florida, Advanced Telemetry Study Technical Report 2, parts 1 and 2.

Nichols, N.H. and Rauch, L.L. (1966) Radio telemetry. New York: John Wiley and Sons, Inc.

Portman, D.J.; Ryznar, E.; Elder, F.C.; and Noble, V.E. (1964) Visual resolution and optical scintillation over snow, ice, and frozen ground; part 1, U.S. Army Cold Regions Research and Engineering Laboratory Research Report 111.

Thomas, L.C. (1966) A hybrid computer technique for power spectrum analysis, Simulation, vol. 6, no. 4, p. 258-265.

Unclassified

Security Classification

DOCUMENT CONTROL DATA - R & D

(Security classification of title, body of abstract and indexing annotation must be entered when the overall report is classified)

1. ORIGINATING ACTIVITY (Corporate author)	2a. REPORT SECURITY CLASSIFICATION
U.S. Army Cold Regions Research and Engineering Laboratory, Hanover, N.H.	Unclassified
	2b. GROUP

3. REPORT TITLE

LASER SCINTILLATION CAUSED BY TURBULENCE NEAR THE GROUND

4. DESCRIPTIVE NOTES (Type of report and inclusive dates)

Research Report

5. AUTHOR(S) (First name, middle initial, last name)

Donald J. Portman; Edward Ryznar and Arif A. Waqif

6. REPORT DATE	7a. TOTAL NO. OF PAGES	7b. NO. OF REFS
January 1968	81	42

8a. CONTRACT OR GRANT NO.	9a. ORIGINATOR'S REPORT NUMBER(S)
DA-AMC-27-021-63 G7	
b. PROJECT NO.	Research Report 225
c. DA Task 1VO14501B52A02	9b. OTHER REPORT NO(S) (Any other numbers that may be assigned this report)
d.	

10. DISTRIBUTION STATEMENT

This document has been approved for public release and sale; its distribution is unlimited.

11. SUPPLEMENTARY NOTES	12. SPONSORING MILITARY ACTIVITY
	U.S. Army Cold Regions Research and Engineering Laboratory Hanover, N.H.

13. ABSTRACT Laser scintillation was measured for a horizontal optical path 500 m long and 1 m high for various conditions of horizontally homogeneous turbulence. Wind direction, average vertical distributions of wind speed and temperature, and, in some cases, turbulent fluctuations of wind velocity were measured simultaneously. The results of the measurements were analyzed in relation to a set of theoretical relationships derived by Tatarski (1961) for electromagnetic wave propagation in turbulent flow. Tatarski's derivation of the scintillation frequency spectrum (at a point in a plane perpendicular to the optical path) in relation to the three-dimensional spectral density of index of refraction inhomogeneities is summarized and interpreted in relation to its validity for various conditions of turbulence. Analysis of the spectral data showed that their characteristics were similar to Tatarski's theoretical spectrum if the divergence of the laser beam, the size of the receiver aperture, the intensity of scintillation and turbulence spectra were considered. Specific results of the analysis revealed: (1) Agreement between a theoretical variance for scintillation calculated from meteorological data and the variance measured from the spectral densities; (2) A linear increase of the frequency of maximum power with wind speed component normal to the optical path in agreement with Tatarski's model; (3) A decrease of scintillation intensity with path height and an accompanying increase in its frequency of maximum power, both closely related to height variations of stability and wind speed; (4) A relative decrease in intensity of scintillation at low frequencies when the potential temperature increases with height. The Appendix consists of a description and discussion of the method of spectral analysis and its application to processing the scintillation and turbulence data.

DD FORM 1 NOV 68 1473 REPLACES DD FORM 1473, 1 JAN 64, WHICH IS OBSOLETE FOR ARMY USE.

Unclassified

Security Classification

14. KEY WORDS	LINK A		LINK B		LINK C	
	ROLE	WT	ROLE	WT	ROLE	WT
Laser scintillation Optical scintillation Electromagnetic wave propagation Spectral analysis						